

Z 2899.10

Prepared for:

DG Rijkswaterstaat


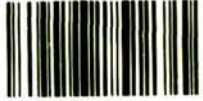
Rijkinstituut voor Kust en Zee/RIKZ

Numerical simulation of wave-current driven sand transport

Theoretical background of the beta-release of the POINT SAND Model
Revised edition

Report

October 2000

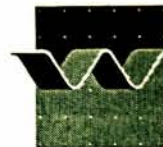
	WV-Check WV-2000 (WV) Edit WV-2000 (WV) Edit
	57848
	Z 2899.10
EXPL	 R0008201

Numerical simulation of wave-current driven sand transport

Theoretical background of the beta-release of the POINT SAND Model
Revised edition

R.E. Uittenbogaard, J. Bosboom, Th. van Kessel





CLIENT: DG Rijkswaterstaat; Rijksinstituut voor Kust en Zee / RIKZ

TITLE: Numerical simulation of wave-current driven sand transport

ABSTRACT:

This is the revised version of our previous report (Nov. 1999) that describes the theoretical background of the beta-release of the POINT-SAND model. The POINT-SAND model is a computer code solving the relevant equations for momentum, turbulence and sediment as a function of the vertical co-ordinate as well as in time for wave-current-turbulence-sediment interactions in free-surface currents as well as in wave tunnels. The main purpose of the POINT-SAND model is being a research tool for sharing and focussing ongoing research in The Netherlands on sand transport. Presently, we implemented just standard formulations for settling velocity, hindered settling and bed erosion under sheet-flow conditions. The novel aspect of the code is the explicit simulation of intra-wave sand transport subjected to wave-current-turbulence interactions for stationary non-breaking waves and horizontal bed.

This revised version introduces and demonstrates a built-in test facility for checking the accuracy of the implemented sand-transport processes, numerical solution procedures and physical as well as numerical parameter setting. This test facility is based on the analytic solution for the depth-integrated flux of suspended sand in stationary turbulent flows.

In addition, this version presents extensive series of wave-current simulations with comparison to observations in the Scheldt flume of monochromatic, bichromatic and random waves, mostly propagating on a turbulent shear flow. It is demonstrated that the wave-current option of the POINT-SAND model is capable of simulation these laboratory flows.

Finally, this report is extended with our papers for the ICCE symposium (Sydney, 2000). One of these papers explores the feasibility of the POINT-SAND model for investigating on-shore/off-shore sand transport in wave-driven currents over plane beds.

REFERENCES:

VER.	ORIGINATOR	DATE	REMARKS	REVIEW	APPROVED BY
1	R.E. Uittenbogaard	September 2000		A. Roelfzema	
2	R.E. Uittenbogaard	October 2000		A. Roelfzema	T. Schilperoord

PROJECT IDENTIFICATION:		Z2899					
KEYWORDS:		Wave-current interaction ; intra-wave sand transport; wave tunnel; sheet flow					
CONTENTS:	TEXT PAGES	60	TABLES	FIGURES	19	APPENDICES	7
STATUS:		<input type="checkbox"/> PRELIMINARY		<input type="checkbox"/> DRAFT		<input checked="" type="checkbox"/> FINAL	

Contents

1	Introduction.....	1-1
1.1	Aim and scope of present study.....	1-1
1.2	Process description.....	1-2
1.3	Outline of report and floppy disk.....	1-4
1.4	Acknowledgements.....	1-5
2	Overview of concepts and solution procedure.....	2-1
2.1	Introduction.....	2-1
2.2	Outline of concepts and solution procedure.....	2-2
2.3	Simplifications.....	2-6
3	Solving the orbital velocity vector.....	3-1
3.1	One-dimensional Poisson solver for pressure by surface waves on a non-uniform flow.....	3-1
3.2	Solving the vertical orbital velocity per spectral component.....	3-4
3.3	Solving the horizontal orbital velocity of a single spectral component....	3-7
4	Turbulence closure.....	4-1
4.1	High-pass filter function for wave-turbulence interaction.....	4-1
4.2	Turbulence model.....	4-5
5	The mean velocity profile and mean flow rate.....	5-1
6	Sediment distribution model.....	6-1
6.1	Advection-diffusion equation.....	6-1
6.2	Boundary conditions.....	6-3
6.3	Mass conservation and inconsistency with dynamical equations for orbital motions.....	6-4

6.4	Numerical implementation.....	6-6
7	Tests case.....	7-1
7.1	Introduction.....	7-1
7.2	Built-in test case.....	7-1
7.3	Wave-current interaction; the Scheldt flume	7-3
7.4	Sand transport; the wave tunnel.....	7-6
	7.4.1 Test cases	7-6
	7.4.2 Input/output.....	7-6
	7.4.3 Results.....	7-7
7.5	Sand transport by waves and wave-driven current	7-7
8	Conclusions, discussion and recommendations.....	8-1
8.1	Conclusions.....	8-1
8.2	Discussion.....	8-3
8.3	Recommendations.....	8-4
	References.....	Lit.-1

Appendices

- A Overview of solution procedure**
- B Direction of orbital velocity and wave number vectors**
- C Partial slip condition**
- D Description of program in- and output**
- E Built-in test case**
- F ICCE Paper on simulating wave-current interaction**
- G ICCE Paper on intra-wave sediment transport**

Summary

Despite joint fundamental research in the EU and in The Netherlands (NCK) towards sand transport in coastal waters, most of the basic numerical research tools remain dispersed. The main reason is that research groups or individual researchers design their own numerical tools for their particular sand-transport experiment. The so-called one-dimensional vertical (1DV) models for intra-wave simulation of flow, turbulence and sand transport are the most popular tools in this field of research. The various 1DV models are validated only for particular applications and most of them rely on a single turbulence model. Further, all known intra-wave 1DV numerical models are limited to so-called rigid-lid wave tunnel experiments with horizontally oscillatory flows. On the other hand, there are doubts whether these tunnel experiments represent correctly sand transport under surface waves because of a vertical orbital velocity component and of wave-induced streaming in boundary layers. In addition, most 1DV models are poorly documented which hampers the transfer to, as well as independent repetitions of the simulations by others.

This state-of-affair frustrates the progress in fundamental research on sand transport because the doubts and differences already begin with the hydrodynamic simulation of a stationary channel flow even more so for oscillatory wave-tunnel experiments and then the question about their applicability to real surface wave conditions. Finally, all this accumulates in hydrodynamic deviations that are amplified strongly by the non-linear and mostly empirical closures for sand transport.

The set-up of the POINT-SAND model, described in detail in this report, is our attempt to consolidate the present state-of-art, to improve the research conditions by stimulating mutual but independent comparisons as well as the exchange of new findings as implemented in this code.

These objectives demand an intra-wave 1DV model that allows for simulating the oscillatory flow in rigid-lid wave tunnel, in mobile free-surface wave channel as well as for waves and (tidal) flows arbitrary angle in the field while using the same formulations for sand transport. These aspects are incorporated in our POINT-SAND model. Here POINT refers to conditions along the water depth at a single horizontal point and SAND to the on-line coupled simulation of vertical and horizontal sand fluxes by multiple sand fractions.

The POINT-SAND model is designed for simulating sand transport in the following typical flow configurations:

1. constant-flow channel (free surface);
2. confined wave tunnel (rigid lid);
3. field conditions without surface waves (wind-driven and tidal currents, varying water depth, varying flow direction);
4. combined wave-current channel (free surface, waves parallel to flow); or
5. field conditions with surface waves (wave propagation irrespective of flow direction).

By its one-dimensional nature, the POINT-SAND model is dedicated to horizontally homogeneous flows over horizontal flat beds for periodic and non-breaking surface waves. We recommend the implementation of existing models for the net effects on mass and momentum transfer by breaking waves and by secondary or Langmuir circulation. For the latter we recommend Radder's model, see (Dingemans, 1999). Further, we recommend the development of a model for turbulence generation over rippled beds for which so-called Direct Numerical Simulations of the 3D turbulent flow at all relevant scales are available.

The modular set-up of the POINT-SAND model by series of subroutines, written in FORTRAN77, is dedicated to future users who desire to implement and validate their own theories and closures. The model has extensive options for input, output and spectral analysis and in this report various examples of input lists are given. A built-in test case allows the user to verify that his adjustments are still in accordance with the few known analytic solutions of sand transport in stationary turbulent channel flow. Currently, the POINT SAND model is equipped with three popular turbulence models ($k-\epsilon$, $k-L$ and Davies' version of the $k-L$ model) all based on eddy viscosity concepts. The set-up of subroutines allows for an easy implementation by the user of other turbulence closures within the eddy viscosity concept.

The present report is extensive because it presents details of the solution procedures with novel aspects regarding turbulence closures and particularly for simulating the wave-current-turbulence interaction problems. For those readers who wish to avoid the mathematics, we have written the overview report (Uittenbogaard, 2000). The latter report includes a motivation of the model set-up, flow diagrams of the solution procedures, tables of the modelled or explicitly simulated processes and a sensitivity analysis for the depth-integrated sand flux to variations in input variables.

Of course, many different and thorough validations are required before the POINT-SAND model will be accepted as a general tool. This report therefore presents many comparisons against wave-tunnel and wave-channel experiments. Most hydrodynamic comparisons are in good to excellent agreement with laboratory observations on currents, oscillatory flows and surface waves. Further, the tidal or stationary current part of the hydrodynamic module is the result of much experience at WL|Delft hydraulics in simulating tidal flows, seasonal thermocline evolution as well as silt transport.

Instead, the comparison of the sand-transport simulations with the POINT-SAND model against wave-tunnel observations is unsatisfactory and occasionally poor. We believe the latter conclusions exhibit the known deficiencies in modelling intra-wave sand transport as well as deficiencies in modelling turbulence in oscillatory flows and in high-concentration sediment flows. These are some of the present research targets in this field for which we hope the POINT-SAND model shall be of assistance.

I Introduction

I.1 Aim and scope of present study

1DV unsteady models resolve the time- and depth-dependency of the velocity and concentration fields. The development and refinement of 1DV unsteady models provides us with further information about the complex processes of sediment suspension enabling a further improvement of engineering transport models. As such the 1DV unsteady models not only increase our knowledge about the sediment transport processes but provide us with a way of improving transport descriptions in morphological models by: 1) parameterization of the unsteady 1DV models, 2) by making an initial effort of tabulating the results of the intra-wave model for a specific situation, after which the morphodynamic model is run at relatively low costs, or 3) by finding analytical approximations to the governing equations (Bosboom, 1999).

In Bosboom and Cloin (1998) the development of an intra-wave sediment transport model is proposed. In the latter report, on the one hand, the presently available 1DV models are described focusing on the underlying physics and their merits and shortcomings as found in previously performed validation studies. On the other hand, necessary future developments are identified and a sediment transport model is proposed including many of these features and with a structure which facilitates cooperation on validation and future developments in an NCK framework. As such it could be considered as a "national sand transport model" acting as a 'knowledge carrier' ('kennisdrager'). Besides, an important aspect of the proposed model as compared to presently available models is the extension to field situations by including e.g. irregular waves, wave-induced streaming (and thus the treatment of vertical velocities) and the treatment of the complete water column.

Whereas the latter study can be seen as a first step by identifying the preferred developments, the present study is a follow-up aiming at the actual development of a first version of the intra-wave model (POINT-SAND model). The beta-release, on the floppy disk attached to this report, is thought to be a first version serving as a base for discussion, future extension and improvement. It does not pretend to be complete in the sense that all the processes to be modelled as identified in Bosboom and Cloin (1998) are taken into account. Also some numerical aspects can be improved in the future, especially regarding the sediment transport module. Although this module functions well when solving horizontal velocities only (as suffices for comparison with wave tunnel experiments), it does not yet work well when solving vertical velocities (as is needed when considering orbital motions generated by surface waves). In addition, calculated sediment concentrations still depend on the chosen grid schematization.

A limited number of wave-current interaction and sediment transport experiments were selected to compare with the model. The aim of this comparison was a first model diagnosis rather than an extensive model validation.

The beta-release however, in combination with the present report serving as a theoretical reference document is thought to provide a concrete basis for discussion in NCK-framework on a multitude of aspects ranging from process description, numerical treatment and model structure to in- and output requirements. It therewith aims at materialising the Cupertino in NCK-framework with the ultimate aim to put an important step forward in the process-based descriptions of sediment transport.

1.2 Process description

The directional point model (DPM/POINT-MUD; Winterwerp and Uittenbogaard, 1997) is developed by joint funding of WL|Delft Hydraulics and by Rijkswaterstaat RIKZ. This model is used as a basis for the development of the intra-wave sand transport model that we call POINT-SAND model. The most far-reaching changes to the model structure result from taking into account the non-linear convective terms in momentum equations for the orbital velocity vector and the consistent coupling with a sand transport module.

The overview report (Uittenbogaard, 2000) describes with more words the physical aspects of the POINT-SAND model. That report also presents an overview of the processes that are solved explicitly, modelled or neglected. The following tables are taken from this overview report.

Input/control by user:

Process or function	options
Numerical control parameters	five choices for layer distribution, time step, time for output, time series and of harmonic analysis
Advection scheme for sediment	1 st order upwind or 2 nd order central scheme
Turbulence models	laminar; k-L, k-L (Davies' version), k- ϵ
Bed friction	partial slip: Chezy, Manning, roughness length or no-slip with given viscosity.
Mean flow equations	IDV or orthogonal (u,v) components
Earth rotation	Coriolis parameter
Water depth	constant, time series or harmonics
Tidal current vector (<i>outer loop</i>)	depth-averaged or at given fixed reference level: constant, time series or harmonics
Atmospheric forcing	constant or time series: wind vector, air pressure, cloudiness, air humidity
True orbital motions (<i>inner loop</i>)	<i>inner loop</i> time step, relaxation time for WCI force and reference to a file for amplitude, period, phase and direction of the spectral wave components
Time series output	for given z-level over given time interval
Sediment properties	multiple fractions, d_{50} , ρ_s , σ_T , pick-up or bed concentration, initial sand profile
Water density	initial profile temperature and salinity
On-line harmonic analysis	for given list of frequencies
Test cases	if the extension of the input file is <i>log</i> , see also on-line an analysis below

Processes explicitly simulated:

process or function	properties
Mean flow	(z,t) over entire water depth only, depending on bed friction, internal friction, wind forcing, Coriolis, WCI force.
Surface waves	vertical and horizontal orbital velocity (z,t) over entire water depth only depending on bed friction, internal friction, horizontal current, solving pressure, arbitrary direction and phases, WCI force, boundary layer streaming
Sediment transport	(z,t) over entire water depth only, depending on settling velocity, hindered settling, orbital motions, diffusion, pick up or bed concentration
WCI force	(z,t) dependent on surface wave solution
Boundary layer streaming	(z,t) dependent on surface wave solution
Stokes drift for sand mass	(z,t) according to sediment transport and on surface wave solution
Diffusion without advection	(z,t) by mixing only and for heat content through computed thermal flux at the free surface

Built-in formulations:

process or function	properties
gravity	fixed
density of water	state equation for sea water
thermal flux	four options up to most explicit formulation for air-water heat exchange processes
Stokes drift water mass	correction for depth-integral Stokes mass drift
Turbulence	laminar or three eddy viscosity type models, see input; fixed turbulence model coefficients
Buoyancy	through vertical density gradient of sand, salt, temperature
bed friction	linear for laminar flow, quadratic for turbulent flow with fixed zero level for log. profile.
Wind-drag coefficient	Smith&Banks formulation
High-pass filter	fixed formulation, for surface waves only
Shields parameter	piecewise approx. depending on grain size and u_* (Van Rijn, 1993)
Settling velocity	piecewise approx. depending on grain size, viscosity, density of sand and water (Van Rijn, 1993)
Hindered settling	Richardson-Zaki formulation, fixed coefficients
Bed concentration	Zyserman&Fredsoe at $z=2d_{50}$ above fluid-bed interface

On-line analysis:

Harmonic analysis	(u;v;w;c;uc;TKE;v _T ;WCI) for given frequencies over given time interval (see input)
Stress power	estimation of energy losses by surface waves
Testcases	for *.log extension: no-slip, partial slip, laminar, turbulent, log. profile, Rouse profile, parabolic eddy viscosity, sand flux numerical and analytic integration

Assumptions and approximations:

Reynolds stresses/fluxes	closure based on eddy viscosity/diffusivity
laminar-turbulence transition	closures for high-Reynolds number turbulent flows only
turbulence in oscillatory flow	closure using high-pass filter function only applicable when each spectral wave component is simulated
mobile free surface	boundary conditions imposed on rigid lid
orbital motions	dedicated to shear-dominated and turbulent flows
Stokes drift water mass	depth-averaged flow corrected by analytic formulation for Stokes drift
wave form	as sum of spatially and temporarily periodic waves; no wave breaking
test cases	for sediment transport in steady flow only
bed form	plane horizontal bed, sheet-flow conditions
erosion/sedimentation	Zyserman-Fredsøe formulation meant for single fraction
input from experiments	prescription by time series of sediment concentration at some given fixed level is not yet available
input from experiments	the piece-wise approximations to the Shields parameter as well as to the settling velocity is discontinuous
laminar-turbulence transition	closures for high-Reynolds number turbulent flows only
sand-water density	buoyancy term in turbulence closures but not in momentum equations

1.3 Outline of report and floppy disk

In Chapter 2 an overview is given of some concepts and assumptions underlying the model. Also the solution procedure, using an inner and *outer* loop, is outlined here. Chapter 3 describes the solution to the orbital velocity vector in the *inner* loop. Chapter 4 deals with the turbulence closure model. In Chapter 5, the mean flow equations, solved in the *outer* loop are given. The equations for the sediment are given in Chapter 6. Chapter 7 gives a short description of some exercises focussing on diagnosis of the model. Section 7.3 describes a comparison with two wave tunnel experiments. One of the tests described here can also be found on the accompanying floppy disk which also contains the model executable. The input and output of the model are discussed here. Appendix A presents schematically the various loops as well as the most important subroutines; this appendix serves as a rough guideline of the code. The essential assumption underlying the POINT-SAND model is related to the treatment of horizontal variations. Appendix B investigates an additional approximation made in that respect, viz. that the horizontal part of the velocity-amplitude vector $\hat{u}(z)$ is parallel with the corresponding wave number vector \underline{k} . In Appendix C we present details of the implementation of the partial slip condition for the turbulent flow along a bed in the fully-rough regime. Appendix D contains a listing of the input files of one of the wave-tunnel tests of which the results are reported on in Section 7.3.

Compared to the previous version of this report, Appendices E to G are new. Appendix E presents the mathematical background of built-in test cases for sand transport in steady turbulent channel flows. These test cases are designed so that the future user and developer of the POINT-SAND model can verify his work and code adaptations. In addition, Appendix E demonstrates the strong sensitivity of the depth-integrated horizontal sand flux for flow conditions. The latter sensitivity thus emphasizes the importance of carefully testing the hydrodynamic aspects of the POINT-SAND model. Appendix F is our ICCE paper presented in the ICCE-conference in Sydney. The paper describes several wave-current interaction and some more details that reported here. Similarly, Appendix F presents our paper on intra-wave sediment transport and it contains additional hydrodynamic and sand transport tests. Moreover the latter appendix also introduces one of the purposes of the POINT-SAND model namely connecting wave-tunnel experience to on-shore or off-shore sand transport in the field.

The admittance of these papers to the ICCE conference can be interpreted as an international reference to the quality of the work presented in this report.

1.4 Acknowledgements

This work is undertaken in the SEDMOC project, in the framework of the EU-sponsored Marine Science and Technology Programme (MAST-III), under contract no. MAS3-CT97-0115. It is cosponsored by the Dutch Ministry of Transport and Public Works (Rijkswaterstaat), WL|Delft Hydraulics in the framework of the Netherlands Centre for Coastal Research (NCK) and Delft Cluster Sediment Transport under contract no. 03.01.01.

We gratefully acknowledge the stimulating discussions with Dr. J. van de Graaff and Mr. G. Klopman and the corrections by the RIKZ referee. We hope to have responded correctly to their comments as well as criticism on the previous version of this report.

2 Overview of concepts and solution procedure

2.1 Introduction

This report describes the POINT-SAND model being the extended version of the Directional Point Model (DPM). The POINT-SAND model is dedicated to simulating, in time, the vertical distribution of suspended sand in an oscillatory horizontal flow in a wave tunnel but also due to the horizontal and vertical orbital velocity, possibly superimposed on a turbulent current, in free-surface wave channel or in the field with different wave and current directions. Irrespective of the application in a wave tunnel or a free-surface wave channel, the same intra-wave sand transport formulations are used. These sand transport process formulations have been reported and demonstrated by others. With respect to the sand-transport process formulations, the POINT SAND model is not superior to published 1DV models but our model is just more flexible.

The DPM and its predecessor, the 1DV model (one velocity component only), are presented in (Kester et al., 1997) for simulating thermally-stratified tidal flows. In (Uittenbogaard et al., 1996) and (Winterwerp and Uittenbogaard, 1997) mud transport is simulated for steady as well as tidal flows and with the effect of surface waves parameterised by an increased bed roughness only. These existing 1DV and DPM codes were in principle already suitable for simulating sand transport in wave-tunnel experiments because these experiments do not induce a mean or orbital vertical velocity.

The extensions in the POINT SAND model concerns mainly the inclusion of orbital motions for simulating more aspects of wave-current interaction (WCI), streaming, wave-turbulence interaction, all this in the context of simulating suspended sand transport under sheet-flow conditions. The flow along the entire water depth is simulated for a correct estimation of WCI. The selection of a non-equidistant vertical grid, however, allows for resolving details of the wave boundary layer.

The loading of the flow with suspended sediment is considered to yield damping of turbulence equivalent to salt-stratified or thermally-stratified flows. This stratified-flow analogy, however, requires modification to large particle densities. For the time being, the stratified-flow analogy is adopted in the implemented k -L and k - ϵ turbulence models through the usual buoyancy flux that represents the conversion of Turbulent Kinetic Energy (TKE) into potential energy.

The POINT SAND model can be regarded as a spectral code. Per spectral component, it solves the orbital motions as a function of depth and mean flow profile. The direction of wave propagation as well as (tidal) flow is arbitrary and we assume spatially periodic wave motions. The bed is assumed to be horizontal and the waves are periodic and non-breaking. The latter restrictions exclude sloping beds as well as strong decay or growth of wave

properties. In principle, each harmonic component of a multi-directional wave spectrum is simulated although simulating many harmonics reduces the computation speed proportionally.

The orbital motions by the surface waves are simulated explicitly while keeping in mind the principle objective of the POINT SAND model. The objective of this model is sand transport in turbulent shear flows with waves and this sand transport is usually confined to just the bed-boundary layer. Therefore, the mobility of the free surface is neglected i.e. in the POINT SAND model the free surface is replaced by a rigid lid on which the surface boundary conditions are imposed. We acknowledge that the latter condition is a crude approximation if the interest is on simulating near-surface motions and near-surface wave-induced drift phenomena. On the other hand, the good comparison between experiments and simulations appear not to suffer severely from this rigid lid approach. There is possibly one exception namely the case of waves propagating on a laminar flow because the rigid-lid approach does not allow for a precise description of the conditions for viscous stress and surface tension at an inclined and rotating free surface. Nevertheless, even that exceptional test case is simulated quite well, for details see Appendix G.

There are no limitations on angular frequency, water depth, depth-averaged velocity or velocity shear rates, provided the latter do not induce wave blocking or a critical layer i.e. conditions where the phase speed equals the mean velocity.

2.2 Outline of concepts and solution procedure

By way of introduction, the solution strategy is presented here but the subsequent chapters describe the mathematical details.

The original DPM solves partial differential equations for flow, constituents (sediment, salt, heat etc.) and turbulence as a function of depth co-ordinate z and time t for a steady or slowly-varying (tidal) flow for a given depth-averaged horizontal velocity and using a hydrostatic pressure. In the original DPM, the momentum equation for one of the two horizontal velocity components reads

$$\frac{\partial U}{\partial t} + \frac{\partial P}{\partial x} = \frac{\partial}{\partial z} \left\{ (\nu + \nu_T) \frac{\partial U}{\partial z} \right\} + T_x(z, t) \quad (2.1)$$

with turbulence-averaged horizontal velocity $U(z, t)$, turbulence-averaged pressure P , kinematic viscosity ν , eddy viscosity $\nu_T(z, t)$, horizontal co-ordinate x and vertical co-ordinate z . The POINT SAND model includes the Coriolis force but this contribution is not of importance here but included in the (extended) code. In this report, pressure is always divided by constant fluid density i.e. Boussinesq's approximation is applied. In (2.1), P is z -independent and $\partial P / \partial x$ is adjusted such that the depth-average of $U(z, t)$ satisfies a user-defined temporal function or constant (time series or harmonic components on input). This is the original and satisfactory approach with the DPM, see (Uittenbogaard et al., 1996) and (Van Kester et al., 1997) for tests and applications.

The extension of the DPM as POINT-SAND model for WCI involves the solution of the depth-dependent momentum equation for the orbital velocity vector of each spectral component as well as the dynamic and kinematic influence (Stokes drift) on mean flow and on turbulence. For the dynamic influence, the depth-dependent wave-current-interaction force T_x in (2.1) is essential. This force is a wave-averaged property and it depends on the vertical co-ordinate. The WCI force varies with the time scale of the mean current such as under tidal flow conditions. In the following, these influences are described briefly.

In the POINT-SAND model, the WCI problem is formulated in Eulerian co-ordinates and for infinitesimal waves propagating on a non-uniform flow. In vector notation, the following equations for orbital momentum are added to the POINT-SAND model:

$$\frac{\partial \tilde{u}}{\partial t} + (\underline{U} + \tilde{u}) \cdot \nabla (\underline{U} + \tilde{u}) + \nabla \tilde{p} = \nabla \cdot \tilde{\underline{\sigma}} - \underline{T} \quad ; \quad \underline{U} \cdot \nabla \underline{U} = \underline{0} \quad , \quad (2.2)$$

with \tilde{p} the hydrodynamic pressure driving the orbital velocity vector \tilde{u} ; the mean flow is horizontal and has just a vertical profile. Not all horizontal advection terms are implemented, but this will be presented later. Per spectral component, the hydrodynamic pressure \tilde{p} is solved for waves over a shear flow but linearized in terms of orbital motions.

In (2.2), \underline{T} is the WCI force that in general is a three-dimensional vector and a wave-averaged property. In the following we explain why we neglect the vertical component of \underline{T} and why we compute the horizontal part of \underline{T} numerically rather than using some theoretical model. We start with the neglect of the vertical component of \underline{T} in the POINT-SAND model.

One of the contributions to \underline{T} is the so-called Craik-Leibovich (CL) vortex force. The CL vortex force is the outer product of the Stokes drift (horizontal drift velocity) and the vorticity vector of the mean flow, for details see e.g. (Dingemans et al., 1996) and its references. Consequently, for a horizontally uniform but possible vertically sheared flow the CL vortex force has just a vertical component. When the mean flow is perturbed then the CL vortex force invokes an instability yielding counter-rotating vortex pairs with horizontal axes parallel to some mean of wave propagation and current direction. In large water bodies, such as lakes and seas, these vertical circulations are called Langmuir circulation but also in flumes the CL vortex force creates secondary circulation perpendicular to the current. This secondary circulation enhances the exchange of horizontal momentum between the flume centre plane and the vertical walls. This momentum exchange then alters the flow in the flume centre plane, for details see (Dingemans et al., 1996).

These wave-driven circulations, however, can be simulated explicitly only when the flow equations are solved in a two-dimensional cross section perpendicular to the flow, such as in (Dingemans et al., 1996), or solved fully in three dimensions. Therefore, in the POINT-SAND model having just one spatial dimension, we can only include the consequences of the CL vortex force by the addition of a suitable model, such as Radder's model presented in (Dingemans, 1999). The implementation of Radder's model in the POINT-SAND model is recommended. This ends our motivation about not including the vertical component of \underline{T} in the POINT-SAND model. Below we motivate the numerical procedure for the horizontal components of \underline{T} .

The orbital motions of waves near the bed and near the free surface invoke shear stresses acting on horizontal planes. These shear stresses are mainly due to the laminar or turbulent bed friction or due to the stress free condition at the free surface while it rotates with the wave motion. The laminar or turbulent stresses create a deviation in the $\pm 90^\circ$ phase lag between vertical and horizontal velocity components. The vertical derivative of the wave-induced shear stresses contributes to the horizontal part of \underline{T} . Various approximate models for these stresses have been developed. Note that these contributions are not represented by the CL vortex force. On the one hand we could implement a theoretical approximation to the laminar or viscous stress contribution for the horizontal part of \underline{T} . Not only a difference between this approximation and the exact force but also numerical errors can induce an accelerating drift velocity through (2.2). By definition, the occurrence of this theoretical or numerical drift in (2.2) is excluded because (2.2) refers to oscillatory motions with zero averages.

Therefore, the horizontal components of \underline{T} are simulated with a numerical procedure such that the time average of the horizontal orbital velocity in (2.2) is negligibly small or zero. The latter condition agrees with the precise definition of orbital motions. The simulated \underline{T} counter-balances the time average of mainly the non-linear part of the convective terms in (2.2) that represents the vertical gradient of the simulated wave-induced shear stress.

This computed \underline{T} yields no artificial drift and then it must represent the transfer of momentum between the mean flow and the orbital motions. Therefore \underline{T} re-appears in the mean flow equation (2.1) with the opposite sign compared to (2.2).

The horizontal part of \underline{T} , obtained by some numerical procedure, varies over the water column and, when applied to (2.1), \underline{T} deforms the mean velocity profile. The depth-averaged part of \underline{T} affects the horizontal hydrostatic pressure gradient in (2.1) and the orbital velocity superimposed on a current increases the wave-averaged bed-shear stresses.

This ends our motivation for using some numerical procedure for the horizontal part of \underline{T} . Notice that the particular choice of the procedure is irrelevant as long as it meets its objectives namely convergence in achieving a negligibly small or zero average of the horizontal orbital velocity. Once these objectives are met then the horizontal part of \underline{T} equals the WCI force, except for some numerical errors in (2.2) that \underline{T} also counter balances.

In (2.2), $\underline{\tilde{\sigma}}$ is the oscillatory part of the stress tensor due to molecular as well as turbulent motions. The latter are represented by $\underline{\tilde{R}}$, the oscillatory part of the Reynolds stress tensor \underline{R} . Chapter 4 explains the closure for $\underline{\tilde{R}}$ but, for clarity, some introductory remarks are made but we refer to (Uittenbogaard, 2000) for an extensive description.

Below we describe why eddies of different sizes and turnover times respond differently to the strain rates induced by the orbital motions. Imagining an eddy as some isolated cylinder of fluid rotating around a curled axis is a simplification on its own but still is a feasible concept.

When each fluid parcel of a large and slowly rotating eddy has covered just a small part of its orbit then short and fast orbital motions already have reversed their influence on the paths of the fluid parcels. After one spatial and temporal wave cycle, the net effect of the wave on the large and slow eddy is negligible and, conversely, the eddy did not transfer the momentum of the orbital motions. Therefore the larger and slower eddies are nearly inactive in damping surface waves.

Instead, fluid parcels in sufficiently short and rapidly rotating eddies are “swept out of orbit” by the comparatively slow and large deformations imposed by the orbital motions. In other words, small and fast eddies are deformed significantly by the orbital motions. This deformation involves a spatial transfer of momentum that is nearly irreversible because fluid parcels enter orbits around other eddies and so on. Consequently, these smaller eddies create a net spatial transfer of the wave-related momentum.

This is our argumentation why sufficiently small and rapid turbulent motions are active in damping surface waves. Such turbulent motions dominate in the boundary layers where their size is limited by the proximity of the bed or the free surface. In these boundary layers, therefore, most turbulent eddies contribute to the deviation from the $\pm 90^\circ$ phase lag between vertical and horizontal orbital velocity components and this deviation creates the wave-induced shear stresses. Subsequently, the vertical derivative of the wave-induced shear stresses contributes to the WCI force and deform the mean velocity profile.

In most applications, the transfer of momentum or mass by turbulence is modelled by the eddy viscosity/diffusivity concept. In this concept, the eddy viscosity/diffusivity is proportional to the product of the variance of the vertical turbulent velocity component and its correlation time scale. As we argued above, the appropriate eddy viscosity for the transfer of wave-related momentum should be based on the variance of vertical velocity and correlation time of eddies smaller and faster than the orbital motions. The previous argumentation can be cast in mathematical formulations. It then yields what we call a high-pass filter function f_{hp} depending on the ratio between wave period and turbulence correlation time, for details see Chapter 4. The terminology “high-pass filter” refers to eliminating the contributions from slow and large turbulent motions to the eddy viscosity.

Rather than solving the total momentum equations, the decomposed set (2.1) and (2.2) allows for splitting the turbulence response due to orbital motions or due to mean flow only. The high-pass filter function reduces the eddy viscosity, related to all sizes of turbulent motions, as described by e.g. k-L or k- ϵ models.

Another important reason for splitting mean flow and orbital motions is that orbital motions can induce significant horizontal gradients. Assuming spatially and temporarily periodic waves, the horizontal gradients of the orbital motions are expressed at the relevant time derivative divided by the phase speed of the spectral wave component.

The mixing of sediment by turbulence responds to all turbulent motions. Consequently, the high-pass filter function is not applied to the eddy diffusivity being the turbulence mixing coefficient for dissolved matter and sufficiently small sediment particles.

The orbital momentum equation (2.2) is solved by using the still water level as upper boundary (rigid lid) rather than the mobile free surface. This rigid-lid approximation simplifies the computation at the expense of a crude approximation of the free surface boundary conditions now imposed on the still water level. The consequence of this rigid-lid

approximation is that the wave-induced water-mass flux, equal to the depth-integrated Stokes drift, is not simulated explicitly by the POINT SAND model. Instead, the depth-integrated Stokes drift is estimated by the theoretical model derived in Appendix B of (Winterwerp & Uittenbogaard, 1997). This theoretical model is a function of the user-defined wave amplitude, the simulation orbital velocity as well as the simulated mean-flow shear rate. Subsequently, the depth-integrated Stokes drift is subtracted from the user-defined flow rate. The net flow rate is obtained by adjusting the hydrostatic pressure gradient $\partial P/\partial x$ in (2.1) during the simulation.

In the POINT SAND model two time loops are made and each time loop has its own time step. In the so-called *inner loop* for each spectral component (input) the orbital motions in (2.2) and contributions of orbital motions to turbulence are solved. Thus the *inner loop* represents the intra-wave part (2.2) of the POINT SAND model; the inner-loop time step should be a small fraction of the wave period. All spectral components are solved with the same inner-loop time step, (2.2) is solved on the same grid as the mean flow equation (2.1) and turbulence and sediment equations.

In the *inner loop* and per *inner loop* time step, the orbital motions are solved by starting with the slowest motions while including the non-linear coupling by advection of all spectral components. Per time step of the *inner loop*, all orbital shear rates are collected and then high-pass filtered. These filtered shear rates form the turbulence production term in the k-L or k- ϵ turbulence model that is solved at each *inner-loop* time step. Notice that in the *inner loop*, (2.2) is solved per spectral component and this becomes computationally demanding for a wide spectrum.

In the *outer loop*, subsequently, the wave-averaged forces and Stokes drifts of all spectral components are collected and the bed friction is low-pass filtered. Then the mean flow momentum equation (2.1) extended to arbitrary flow direction is solved. In this *outer loop*, a single and usually larger time step is made, typically this time step equal the largest wave period. The outer loop time step is an integer multiple (NUMWAV) of the inner loop time step. The averaging of wave properties per spectral component covers its most recently completed wave cycle.

At a new step of the *inner loop*, the adapted mean-flow profile is used to estimate the wave numbers for given angular frequencies and for estimating the advection of waves by a non-uniform current. This alternating solution procedure for (2.1) and (2.2) is repeated until end. Appendix A presents schematically the various loops as well as the most important subroutines; this appendix serves as a rough guideline of the code. The overview report (Uittenbogaard, 2000) illustrates this solution procedure by several flow diagrams.

2.3 Simplifications

Compared with a 3D wave-current simulation, the essential simplification for using the POINT SAND model concerns horizontal variations. Steady harmonic oscillations at given angular frequency ω with flow-dependent wave number vector $\underline{k}=(k, \ell)$ with component k in x-direction and ℓ in y-direction are assumed i.e.

$$\tilde{\psi} = \hat{\psi} \operatorname{Re} \left\{ \exp(i \underline{k} \cdot \underline{x} - i \omega t) \right\} ; \quad i = \sqrt{-1} \quad , \quad (2.3)$$

with $\tilde{\psi}$ any wave-related variable with zero mean and with constant and real amplitude. The amplitude $\hat{\psi}(z)$ of any oscillatory variable may depend on the depth co-ordinate z . Accordingly, the following transform (2.4) is applied to all wave-related fluctuations:

$$\frac{\partial..}{\partial x} = -\frac{k(\omega)}{\omega} \frac{\partial..}{\partial t} ; \quad \frac{\partial..}{\partial y} = -\frac{\ell(\omega)}{\omega} \frac{\partial..}{\partial t} \quad . \quad (2.4)$$

The wave-related surface elevation, with zero mean, is prescribed by

$$\tilde{\zeta} = \hat{\zeta} \sin[\underline{k}(\omega) \cdot \underline{x} - \omega t + \phi(\omega)] \quad (2.5)$$

with user-defined amplitude $\hat{\zeta}$ for each angular frequency ω as well as user-defined direction of propagation and user-defined phase shift ϕ . In the POINT SAND model, the wave number \underline{k} is a horizontal vector and its magnitude follows from solving the dispersion relation; this is explained in Section 3.1.

In principle, solving (2.2) involves three equations but the two horizontal momentum equations are reduced to just one for the horizontal velocity in the direction of wave propagation. The latter simplification is founded on Appendix B that derives, to a good approximation, that indeed the horizontal part of the velocity-amplitude vector $\hat{\underline{u}}(z)$ is parallel with the corresponding wave number vector \underline{k} .

3 Solving the orbital velocity vector

3.1 One-dimensional Poisson solver for pressure by surface waves on a non-uniform flow

In the *inner loop* and per spectral component (*spectral loop*), first the orbital velocity vector is solved by (2.2) for each spectral component. For simplifying the notation, we shall not include the dependence of orbital variables on angular frequency ω explicitly unless ambiguity arises.

Per spectral component, pressure \tilde{p} drives the momentum equations (2.2) for orbital velocity; in general \tilde{p} is non-hydrostatic. Pressure \tilde{p} is formulated in a Poisson equation that is derived from

$$\frac{\partial \tilde{u}}{\partial t} + (\underline{U} + \tilde{u}) \cdot \nabla (\underline{U} + \tilde{u}) + \nabla \tilde{p} = \underline{0} \quad ; \quad \underline{U} = U(z) \hat{e}_x \quad ; \quad \nabla \cdot \tilde{u} = 0$$

for surface waves on a z -dependent mean flow and with the neglect of molecular, turbulence as well as neglecting all quadratic orbital-velocity terms (advection). These equations then yield the following linearized Poisson equation

$$\nabla^2 \tilde{p} = -2 \frac{\partial U}{\partial z} \cdot \nabla \tilde{w} \quad . \quad (3.1)$$

Note that (3.1) includes waves relative to a vertically non-uniform flow at arbitrary angle of propagation. Substitution of (2.4) as well as of the linearized momentum equation for vertical velocity in (3.1) yields the following equivalent to the well-known Rayleigh equation:

$$\frac{d^2 \hat{p}}{dz^2} + 2B \frac{d\hat{p}}{dz} - |k|^2 \hat{p} = 0 \quad ; \quad B = \frac{1}{\Omega} \cdot \frac{\partial U \cdot k}{\partial z} \quad ; \quad \Omega(z) = \omega - \underline{k} \cdot \underline{U}(z) \quad . \quad (3.2)$$

This ordinary differential equation for the pressure amplitude is discretized on the vertical grid of the POINT SAND model with pressure defined in cell centres and its vertical gradient at cell interfaces. The surface cell has number $m=1$ and the bed cell $m=kmax$, the cell height is Δz_m . Typically 100 cells are used which may also be non-equidistant. Variables defined on the lower cell interface obtain the subscript of the cell above it and the variable at the mean water surface has subscript $m=0$.

The Poisson equation (3.2), equivalent to (3.1), is solved with vertical gradient $d\hat{p}/dz$ as principle unknown, see (Peyret and Taylor, 1983, Section 4.1), and by using quadratic splines for expressing pressure into its vertical gradient through:

$$\hat{p}_m - \hat{p}_{m+1} = \alpha_m \left(\frac{d\hat{p}}{dz} \right)_{m-1} + \beta_m \left(\frac{d\hat{p}}{dz} \right)_m + \gamma_m \left(\frac{d\hat{p}}{dz} \right)_{m+1} \quad , \quad (3.3)$$

with weight factors:

$$\beta_m = \frac{3}{8}(\Delta z_m + \Delta z_{m+1}) \quad ; \quad \alpha_m \equiv \gamma_m = \frac{1}{6}\beta_m \quad . \quad (3.4)$$

The exact boundary condition for pressure at the bed reads

$$\left. \frac{\partial \tilde{p}}{\partial z} \right|_{bed} = \frac{\partial}{\partial z} \left\{ 2(u + u_T) \frac{\partial \tilde{w}}{\partial z} \right\} \Big|_{bed} \quad ,$$

but Kraichnan (1956) showed that the gradient of normal stresses due to molecular and turbulent motions is negligible and thus the previous boundary condition can be simplified into

$$\left(\frac{d\hat{p}}{dz} \right)_{bed} = 0 \quad . \quad (3.5)$$

Next we introduce the following essential simplification. All equations are solved on a fixed grid and the boundary conditions at the free surface are imposed at the still water level rather than at the mobile free surface. This rigid-lid approximation has conceptual as well as computational advantages but at the expense of projecting the surface-boundary conditions on the still water level. In this approach the pressure at still water level is prescribed as the hydrostatic pressure

$$\tilde{p} = g\zeta \quad . \quad (3.6)$$

Numerically this condition is imposed on the pressure that is defined in the centre of the first cell ($m=1$). Using the vertical pressure gradients at cell interfaces and assuming a pressure profile quadratic in z , the pressure amplitude in the centre of the top cell reads:

$$\hat{p}_1 = g\hat{\zeta} - \frac{1}{8}\Delta z_1 \left\{ 3 \left(\frac{d\hat{p}}{dz} \right)_0 + \left(\frac{d\hat{p}}{dz} \right)_1 \right\} \quad . \quad (3.7)$$

With (3.5) and (3.7), the Poisson equation (3.2) is solvable but for a yet unknown wave number magnitude $|k|$. The latter is determined by the so-called dispersion relation. This relation follows from replacing \tilde{w} , in its linearized vertical momentum equation without

viscous or turbulence stresses, by the linearized material derivative of ζ , yielding for sufficiently-small wave amplitude:

$$\left(\frac{\partial}{\partial t} + \underline{U}(z) \cdot \nabla \right) \tilde{\zeta} + \left(\frac{\partial \tilde{p}}{\partial z} \right)_{\bar{\zeta}} = 0 \quad (3.8)$$

The angular frequency $\Omega(z) = \omega - \underline{k} \cdot \underline{U}(z)$ in (3.2) is recorded by a co-moving observer at level z . Substitution of (2.3) in (3.8) and then differentiation with respect to the wave amplitude yields at the still water level:

$$\Omega^2(\bar{\zeta}) = \left(\frac{\partial^2 \hat{p}}{\partial z \partial \bar{\zeta}} \right)_{\bar{\zeta}} \quad (3.9)$$

Equations (3.2) and (3.9) are mutually coupled where the essential unknown is the wave number magnitude appearing in $\Omega(z) = \omega - \underline{k} \cdot \underline{U}(z)$ in (3.2) as well as in (3.9). Therefore, these two equations are solved iteratively. The iteration begins with an estimate for the wave number magnitude $|\underline{k}|$ derived from the dispersion relation of infinitesimal potential waves superimposed on a mean current. Next, Ω is obtained from a finite difference version of (3.9) by solving (3.2) twice: for zero and for unit wave amplitude. The difference in vertical pressure gradient at the still water level $z = \bar{\zeta}$ then yields Ω^2 from (3.9). By Picard iteration the new estimate for the wave number follows from

$$|\underline{k}|^{(n+1)} = \frac{\omega}{\text{sign}(\hat{\underline{k}} \cdot \underline{U}(\bar{\zeta})) + \Omega^{(n)} / |\underline{k}|^{(n)}} \quad \text{for fixed } \frac{\ell}{|\underline{k}|} \quad ; \quad |\underline{k}| = \sqrt{k^2 + \ell^2} \quad (3.10)$$

with iteration counter $n=1,2,3\dots$. The Froude number is assumed subcritical so that no wave blocking or critical layer is formed i.e. $\Omega(z)$ is non-zero everywhere and thus B remains regular. Velthuisen and Van Wijngaarden (1969) consider the case of critical-layer formation at the level where $\Omega(z)=0$ holds. Initially, five to seven iterations are required for 1% relative accuracy but for subsequent wave cycles just a single iteration appears sufficient. The dispersion relation is solved at the start of a new wave cycle, using a new estimate of the mean flow profile in (3.2).

Of course, the converged solution of (3.2) and dispersion relation (3.9) yields also the vertical profile of $d\hat{p}/dz$, normalised by the wave amplitude. From this pressure gradient follows the wave-related pressure amplitude by (3.3) and starting at the still water level condition (3.6). Subsequently, the horizontal gradient of the pressure amplitude follows from the time derivative of the pressure amplitude and using (2.4). At all subsequent time steps, the horizontal pressure gradient in a single wave cycle follows from (2.3) i.e. by scaling the horizontal gradient of the pressure amplitude. Note that in this procedure the harmonic function (2.5) for surface elevation is the single user-controlled input to the Poisson solver.

Per spectral component, the pressure gradients drive the momentum equations (2.2) for the horizontal and vertical velocity components. Section 3.2 starts with the latter because the vertical orbital velocity is used subsequently for vertical advection in the horizontal orbital velocity as treated in Section 3.3.

3.2 Solving the vertical orbital velocity per spectral component

This section begins with our motivation for the procedure for solving the vertical orbital velocity per spectral component.

Consider a 3D shallow-water solver in which the pressure is approximated by the hydrostatic pressure. In this solver, the vertical velocity is obtained by vertical integration, of the divergence of the horizontal velocity vector from the bed ($z=0$) upward:

$$w(\zeta) - w(0) = - \int_0^{\zeta} \left(\frac{\partial u}{\partial x} + \frac{\partial v}{\partial y} \right) dz \quad . \quad (3.11)$$

This integration then yields the vertical velocity at the free surface. In virtue of mass conservation, the free-surface vertical velocity $w(\zeta)$ must be compatible with the material derivative of the surface elevation ζ i.e.

$$\frac{\partial \zeta}{\partial t} + u(\zeta) \frac{\partial \zeta}{\partial x} + v(\zeta) \frac{\partial \zeta}{\partial y} = w(\zeta) \quad . \quad (3.12)$$

This compatibility condition couples the (depth-integrated) horizontal momentum equations to the depth-integrated incompressibility condition $\nabla \cdot \underline{u} = 0$. The latter coupling yields an equation in term of the horizontal velocity components (u, v) as well as the yet unknown ζ but with the vertical velocity eliminated. Once this coupled set is solved, the vertical profile of the vertical velocity follows from (3.11) without using the vertical momentum equation. The latter neglect yields a passive or reactive response of vertical velocity mostly as a kinematic closure to the incompressibility condition rather than a dynamic response to forcing.

Indeed, extensive experience with the previous solution procedure learns that the passive response of the vertical velocity does not yield the correct vertical motion of, for instance, a heavy or light blob of water. Instead, the hydrodynamic solver (Casulli and Stelling, 1998) can solve this problem correctly because the first estimate for the vertical velocity is derived from its momentum equation in which vertical forces and hydrodynamic pressure gradients are included. This analysis and experience motivates our choice in solving a particular sequence of momentum equations.

For the purpose of investigating which terms are significant in wave-current interaction, therefore the vertical velocity is solved here first by its simplified momentum equation. The vertical momentum equation is driven by the vertical hydrodynamic pressure gradient. This solution procedure allows for the application of the compatibility condition (3.12) but it does not guarantee the incompressibility condition (3.11). Tests with the POINT SAND model, however, show that the deviations from (3.12) appear small although a distinct

criterion for approximating (3.12) is lacking. A dedicated proof of approximating (3.12) is implementing a transport equation for a conserved scalar and checking the temporal deviations from an initially uniformly-distributed constituent.

Thus the vertical orbital velocity is solved through a simplified momentum equation. As announced in Section 3.1, not all advection terms in (2.2) are included in the simulation and most of them are removed for solving the vertical orbital velocity. The following linearized momentum equation for the vertical orbital-velocity component is adopted:

$$\frac{\partial \tilde{w}}{\partial t} + \underline{U}(z) \cdot \nabla \tilde{w} + \frac{\partial \tilde{p}}{\partial z} = \frac{\partial}{\partial z} \left\{ 2(\nu + f_{hp} \nu_T) \frac{\partial \tilde{w}}{\partial z} \right\} . \quad (3.13)$$

Note that inconsistent with the Poisson equation (3.1) and its boundary condition (3.5), the vertical momentum equation (3.13) is extended with the influence of turbulence on the vertical orbital velocity component. The inclusion of vertical advection has been tested but it overestimates the vertical velocity near the bed, probably because the solution procedure for the vertical pressure gradient does not account for this non-linearity but more analysis is recommended.

The RHS of (3.13) contains the vertical exchange of mean horizontal momentum with ν the kinematic viscosity and ν_T the eddy viscosity. In (3.13), the horizontal gradient of the Reynolds shear stress:

$$\frac{\partial}{\partial x} \left\{ (\nu + f_{hp} \nu_T) \left(\frac{\partial \tilde{u}}{\partial z} + \frac{\partial \tilde{w}}{\partial x} \right) \right\} ; \quad \frac{\partial}{\partial y} \left\{ (\nu + f_{hp} \nu_T) \left(\frac{\partial \tilde{v}}{\partial z} + \frac{\partial \tilde{w}}{\partial y} \right) \right\} .$$

are neglected. These minor terms contain complicated estimates for horizontal gradients of $\partial \tilde{u} / \partial z$ and $\partial \tilde{w} / \partial x$. Particularly in view of (2.4), the horizontal derivative of the latter would involve second-order temporal derivatives of \tilde{w} .

In (3.13), the eddy viscosity ν_T is reduced by a (high-pass) filter-function f_{hp} that depends on wave angular frequency of the particular spectral component. The product of this filter function and the total eddy viscosity represents the reduced eddy viscosity due to turbulent motions that respond sufficiently fast to the orbital shear rates; see Chapter 4 for more details.

On the impermeable bed we have

$$\tilde{w} = 0 \quad (3.14)$$

The surface condition needs more elaboration for both orbital velocity components as well as for the mean flow and therefore the stress balance at the surface is considered first. The following formulations are applied at the still water level (rigid-lid approximation) rather than at the mobile free surface. This simplification is considered as a crude one but tests show it works sufficiently well.

Continuity of pressure as well as zero tangential shear stresses on the water surface demand, in absence of wind:

$$z = \bar{\zeta}: \quad \sigma_{xx}n_x + \sigma_{xz}n_z = 0 \quad ; \quad \sigma_{xz}n_x + \sigma_{zz}n_z = 0 \quad \text{with} \quad \frac{n_x}{n_z} = -\frac{\partial \tilde{\zeta}}{\partial x} \quad . \quad (3.15)$$

This is the simplest approximation to the free-surface condition at it is of zero order accuracy neglecting the surface elevation. In (3.15), σ_{ij} ($i,j=1,2,3$ or x,y,z) are the deviatoric stress components and (n_x, n_z) are the components of the upward-directed normal to the water surface of which its mean inclination, due to mean horizontal pressure gradient, is neglected. The stresses are due to molecular motions as well as due to Reynolds stresses which are closed by introducing an isotropic eddy viscosity. Combining the two stress balances in (3.15) yields:

$$z = \bar{\zeta}: \quad \sigma_{zz} = \left(\frac{n_x}{n_z} \right)^2 \sigma_{xx} \quad (3.16)$$

and thus σ_{zz} is of third-order in wave amplitude so that at least to first-order, the boundary condition for vertical orbital velocity reads:

$$z = \bar{\zeta}: \quad \frac{\partial \tilde{w}}{\partial z} = 0 \quad . \quad (3.17)$$

Further, from the first condition in (3.15) as well as the stress closures follows:

$$z = \bar{\zeta}: \quad \frac{\partial U}{\partial z} + \frac{\partial \tilde{u}}{\partial z} + \frac{\partial \tilde{w}}{\partial x} = 2 \frac{\partial \tilde{u}}{\partial x} \frac{\partial \tilde{\zeta}}{\partial x} \quad (3.18)$$

so that to first-order in wave amplitude, for the horizontal orbital velocity:

$$z = \bar{\zeta}: \quad \frac{\partial \tilde{u}}{\partial z} = -\frac{\partial \tilde{w}}{\partial x} \quad (3.19)$$

holds because the mean of (3.18) demands for the mean vertical shear rate:

$$z = \bar{\zeta}: \quad \frac{\partial U}{\partial z} = 2 \overline{\frac{\partial \tilde{u}}{\partial x} \frac{\partial \tilde{\zeta}}{\partial x}} \quad . \quad (3.20)$$

The horizontal gradient in the linearized material derivative is converted through (2.4) into a temporal derivative i.e.

$$\frac{\partial \tilde{w}}{\partial t} + U(z) \frac{\partial \tilde{w}}{\partial x} + V(z) \frac{\partial \tilde{w}}{\partial y} \equiv \left(1 - \frac{k \cdot U(z)}{\omega} \right) \frac{\partial \tilde{w}}{\partial t} \quad (3.21)$$

The momentum equation (3.13) for the vertical orbital-velocity component and its boundary conditions (3.14) and (3.19) are solved on the same grid as the wave-related pressure. The vertical velocity is defined at vertical cell interfaces where also the vertical pressure gradient has been defined. In this staggered mesh, condition (3.14) can be imposed on the bed and the zero normal-stress condition (3.16) closes diffusion in (3.13) at the free surface.

Equation (3.13) is solved with \tilde{w} as principle unknown and diffusion is integrated with Euler implicit. The pressure gradient in (3.13) is time centred.

Note that first the surface elevation is prescribed in (3.7) and then the hydrodynamic pressure is solved. Subsequently, the vertical orbital velocity is solved by (3.13) and it is driven by the vertical pressure gradient. We believe that this solution sequence is essential for creating the wave-current force that affects the vertical profile of the mean horizontal velocity. The overview report (Uittenbogaard, 2000) illustrates this sequence. In the next section, this role of the vertical orbital velocity will become more apparent.

3.3 Solving the horizontal orbital velocity of a single spectral component

Our numerical simulations have shown that the vertical advection, by orbital velocity \tilde{w} , of horizontal orbital momentum is responsible for creating the major contribution to the wave-induced force that affects the vertical profile of the mean horizontal velocity. Rather than modelling this momentum transfer, the creation of this force is simulated directly by solving the non-linear momentum equation for the horizontal orbital velocity.

The equation for the horizontal orbital velocity is arranged such that it allows for the simulation of the orbital motions as part of a given wave number spectrum of surface elevations. Therefore, we start with (2.2) for a horizontal mean flow. Initially, we neglect the RHS of (2.2) but later we include the unbalance of turbulence stresses. For the purpose of solving orbital motions for a given spectrum, the orbital velocity in (2.2) is replaced by the sum

$$\tilde{u} \rightarrow \underline{\tilde{u}} + \tilde{v} \quad (3.22)$$

where \tilde{v} represents all other contributions at wave numbers that differ from wave number k belonging to $\underline{\tilde{u}}$. Formally we thus define

$$\underline{\tilde{u}} = \underline{\tilde{u}}(\omega_s) \quad ; \quad \tilde{v} = \sum_{n \neq s} \underline{\tilde{u}}(\omega_n) \quad (3.23)$$

with ω_n ($n=1,2,3,\dots$) the angular frequencies of the spectral components defined by the user. The previous decomposition is applied to (2.2) and it reads

$$\frac{\partial \tilde{\underline{u}} + \tilde{\underline{v}}}{\partial t} + (\underline{U} + \tilde{\underline{u}} + \tilde{\underline{v}}) \cdot \nabla (\tilde{\underline{u}} + \tilde{\underline{v}}) + (\tilde{\underline{u}} + \tilde{\underline{v}}) \cdot \nabla \underline{U} + \nabla (\tilde{p}_u + \tilde{p}_v) = \underline{0} \quad (3.24)$$

where p_u is the pressure related to the orbital velocity $\tilde{\underline{u}}$ and likewise p_v is related to $\tilde{\underline{v}}$. An obvious decomposition of (3.24) are the following momentum equations for $\tilde{\underline{u}}$ and $\tilde{\underline{v}}$ separately:

$$\frac{\partial \tilde{\underline{u}}}{\partial t} + (\underline{U} + \tilde{\underline{u}} + \tilde{\underline{v}}) \cdot \nabla \tilde{\underline{u}} + \tilde{\underline{u}} \cdot \nabla \underline{U} + \nabla \tilde{p}_u = \underline{0} \quad (3.25)$$

$$\frac{\partial \tilde{\underline{v}}}{\partial t} + (\underline{U} + \tilde{\underline{u}} + \tilde{\underline{v}}) \cdot \nabla \tilde{\underline{v}} + \tilde{\underline{v}} \cdot \nabla \underline{U} + \nabla \tilde{p}_v = \underline{0} \quad (3.26)$$

The sum of (3.25) and (3.26) equals (3.24). Of course, (3.26) can be decomposed further into other wave number components.

Next, a convenient simplification is introduced that allows for solving just one horizontal momentum equation per wave number or angular frequency rather than solving two equations for the two horizontal orbital velocity components. This simplification is based on the linearized version

$$\frac{\partial \tilde{\underline{u}}}{\partial t} + \underline{U} \cdot \nabla \tilde{\underline{u}} + \tilde{\underline{u}} \cdot \nabla \underline{U} + \nabla \tilde{p}_u = \underline{0} \quad (3.27)$$

of the non-linear momentum equation (3.25). Appendix B shows that the orbital velocity vector can be decomposed as:

$$\tilde{\underline{u}} = \tilde{u} \hat{\underline{k}} + \tilde{w} \hat{\underline{m}} \quad ; \quad \hat{\underline{k}} = \frac{\underline{k}}{|\underline{k}|} \quad ; \quad |\hat{\underline{m}}| = 1 \quad ; \quad \hat{\underline{m}} \cdot \hat{\underline{k}} = 0 \quad (3.28)$$

In (3.28), $\hat{\underline{k}}$ is the unit vector parallel to the (horizontal) wave number \underline{k} and the unit vector $\hat{\underline{m}}$ is directed against gravity. The essential aspect of (3.28) is that the horizontal part of the orbital velocity vector is parallel to its wave number vector \underline{k} . For surface waves propagating with some angle to a flow having vertical velocity profile, the latter is not obvious. Nevertheless, Appendix B shows that this parallelism is approximated excellently. The convenient consequence of this parallelism becomes apparent after the scalar multiplication of (3.25) with the horizontal unit vector $\hat{\underline{k}}$ yielding:

$$\frac{\partial \tilde{u}}{\partial t} + \left\{ (\underline{U} + \tilde{\underline{v}}) \cdot \hat{\underline{k}} + \tilde{u} \right\} \frac{\partial \tilde{u}}{\partial x_k} + \tilde{w}_u \frac{\partial \tilde{u}}{\partial z} + \tilde{w}_u \frac{\partial \underline{U} \cdot \hat{\underline{k}}}{\partial z} + \frac{\partial \tilde{p}_u}{\partial x_k} = 0 \quad (3.29)$$

with x_k the horizontal co-ordinate in positive \underline{k} direction and \tilde{w}_u the vertical component of $\tilde{\underline{u}}$ all related to a single spectral component. Thus (3.29) is a single horizontal momentum equation obtained by projection of the "external" flow field $(\underline{U} + \tilde{\underline{v}})$ on the direction \underline{k}

rather than splitting the horizontal part of $\tilde{\mathbf{u}}$ with respect to horizontal directions parallel and normal to e.g. $\underline{\mathbf{U}}$. The horizontal momentum equation (3.29) shows that the vertical gradient of the mean horizontal velocity vector is significant only if it has a component parallel to $\underline{\mathbf{k}}$. Likewise, there is advection by $(\underline{\mathbf{U}} + \tilde{\mathbf{v}})$ provided $(\underline{\mathbf{U}} + \tilde{\mathbf{v}})$ has a component in the direction $\underline{\mathbf{k}}$ of wave propagation.

Note that (3.29) for the horizontal vector $\tilde{\mathbf{u}}$ contains the following linear and non-linear (wave-wave) interaction terms:

	$\underline{\mathbf{U}}$	$\tilde{\mathbf{v}}$	$\tilde{\mathbf{u}}$
$\underline{\mathbf{U}}$	$\underline{\mathbf{U}} \cdot \nabla \underline{\mathbf{U}}$	$\underline{\mathbf{U}} \cdot \nabla \tilde{\mathbf{v}}$	$\underline{\mathbf{U}} \cdot \nabla \tilde{\mathbf{u}}$
$\tilde{\mathbf{v}}$	$\tilde{\mathbf{v}} \cdot \nabla \underline{\mathbf{U}}$	$\tilde{\mathbf{v}} \cdot \nabla \tilde{\mathbf{v}}$	$\tilde{\mathbf{v}} \cdot \nabla \tilde{\mathbf{u}}$
$\tilde{\mathbf{u}}$	$\tilde{\mathbf{u}} \cdot \nabla \underline{\mathbf{U}}$	$\tilde{\mathbf{u}} \cdot \nabla \tilde{\mathbf{v}}$	$\tilde{\mathbf{u}} \cdot \nabla \tilde{\mathbf{u}}$

Table 1 Overview of linear and non-linear (wave-wave) interaction terms in (3.29)

In the following the reference to wave number $\underline{\mathbf{k}}$ in the horizontal co-ordinate x_k is omitted. Instead, x_k is replaced by co-ordinate x parallel to the direction of wave propagation. Likewise, \tilde{w} is written in place of \tilde{w}_u and also \tilde{p} in place of \tilde{p}_u . We believe these notational simplifications do not create ambiguity because they all relate to the horizontal velocity subject of the equation in which they appear. Consequently (3.29), extended with the RHS of (2.2), reads:

$$\frac{\partial \tilde{\mathbf{u}}}{\partial t} + \left\{ (\underline{\mathbf{U}} + \tilde{\mathbf{v}}) \cdot \hat{\mathbf{k}} + \tilde{\mathbf{u}} \right\} \frac{\partial \tilde{\mathbf{u}}}{\partial x} + \tilde{w} \frac{\partial \tilde{\mathbf{u}}}{\partial z} + \tilde{w} \frac{\partial \underline{\mathbf{U}} \cdot \hat{\mathbf{k}}}{\partial z} + \frac{\partial \tilde{p}}{\partial x} = \frac{\partial}{\partial x} \left\{ 2(\nu + f_{hp} \nu_T) \frac{\partial \tilde{\mathbf{u}}}{\partial x} \right\} + \frac{\partial}{\partial z} \left\{ (\nu + f_{hp} \nu_T) \left(\frac{\partial \tilde{\mathbf{u}}}{\partial z} + \frac{\partial \tilde{w}}{\partial x} \right) \right\} - T_x \tag{3.30}$$

In (3.30) the spatial derivative in the transverse (y) direction as well as the corresponding transverse velocity component are omitted by the approximation presented in Appendix B. Further, the x-direction in (3.30) is parallel to the direction $\underline{\mathbf{k}}$ of wave propagation.

The terms

$$\tilde{\mathbf{u}} \frac{\partial \tilde{\mathbf{u}}}{\partial x} + \tilde{\mathbf{v}} \cdot \hat{\mathbf{k}} \frac{\partial \tilde{\mathbf{u}}}{\partial x} + \tilde{w} \frac{\partial \tilde{\mathbf{u}}}{\partial z} \tag{3.31}$$

see also Table 1, represent the *non-linear advection terms* in the POINT SAND model of which

$$\tilde{w} \frac{\partial \tilde{u}}{\partial z} \tag{3.32}$$

as part of $\tilde{\mathbf{v}} \cdot \nabla \underline{\mathbf{U}}$ in Table 1, appears to be the most prominent one for the experiments of Klopman (1994).

The horizontal orbital pressure gradient that drives (3.30) follows from the hydrodynamic pressure (Section 3.1) as well as from (2.4) for expressing the horizontal derivative into temporal derivative which is defined time centred.

Note that, except T_x , all terms in the RHS of (3.30) are due to the molecular and the turbulence stresses that we neglected upon deriving the linearized Poisson equation (3.1).

Below simplifications to the stress terms in the RHS of (3.30) are considered. First define F_x according to the RHS of (3.30), excluding the WCI force T_x , as:

$$F_x = \frac{\partial}{\partial x} \left\{ 2(v + f_{hp} v_T) \frac{\partial \tilde{u}}{\partial x} \right\} + \frac{\partial}{\partial z} \left\{ (v + f_{hp} v_T) \frac{\partial \tilde{u}}{\partial z} \right\} + \frac{\partial}{\partial z} \left\{ (v + f_{hp} v_T) \frac{\partial \tilde{w}}{\partial x} \right\} \tag{3.33}$$

Subsequently, the horizontal variations in eddy viscosity v_T and in the high-pass filter function f_{hp} are neglected. The argumentation for this neglect is that near the bed where f_{hp} is large the horizontal gradients are small compared to vertical gradients. Further, the horizontal derivative is replaced by the temporal derivative using (2.4) and the second-order derivative by exploiting the periodicity assumption (2.3). Consequently, F_x then reads

$$F_x = -2k^2 (v + f_{hp} v_T) \tilde{u} + \frac{\partial}{\partial z} \left\{ (v + f_{hp} v_T) \frac{\partial \tilde{u}}{\partial z} \right\} - \frac{k}{\omega} \frac{\partial}{\partial z} \left\{ (v + f_{hp} v_T) \frac{\partial \tilde{w}}{\partial t} \right\} \tag{3.34}$$

The approximation (3.34) to (3.33) is used in (3.30) because it contains derivatives that are known in the POINT SAND model. This ends the treatment of the stress terms in (3.30) in the horizontal orbital momentum equation implemented in the POINT SAND model.

Another subject is the sequence of solving the various spectral components of the orbital motions. This sequence plays a role in computing the advection because this term contains most of the wave-wave interaction. The horizontal advection terms are approximated by

$$\frac{\partial \tilde{u}}{\partial t} + \left\{ (\underline{\mathbf{U}} + \tilde{\mathbf{v}}) \cdot \hat{\mathbf{k}} + \tilde{u} \right\} \frac{\partial \tilde{u}}{\partial x} = \left\{ 1 - \frac{k}{\omega} [(\underline{\mathbf{U}} + \tilde{\mathbf{v}}) \cdot \hat{\mathbf{k}} + \tilde{u}] \right\} \frac{\partial \tilde{u}}{\partial t} \Big|_{t+\frac{1}{2}\Delta t} \tag{3.35}$$

with $\Delta t^{(orb)}$ the time step applied in the *inner loop*. For more than one spectral component, the advection (3.35) is solved in a loop that starts with the lowest angular frequency. For solving the orbital motions at angular frequency ω_s , with s some integer label, the other orbital velocity vectors are split into two groups as

$$\hat{k} \cdot \tilde{v} = \hat{k} \cdot \tilde{u}^{(-)} + \hat{k} \cdot \tilde{u}^{(+)} \tag{3.36}$$

with

$$\tilde{u}^{(-)}\left(t + \frac{1}{2} \Delta t^{(orb)}\right) = \sum_{n < s} \tilde{u}\left(t + \frac{1}{2} \Delta t^{(orb)}; \omega_n\right) \quad ; \quad \tilde{u}^{(+)}(t) = \sum_{s < n} \tilde{u}(t; \omega_n) \tag{3.37}$$

Here ω_s is the angular frequency implicitly referred to in (3.30). The splitting (3.36) and (3.37) shows that for frequencies lower than ω_s , the velocity at the new time level is used. In principle, a return *sweep* starting with the highest angular frequency can be included, similar to Gauss-Seidel elimination procedure in solving matrix equations. Here we assume that $\Delta t^{(orb)}$ is sufficiently small and short waves are affected mostly by longer waves than vice versa and we neglect the return sweep.

The approximation (3.35) and the solution sequence defined by (3.36) and (3.37) in the (intra-wave) *inner loop* are implemented in the POINT SAND model.

The vertical advection (3.32) of horizontal orbital momentum is defined in the centre of the m^{th} cell and it is discretized by

$$\tilde{w} \left. \frac{\partial \tilde{u}}{\partial z} \right|_m = \left\{ \frac{1}{2} - \theta \text{sign}(\tilde{w}_{m+\frac{1}{2}}) \right\} \tilde{w} \left. \frac{\partial \tilde{u}}{\partial z} \right|_{m-1} + \left\{ \frac{1}{2} + \theta \text{sign}(\tilde{w}_{m+\frac{1}{2}}) \right\} \tilde{w} \left. \frac{\partial \tilde{u}}{\partial z} \right|_m \tag{3.38}$$

with θ for weighting central ($\theta=0$) and first-order upwind ($\theta=0.5$) schemes. For simulating the wave-current experiments of (Klopman, 1994) with 100 equidistant layers and 100 time steps per wave period, the central scheme does not wiggle but for safety we set $\theta=0.1$. Because the vertical orbital velocity is also known at the new time level, the LHS of (3.38) is time-centred and the gradient $\partial \tilde{u} / \partial z$ at the new time level is treated implicitly.

The discrete representation of the horizontal-momentum equation (3.30) is formulated with $\partial \tilde{u} / \partial z$ as principle unknown and using Hermite interpolation similar to (3.3):

$$\tilde{u}_m - \tilde{u}_{m+1} = \alpha_m \left(\frac{\partial \tilde{u}}{\partial z} \right)_{m-1} + \beta_m \left(\frac{\partial \tilde{u}}{\partial z} \right)_m + \gamma_m \left(\frac{\partial \tilde{u}}{\partial z} \right)_{m+1} \quad , \tag{3.39}$$

with weight factors: $\beta_m = \frac{1}{2} (\Delta z_m + \Delta z_{m+1}) \quad ; \quad \alpha_m \equiv \gamma_m = 0 \quad .$

The Hermite interpolation (3.39), however, allows for a weighting matched to a strongly non-equidistant grid such as a logarithmic distribution can be used without loss of accuracy. The latter requires weight factors different from those in (3.4) and these are not implemented yet.

Finally, we must design a numerical procedure for force T_x by which the average of the horizontal orbital velocity is negligibly small or zero. With respect to (2.1) and (2.2), the argumentation for such a numerical procedure has been given. We have good experience

with the procedure for adjusting the horizontal pressure gradient in (2.1) for realising a user-defined depth-averaged velocity. This procedure is applied to T_x but for each z -level separately so that at each z -level the average of the horizontal orbital velocity is negligibly small or zero.

Per spectral component with angular frequency ω_s , the recipe then reads

$$T_x(z, (l + \frac{1}{2})T; \omega_s) = \frac{\overline{\tilde{u}(z; \omega_s)}}{T} \quad ; \quad \overline{\tilde{u}(z; \omega_s)} = \frac{1}{T} \int_{lT}^{(l+1)T} \tilde{u}(z, t; \omega_s) dt \quad ; \quad (3.40)$$

$$T = \frac{2\pi}{\omega_s} \quad ; \quad l = 0, 1, 2, 3, \dots$$

In (3.40), the time interval lT to $(l+1)T$ refers to the most recently completed wave cycle of the relevant spectral component with wave period T . This numerical formulation of wave-current force $T_x(z)$ thus follows from averaging, per z -level, the horizontal orbital velocity over the most-recently completed wave cycle, divided by its wave period.

Force $T_x(z)$ represents some acceleration or deceleration of the horizontal orbital velocity such that the average horizontal orbital velocity vanishes. Inversely, T_x represents a momentum exchange between mean flow and orbital motions. Therefore, with the opposite sign, T_x appears in the momentum equation (2.1) for the mean or wave-averaged horizontal velocity. As outlined in Section 2.2, the formulation of T_x by (3.40) is purely numerical and the formulation does not reflect an analytical solution. The mere role of (3.40) is yielding a sufficiently small wave-averaged orbital velocity as well as closing the total force balance with the mean-flow momentum equation. In the summation of (3.30) to the mean-flow momentum equation, yielding the total momentum equation for flow and waves, force $T_x(z)$ vanishes. In general $T_x(z)$ is z -dependent so that it deforms the mean current profile. The depth-average of T_x must be balanced by adjusting the hydrostatic pressure gradient in (2.1) for achieving the user-defined depth-averaged velocity.

The formulation (3.40) is implemented in the POINT SAND model. In the subroutine AVERAG the time integration in (3.40) is ended and re-initialised at every second zero crossing of $\tilde{\zeta}(t; \omega_s)$. Note that there is a time lag in the WCI force per spectral component depending on the time step in the *outer loop* as well as the period of the particular spectral component. Moreover, after completion of a wave cycle, the WCI force is updated and this creates a jump in WCI force in the mean-momentum equation. For a monochromatic wave this jump is not serious as it disappears upon convergence to stationary conditions. For multi-component waves, however, the wave-wave interactions create ongoing oscillations in the respective WCI forces and the sum of these forces perturb the mean momentum and this sum can create e.g. subharmonic quite faithfully. In the latter case, however, the jumps in WCI force create a non-convergence in the mean flow solution, irrespective of the time step in the *outer loop*. For obtaining convergence therefore the WCI forces are adjusted gradually over the respective wave period. The following procedure (3.41) is designed for that purpose. In (3.41), η represents the gradually adjusted T_x from the old value η_0 to the new prediction η_∞ for T_x . This prediction is based on (3.40) and it reads $\eta_\infty = 2 \cdot T_x(\text{new}) - T_x(\text{old})$ with $T_x(\text{new})$ defined by the latest evaluation of (3.40) over the most recently completed wave cycle and $T_x(\text{old})$ the former cycle. The differential equation

$$\frac{d\eta}{d\tau} = \alpha \tau (\eta_{\infty} - \eta) \tag{3.41}$$

has the temporal solution $\eta = \eta_0 + \eta_{\infty} \{1 - \exp(-\frac{1}{2} \alpha \tau^2)\}$ with time τ and this solution changes gradually from η_0 to η_{∞} . Inspired by (3.41), the change in WCI force after a wave cycle is gradually adjusted by the finite difference scheme

$$\eta^{(n+1)} = \eta^{(n)} + \frac{n\alpha}{N^2} (\eta_0 - \eta^{(n)}) \quad ; \quad n = 1, 2, \dots, N \quad , \tag{3.42}$$

where N is the number of time steps in the *inner* loop covering one wave period and integer n is the counter which is reset to $n=0$ after every second zero crossing of the surface elevation. In (3.42), α is taken so that $\eta^{(N)} - \eta_0 = r(\eta_{\infty} - \eta_0)$ which requires $\alpha = -\ln\{(1-r)^2\}$. This prediction is based on (3.40) and it reads $\eta_{\infty} = 2 \cdot T_x(\text{new}) - T_x(\text{old})$ with $T_x(\text{new})$ defined by the latest evaluation of (3.42) and $T_x(\text{old})$ the result of (3.42) at the completion of the most recent wave cycle. For bichromatic waves this approach yields converged solutions.

As derived in the previous section, see (3.19), the conditions for a stress-free surface demand to zero order in wave amplitude:

$$z = \bar{\zeta}: \quad \frac{\partial \tilde{u}}{\partial z} = -\frac{\partial \tilde{w}}{\partial x} = \frac{k}{\omega} \frac{\partial \tilde{w}}{\partial t} \quad . \tag{3.43}$$

In case of a free surface subjected to wind shear stress, the condition (3.43) still holds when the wind shear stress does not vary in the rhythm of the surface waves.

The bed condition for orbital motions can be based on a turbulent boundary layer i.e. a partial slip condition or viscous sublayer i.e. the no-slip condition.

The partial slip condition for a turbulent flow over a hydraulically rough bed requires subtle definition for obtaining results independent of the thickness $\Delta z(k_{\max})$ of the computational bed boundary layer. In literature on 1DV models for orbital motions we found insufficient details for reference and therefore we present our procedure in detail (see also Appendix C).

Therefore, the well-known quadratic friction law is applied for the bed shear stress:

$$(\nu + \nu_T) \left(\frac{\partial U}{\partial z} + \frac{\partial \tilde{u}}{\partial z} \right) \Big|_{z=z_0} = \frac{|\bar{u} + \tilde{u}| (\bar{u} + \tilde{u})}{S^2} \Big|_{z=\frac{1}{2} \Delta z_{k \max}} \tag{3.44}$$

with

$$S = \frac{1}{\kappa} \log \left(1 + \frac{\frac{1}{2} \Delta z_{k \max}}{z_0} \right) ; \quad \kappa = 0.41 \quad , \quad (3.45)$$

for a quasi-steady log-layer with roughness length z_0 1/30 of the Nikuradse length scale k_s . In (3.44), the filter function f_{hp} has been set to unity because in the bed boundary layer, turbulence is sufficiently fast for responding in a quasi-steady fashion to the imposed orbital shear rates. The latter is substantiated in Chapter 4. In (3.45), the level $\frac{1}{2} \Delta z_{k \max}$ refers to the first computational velocity point above the bed.

According to the standard procedure for solving the mean momentum equation in the original DPM, (3.30) is discretized on a staggered grid with velocity \tilde{u} in cell centre and its vertical gradient on cell interfaces. The principle unknown is $\partial \tilde{u} / \partial z$ and Hermite interpolation similar to (3.3) is applied with diffusion Euler implicit. Further, the bed boundary condition using the quadratic bed friction is solved semi-implicitly by products of flow variables at old and new time levels. To that purpose, the vertical gradient of the horizontal velocity is coupled to the near-bed velocity at the new time level as explained below.

From (3.44) follows the wave-induced part of the bed shear stress vector which has zero mean:

$$\tilde{\tau}_b = (\nu + f_{hp} \nu_T) \frac{\partial \tilde{u}}{\partial z} \Big|_{z_0} = S^{-2} (|\underline{u}| \underline{u} - \overline{|\underline{u}| \underline{u}}) \Big|_{\frac{1}{2} \Delta z_{k \max}} \quad (3.46)$$

Decomposed into mean and orbital motions the previous equation reads

$$\tilde{\tau}_b = (\nu + f_{hp} \nu_T) \frac{\partial \tilde{u}}{\partial z} \Big|_{z_0} = S^{-2} (|\underline{U} + \tilde{u}| \underline{U} + |\underline{U} + \tilde{u}| \tilde{u} - \overline{|\underline{u}| \underline{u}}) \Big|_{\frac{1}{2} \Delta z_{k \max}} \quad (3.47)$$

For the purpose of Hermite interpolation a connection between orbital velocity and its vertical gradient is desired and this relation follows from re-arranging the previous equation into:

$$S^{-2} (|\underline{U} + \tilde{u}| \tilde{u}) \Big|_{\frac{1}{2} \Delta z_{k \max}} - (\nu + f_{hp} \nu_T) \frac{\partial \tilde{u}}{\partial z} \Big|_{z_0} = S^{-2} (\overline{|\underline{u}| \underline{u}} - |\underline{U} + \tilde{u}| \underline{U}) \Big|_{\frac{1}{2} \Delta z_{k \max}} \quad (3.48)$$

or after division by $S^{-2} |\underline{U} + \tilde{u}| \Big|_{\frac{1}{2} \Delta z_{k \max}}$:

$$\tilde{u} \left(\frac{1}{2} \Delta z_{k \max} \right) - (\nu + f_{hp} \nu_T) \frac{\partial \tilde{u}}{\partial z} \Big|_{z_0} = \frac{\overline{|\underline{u}| \underline{u}}}{|\underline{U} + \tilde{u}| \Big|_{\frac{1}{2} \Delta z_{k \max}}} - U \left(\frac{1}{2} \Delta z_{k \max} \right) \quad (3.49)$$

At the bed all turbulent motions are smaller as well as faster than the orbital motions so that $f_{hp}=1$. Further, the time levels are considered for implicit integration so that the previous equation yields:

$$\begin{aligned} \tilde{u}\left(\frac{1}{2} \Delta z_{k \max}, t+\Delta t\right) - \frac{\left[\nu+\nu_T\left(z_0, t\right)\right] S^2}{\left|U+\tilde{u}\left(\frac{1}{2} \Delta z_{k \max}, t\right)\right|} \frac{\partial \tilde{u}(z, t+\Delta t)}{\partial z} \Bigg|_{z_0} = \\ \frac{\left|U+\tilde{u}\left(\frac{1}{2} \Delta z_{k \max}, t\right)\right|}{\left|U+\tilde{u}\left(\frac{1}{2} \Delta z_{k \max}, t\right)\right|_{\frac{1}{2} \Delta z_{k \max}}} - U\left(\frac{1}{2} \Delta z_{k \max}, t\right) \end{aligned} \tag{3.50}$$

The LHS of (3.50) contains the desired implicit coupling for the new time level in the *inner* loop in which (3.30) is solved and all variables in the RHS of (3.50) are defined at previous time level(s).

Comments

Note that the definition (3.30) of T_x is not based on an analytic model for the wave-current force. The sole purpose of T_x is obtaining such a small mean horizontal orbital velocity that this mean value can be neglected in the horizontal orbital momentum equation (3.30).

The principle purpose of T_x is that, once convergence is obtained, its precise formulation is irrelevant provided the horizontal orbital momentum equation is added to the mean horizontal momentum equation (2.1). This addition eliminates T_x but the true mean Eulerian velocity is $U(z)+\tilde{u}(z)$ rather than just $U(z)$.

4 Turbulence closure

4.1 High-pass filter function for wave-turbulence interaction

Laboratory experiments of Jiang et al. (1990) with wind-driven surface waves over a turbulent flow have shown marginal wave-turbulence interaction. Therefore, the inclusion of the full eddy viscosity in the closure for the stress tensor of (2.2) would overestimate significantly the orbital Reynolds stresses and likewise the turbulence production by orbital shear rates in most of the fluid volume. On the other hand, however, there is notable turbulence production in the boundary layer so that neglecting wave-turbulence interaction is not correct for the entire fluid volume.

Therefore, this section considers a simple model for determining the high-pass filter function f_{hp} that was introduced in (3.13) and (3.30). This function reduces the total eddy viscosity to a smaller one that represents the exchange wave momentum just by sufficiently fast turbulent motions. To that purpose we repeat the derivation of the eddy viscosity defined as the product $\langle w'^2 \rangle \tau_L$ between the variance $\langle w'^2 \rangle$ of the vertical turbulent velocity component and its correlation time scale τ_L . Subsequently, we estimate the reduced variance $\langle w'^2 \rangle$ of turbulent motions with time scale faster than the wave period as well as the corresponding reduction in correlation time scale τ_L . The two reductions are compared to the original magnitudes of $\langle w'^2 \rangle$ and τ_L and this comparison yields the low-pass filter function $0 \leq f_{hp} \leq 1$ that depends on the angular frequency of the particular spectral wave component and the time and z -dependent turbulent properties as predicted by some turbulence model.

This function represents the response of sufficiently-fast turbulence to orbital shear rates with angular frequency ω . Note that in the experiments of Klopman (1994) the horizontal wave length is about five times the water depth. Therefore, all major energy containing turbulence wave lengths are sufficiently short for interacting with the imposed spatial variations in orbital shear rate. Consequently, in this particular case, the problem of wave-turbulence interaction reduces to modelling just the turbulence response in frequency domain. In the more general case, the high-pass filter function should also include the separation of turbulent shear stress in wave number space.

The derivation of the high-pass filter based solely on separation in frequency domain is presented below.

First, the frequency spectrum of Lagrangian turbulent velocity is estimated. From this spectrum, the fraction of turbulent kinetic energy with minimal frequency ω is estimated and ω is the angular frequency of the surface wave. The formation of orbital Reynolds stresses is set proportional to this energy fraction as well as the reduced time scale and the product of the latter two defines the high-pass filter function f_{hp} .

The frequency spectrum of Lagrangian turbulent velocity is derived as follows. The (Lagrangian) position \underline{X} of a fluid parcel, starting at Eulerian position \underline{x} at time t is defined formally by

$$\underline{X}(0) = \underline{x}: \frac{d\underline{X}(\tau)}{d\tau} = \underline{u}(\underline{X}, t + \tau) \quad (4.1)$$

with total derivative $d/d\tau$ with respect to flight time τ of the fluid parcel starting at \underline{x} and \underline{u} is the total velocity of the fluid. The Lagrangian autocorrelation coefficient ρ_{uu} for a single velocity component is then defined by (Tennekes and Lumley, 1972, eq. 7.1.4)

$$\rho_{uu}(\tau; \underline{x}, t) = \frac{\langle u'(\underline{x}, t) u'(\underline{X}, t + \tau) \rangle}{\langle u'^2(\underline{x}, t) \rangle} \quad (4.2)$$

The brackets $\langle \dots \rangle$ imply ensemble averaging over turbulence; the variables after the semicolon in (4.2) are considered as parameters. If turbulence is superimposed on a time-varying mean flow then the formalism of turbulence with stationary increments could be introduced, see (Monin and Yaglom, 1975, part II, sec. 13.1). For turbulence in a wave-affected flow, the procedure would be to define turbulence superimposed on a mean flow that is locally linearized in time, i.e. turbulence with stationary first increments, and by applying phase averaging as the appropriate ensemble-averaging operation. Nevertheless, the consequences for the design of the following simple model for the high-pass filter function f_{hp} are equivalent to the following considerations for stationary turbulence.

For stationary turbulence, the definition of the so-called integral Lagrangian time scale reads (Tennekes and Lumley, 1972, eq. 2.3.17):

$$\tau_L = \int_0^\infty \rho_{uu}(\tau) d\tau \quad (4.3)$$

The derivation of eddy diffusivity Γ_T then yields (Tennekes and Lumley, 1972, eq. 7.1.14):

$$\Gamma_T = \lim_{\tau \rightarrow \infty} \frac{d \frac{1}{2} \langle X'^2(\tau) \rangle}{d\tau} = \langle u'^2(\underline{x}, t) \rangle \tau_L \quad (4.4)$$

and the usual closure assumption is that eddy viscosity is proportional to Γ_T , the coefficient of proportionality is about unity and it is called the turbulence Prandtl/Schmidt number, see e.g. (Rodi, 1984).

Here the interest is on eddy viscosity related to the orbital Reynolds stresses due to turbulence with angular frequency ω or larger. The high-pass filter function is now defined as:

$$f_{hp}(\omega) \equiv \frac{\Gamma_T(\omega)}{\Gamma_T(0)} \quad (4.5)$$

with $\Gamma_T(\omega)$ the eddy diffusivity of turbulent motions responding to shear rates imposed at angular frequency ω . Consequently, according to (4.4) and (4.5), two estimates should be made for defining the high-pass function. The first estimate concerns the variance $\langle u'^2(\omega) \rangle$ of turbulent motions with angular frequency exceeding ω . The second and last estimate is the Lagrangian time scale of the high-pass filtered turbulent motions.

The first estimate thus concerns the ratio in velocity variances. Experiments by Sato and Yamamoto (1987) have shown the following approximation to the Lagrangian auto-correlation coefficient (4.2):

$$\rho_{uu}(\tau) = \exp(-\tau / \tau_L) \quad . \quad (4.6)$$

The corresponding (normalised) energy spectrum $E_{uu}(\omega')$ follows from the cosines transform (Hinze, 1975, eq. 1-95a) of (4.6) and it yields:

$$E_{uu}(\omega') = \frac{2}{\pi} \frac{\tau_L}{1 + (\omega' \tau_L)^2} \quad ; \quad \int_0^\infty E_{uu}(\omega') d\omega' = 1 \quad (4.7)$$

so that the ratio of velocity variances becomes

$$\frac{\langle u'^2(\omega) \rangle}{\langle u'^2(0) \rangle} \equiv \int_\omega^\infty E_{uu}(\omega') d\omega' = 1 - \frac{2}{\pi} \arctan(\omega \tau_L) \quad (4.8)$$

and this defines the first estimate.

The second estimate concerns the equivalent time scale of the high-pass filtered turbulence with corrected Lagrangian correlation function:

$$\tau_L(\omega) = \int_0^\infty \rho_{uu}(\tau; \omega) d\tau \quad . \quad (4.9)$$

where ω after the semicolon of the autocorrelation coefficient refers to the high-pass filtering operation on turbulence. In (4.8) appears the product $(\omega\tau_L)$ i.e. ω is inversely connected to the integral time scale. This relation connects the inverse of angular frequency (or wave number) to integral time scale (or length scale) i.e. disregarding the 2π for conversion to period or wave length. The equivalency between integral time scale and the inverse of appropriate angular frequency is typical for turbulence processes, see (Hinze, 1975, chapter 3) for examples. Therefore, (4.9) is approximated by

$$\tau_L(\omega) = \int_0^{\omega^{-1}} \rho_{uu}(\tau) d\tau \quad , \quad (4.10)$$

where ω^{-1} represents the upper limit of time scales of turbulence that responds to oscillations with angular frequency ω . Consequently, the estimate for the ratio in integral time scales reads:

$$\frac{\tau_L(\omega)}{\tau_L(0)} = 1 - \exp\{-(\omega \tau_L)^{-1}\} \quad (4.11)$$

Combining (4.8) and (4.11) in (4.4) for determining the ratio (4.5) yields the high-pass filter function:

$$f_{hp} = \left\{1 - \frac{2}{\pi} \arctan(\omega \tau_L)\right\} \left\{1 - \exp\left[-(\omega \tau_L)^{-1}\right]\right\} \quad (4.12)$$

which, of course, becomes unity for vanishing integral time scale τ_L i.e. when the turbulence is very fast compared to the oscillations in the imposed shear rates. Figure 1 presents the properties of the previous functions and particularly the lower graph for f_{hp} can be used to estimate the thickness of the wave-induced turbulent boundary layer above a rough bed for an estimated profile of $\tau_L(z)$.

Finally, before closing this section, an estimate for the integral Lagrangian time scale proper should be made. As presented in the next section, an eddy viscosity/diffusivity model will be applied. Practically all such turbulence models are based on some analytical expression or transport equation for the turbulent kinetic energy q^2 ; note that q^2 is used here rather than k for avoiding confusion with wave number. Most eddy-viscosity type turbulence models are tuned for estimating the exchange of streamwise momentum or mass in the direction normal to the wall, in the present case that is the vertical direction. The relevant eddy diffusivity then is based on the vertical velocity variance, so from its definition (2.5.4), the integral time scale is expressed in turbulence model variables through

$$\tau_L = \frac{\Gamma_T}{|w'|^2} \quad ; \quad \Gamma_T = \frac{v_T}{\sigma_T} \quad ; \quad |w'|^2 = \alpha q^2 \quad ; \quad q^2 = \frac{1}{2} \langle \underline{u}' \cdot \underline{u}' \rangle \quad (4.13)$$

with empirical coefficient $\alpha \approx 0.25$ for turbulent channel flow, see e.g. (Nezu and Rodi, 1986, fig. 12 and 13) and turbulent Prandtl/Schmidt number $\sigma_T \approx 0.7$. Whether α is wave dependent is not investigated yet. With coefficient α and the turbulent kinetic energy q^2 estimated by the turbulence model, the integral time scale τ_L follows from (4.13) and with the given angular of the surface waves, the high-pass filter function is known at every level. Sufficiently close to a rigid wall, the eddy diffusivity is proportional with wall distance where q^2 is large and nearly constant, see e.g. (Nezu and Rodi, 1986). Consequently, the integral time scale τ_L is proportional with wall distance. The consequence is that practically all energy containing length scales of the fast near-wall turbulence respond to the imposed orbital shear rates with angular frequency ω and so f_{hp} tends to unity and that corresponds to $\tau_L \approx 0$ in (4.12). Therefore, $f_{hp}=1$ has been used in the boundary condition (3.44) for orbital horizontal velocity.

The simple high-pass filter function is devoted to the special case of simulating the experiments of Klopman (1994) i.e. with wave length of surface waves exceeding the water depth significantly. In case of short waves on deep water the truncation in wave number space should also be included in the filter function. The extension of f_{hp} for truncation of turbulence shear stress in wave number space is possible provided the form of the cross spectrum $G_{uw}(k)$ based on turbulent velocity components u' and w' as a function of horizontal wave number magnitude k is known. An estimate for $G_{uw}(k)$ could follow from observations in wave-induced boundary layers and using the decomposition procedure of (Jiang et al., 1990).

Before presenting the turbulence model in the next section, the turbulence production by orbital motions is considered here. The turbulence production is a source term in the transport equation for turbulent kinetic energy. The exact expression for production P_k of turbulent kinetic energy reads:

$$P_k = r_{ij} d_{ij} \quad ; \quad r_{ij} = -\langle u_i' u_j' \rangle \quad ; \quad d_{ij} = \frac{1}{2} \left(\frac{\partial \langle u_i \rangle}{\partial x_j} + \frac{\partial \langle u_j \rangle}{\partial x_i} \right) \quad (4.14)$$

with Reynolds stress tensor r_{ij} , rate-of-deformation tensor d_{ij} and $\langle \cdot \rangle$ represents ensemble-averaging. In case of phase-averaging, e.g. with surface-wave elevation as reference signal, the tensors in (4.14) can be decomposed into mean (written in capitals) and orbital components:

$$r_{ij} = R_{ij} + \tilde{r}_{ij} \quad ; \quad d_{ij} = D_{ij} + \tilde{d}_{ij} \quad . \quad (4.15)$$

For instance, Jiang et al. (1990) applied such a decomposition procedure to turbulence and surface waves.

The application of the well-known eddy-viscosity closure for expressing the deviatoric wave-induced Reynolds stresses into the orbital shear rates then yields for the turbulence production:

$$P_k = 2\nu_T (D_{ij} D_{ij} + f_{hp} \tilde{d}_{ij} \tilde{d}_{ij}) \quad (4.16)$$

and in wave-averaging P_k it is understood that f_{hp} is independent of wave phase i.e. f_{hp} refers to wave-averaged turbulence properties rather than wave-related modulations of the integral time scale.

4.2 Turbulence model

The standard DPM is equipped with the k - ϵ turbulence model and the quasi-equilibrium level 2.5 Mellor-Yamada model which are the prominent models in large-scale civil engineering simulations. The application of these models in the WCI problem showed no difficulties. For the purpose of comparing the results of the hydrodynamic performance of the adapted POINT SAND with (Groeneweg and Klopman, 1998), the k -L turbulence model

they applied is used here as well. For sake of completeness of notation our versions of the k-L and k-ε turbulence models as implemented in the POINT SAND read as follows.

The generic equation for Turbulent Kinetic Energy (TKE) reads:

$$\frac{\partial k}{\partial t} = \frac{\partial}{\partial z} \left\{ (\nu + \nu_T / \sigma_k) \frac{\partial k}{\partial z} \right\} + P_k - \varepsilon - B_k \tag{4.17}$$

Table 4.1 presents closure of (4.17) for the k-L and the k-ε turbulence model.

		k-L model	k-ε model
turbulence production	P_k	see (4.16)	see (4.16)
dissipation rate	ε	$\varepsilon = c_D k^{3/2} / L$	see (4.18)
buoyancy flux	B_k	$\nu_T / \sigma_\rho N^2$	$\nu_T / \sigma_\rho N^2$
eddy viscosity	ν_T	$c_\mu' L \sqrt{k}$	$c_\mu k^2 / \varepsilon$

Table 4.1. Definition and closures for terms in k-L and k-ε turbulence models

The k-ε turbulence model is a two-equation model with the following equation for energy dissipation rate ε:

$$\frac{\partial \varepsilon}{\partial t} = \frac{\partial}{\partial z} \left\{ (\nu + \nu_T / \sigma_\varepsilon) \frac{\partial \varepsilon}{\partial z} \right\} + \frac{\varepsilon}{k} (c_{1\varepsilon} P_k - c_{2\varepsilon} \varepsilon - c_{3\varepsilon} B_k) \tag{4.18}$$

Our version of the k-L model is closed with the flow-independent mixing length L:

$$L = \kappa (9z_0 + z) \sqrt{1 - \frac{9z_0 + z}{\zeta + z_a}} \tag{4.19}$$

which, in principle, is the Bakhmetev profile but with some correction for the length scale at the mean water level and at the bed. For boundary conditions on a hydraulically rough bed we refer to Appendix C.

The last term B_k in (4.17) the buoyancy flux which represents the conversion of turbulent kinetic energy to mean potential energy or vice versa. In (4.17) appears the so-called buoyancy frequency N^2 (see Table 4.1):

$$N^2 = - \frac{g}{\rho} \frac{\partial \rho}{\partial z} \tag{4.20}$$

and the turbulence Prandtl/Schmidt number $\sigma_\rho \approx 0.7$ for conversion of eddy viscosity into eddy diffusivity. We refer to Chapter 6 for the formulation of the total, fluid and sediment,

density that is assumed to damp turbulence as if the fluid was stably stratified by salt or temperature.

In (4.17) and (4.18) P_k is the turbulence production term that is extended here by wave-turbulence interaction according to (4.16).

κ	0.41
σ_p	0.7
σ_k	1.0
σ_ε	1.3
c_μ	0.09
c'_μ	0.54
c_D	0.156
$c_{1\varepsilon}$	1.44
$c_{2\varepsilon}$	1.92
$c_{3\varepsilon}$	$0 \text{ } N^2 > 0$
$c_{3\varepsilon}$	$1 \text{ } N^2 < 0$
z_a	1 [mm]

Table 4.2. Coefficients used in the k-L and k- ε turbulence models.

In (4.19), κ is the Von Kármán constant ($\kappa \approx 0.41$), z_0 the roughness length, similar to the one used in bed friction (3.45), and z_a is some off-set or surface-roughness length scale that Groeneweg and Klopman (1998) introduced for maintaining a non-zero L at the free surface; they took $z_a = 1$ mm. In (4.19), $z=0$ is considered to be the mean bed level and $z=\bar{\zeta}$ the mean level of the water surface. The coefficients $\sigma_k=1.0$, $c'_\mu = 0.54$ and $c_D = 0.156$ are adopted from (Groeneweg and Klopman, 1998) but the addition of kinematic viscosity in (4.17) for diffusion is not applied by them.

Presently in the POINT SAND model, vertical advection by the mean and orbital flow is neglected but may be implemented in the same conservative approach as for sediment, see Chapter 6. Equation (4.17) is discretized on the same grid as for the momentum and pressure equations but with k and v_T on cell interfaces. At the bed and mean water surface (without wind forcing) the vertical diffusion of turbulent kinetic energy is zero. On the bed a usual boundary condition for high-Reynolds turbulence models is imposed, see Appendix C, with reference to velocity defined in the centre of the bed cell (k_{max}) at the previous time step.

For the mean velocity, the time reference is the start time of the inner loop of solving orbital motions. The boundary condition for k differs from the one imposed in (Groeneweg and Klopman, 1998) because they applied a no-slip condition for velocity and expressed u_* in the vertical gradient of horizontal velocity. The application by Groeneweg and Klopman (1998) of the no-slip boundary condition is not in accordance with the high-Reynolds turbulence model (4.17). The no-slip condition should be applied with a low-Reynolds turbulence model that accounts for the direct damping of turbulence by molecular viscosity.

Another problem of using the no-slip condition as well as low-Reynolds turbulence model for flows near hydraulically-rough bed is the existence of a viscous sublayer with typical thickness a few times larger than the size of the sand grains that form the bed roughness. The neglect of the viscous effects very close to the bed is in accordance with the following procedure. The application of the high-Reynolds turbulence closures, such as (4.17), can be regarded from the viewpoint of asymptotic expansion theory with

$$z^+ = \frac{u_* z}{\nu} \quad (4.21)$$

as scaling parameter. Note that z^+ is a local Reynolds number. The inner solution holds for small z^+ and covers the z -interval with dominant viscous effects on turbulence. Conversely, the outer solution is dedicated to large z^+ and this is the range of application of high-Reynolds turbulence models. In this asymptotic expansion, the outer solution should match the inner solution and, as usual in this theory, the matching conditions for the outer solution are imposed on $z^+=0$. Appendix C gives the matching conditions for the (high-Reynolds) outer solution, see e.g. (Van Dyke, 1975, eq. 7.7b).

The diffusion term in the turbulence equation (4.17) Euler-implicit time integrated, P_k is integrated explicit and in the last so-called energy-dissipation term, $k^{3/2}$ is written as a product of old and new time level and it is integrated implicitly. This numerical solution ensures positive k and consequently no truncation on k is applied. The k -L model is solved at each inner-loop time step using the solution of the orbital motions at the new inner-loop time level. All components entering the double contraction $\tilde{d}_{ij}\tilde{d}_{ij}$ in (4.16) of the wave-related strain-rate tensor are evaluated but the horizontal gradients are derived from temporal derivatives, according to (2.4).

5 The mean velocity profile and mean flow rate

After completion of simulating the orbital motions and turbulence properties in the inner loop, the momentum equation (2.1)

$$\frac{\partial U}{\partial t} + \frac{\partial P}{\partial x} = \frac{\partial}{\partial z} \left\{ (v + v_T) \frac{\partial U}{\partial z} \right\} + T_x$$

for the mean horizontal velocity is solved with a time step equal to the wave period. The solution procedure is the one employed in the original DPM with WCI force T_x integrated explicitly. The eddy-viscosity in (2.1) equals the eddy viscosity obtained by solving the q^2 -L turbulence model (Section 4.2) up to the last time step in the inner loop. The boundary condition on the mean water surface equals (3.20) which is derived from time-averaging the stress-free condition with surface waves. The standard boundary condition on the bed is due to a logarithmic profile using the roughness length scale z_0 user prescribed either directly or converted from user-specified Chézy or Manning coefficient

The standard procedure in the POINT SAND model is adopted for estimating the horizontal pressure gradient such that the depth-averaged horizontal velocity U_0 is obtained and U_0 is user-prescribed. In the experiments (Klopman, 1994), the total flow rate in the facility is constant and it is determined by a pump recirculating the water in the flume so that U_0 then represents the flow rate averaged, over any cross section of the flume between the flow-inlet and flow-exit sections. In case of waves in the facility, the depth-integrated Stokes drift yields an additional flux in the direction of wave propagation.

In the numerical simulations using the extended DPM, the following three fluxes are involved in obtaining the imposed depth-averaged velocity U_0 :

- The depth average of $U(z)$ being the solution of (2.1);
- The depth average of Stokes drift $U_S(z)$;
- The depth average of $\bar{\tilde{u}}(z)$, being $\tilde{u}(z,t)$ averaged over the previous wave period.

At the end of Section 3.3, the role of force T_x is explained in conjunction with the addition of the horizontal orbital momentum equation (3.22) to the mean (wave-averaged) horizontal momentum equation (2.1). Conceptually, the essential point is the elimination of T_x in conjunction with a non-zero wave-averaged horizontal orbital velocity $\bar{\tilde{u}}(z)$, defined by (3.27). The total mean velocity then reads $U(z) + \bar{\tilde{u}}(z)$ rather than just $U(z)$.

For WCI, the procedure for adjusting the horizontal pressure gradient is extended by including the wave-related mass flux, or equivalently depth-integrated Stokes drift, and the new formulation reads as follows:

$$\frac{\partial P}{\partial x} = \frac{\tau_{s,x} - \tau_{b,x}}{\bar{\zeta}} + \frac{U^{(\zeta)} + U_S^{(\zeta)} - U_0}{T_{rx}} + \bar{T}_x \quad , \quad (5.1)$$

with depth-averaged velocity and depth-averaged Stokes drift defined by

$$U^{(\zeta)} = \frac{1}{\bar{\zeta}} \int_0^{\bar{\zeta}} U(z,t) dz \quad ; \quad \bar{\zeta} U_S^{(\zeta)} = \overline{\tilde{\zeta} \tilde{u}(\tilde{\zeta})} + \frac{1}{2} \overline{\tilde{\zeta}^2} \left. \frac{\partial U}{\partial z} \right|_{\tilde{\zeta}} \quad , \quad (5.2)$$

for the latter see (Van Kester et al, 1996). Likewise, the depth-average of $T_x(z)$ is defined by

$$\bar{T}_x = \frac{1}{\bar{\zeta}} \int_0^{\bar{\zeta}} T_x(z) dz \quad . \quad (5.3)$$

In (5.1), $\tau_{b,x}$ is the bed shear stress and $\tau_{s,x}$ the surface shear stress, both divided by fluid density. The shear stress $\tau_{s,x}$ is used here for imposing the condition (3.20) for a stress-free boundary with waves. In (5.1), T_{rx} is a relaxation time which is set to twice the time step of solving (2.1) i.e. twice the wave period and this choice is standard for the original DPM. The RHS of the depth-integrated Stokes drift in (5.2) is due to averaging over the inner-loop solutions of the last wave period. Similarly, force T_x defined by (3.27), is evaluated over the inner-loop solutions in the previous wave period.

The solution of the mean flow profile according to (2.1) is used in the next inner loop for solving the hydrodynamic pressure, vertical and horizontal orbital velocity and k-L turbulence model in the inner loop. This closes the set of equations.

6 Sediment distribution model

6.1 Advection-diffusion equation

We apply the following advection-diffusion equation for the mass concentration $c^{(k)}$ of sediment fraction ($k=1,2,\dots$):

$$\frac{\partial c^{(k)}}{\partial t} + \nabla \cdot (\underline{u}_c^{(k)} c^{(k)}) = \frac{\partial}{\partial z} \left[\left(\nu + \frac{\nu_T}{\sigma_T^{(k)}} \right) \frac{\partial c^{(k)}}{\partial z} \right], \quad (6.1)$$

using the mean particle velocity

$$\underline{u}_c^{(k)} = \underline{\tilde{u}} + w_s^{(k)} \frac{\underline{g}}{g}. \quad (6.2)$$

The particle velocity (6.2) is averaged over a sufficiently small volume still containing a sufficiently large number of particles for defining this mean velocity vector. The first term in the RHS of (6.3) represents the orbital velocity of all spectral components. The last term in (6.2) is the fall velocity, specified below for sand and g is the downward acceleration vector with magnitude g .

The horizontal orbital velocity component in (6.2) is the solution of the horizontal momentum equation (3.30). The vertical orbital velocity component, however, is derived from the incompressibility condition rather than from its momentum equation. This inconsistency is motivated by mass conservation and this argument is clarified in Section 6.3.

By (6.2) we implicitly assume that the mean flow is horizontal and that it does not vary in horizontal direction. The orbital velocity consists of the horizontal as well as vertical orbital component. In (6.1) just the vertical diffusion is included. In (6.1), the eddy diffusivity is defined through the eddy viscosity ν_T divided by σ_T , the turbulence Prandtl/Schmidt number. Typically, $\sigma_T \approx 0.7$ holds and this corresponds to the multiplication factor $\beta \approx 1.4$ used in sand transport literature. The Prandtl/Schmidt number is a user-defined parameter and can be specified per sediment fraction (k).

Implicitly, we assumed in (6.1) that the particle response time (Stokes time) is sufficiently small so that all temporal and spatial variations in eddy diffusivity are transferred to particle diffusion. In other words, in (6.1) we do not apply the high-pass filter function that was introduced in Chapter 4 for the possibly reduced response of turbulent eddies to the straining action of the orbital motions.

Appendix D describes that the user can select more than one sediment fraction e.g. with different grain diameter and mass density. For simplicity in notation in the remaining text, however, we omit the superscript (k) for sediment fraction unless required.

The fall velocity of the sediment w_s is computed according to Van Rijn (1993) but reduced by hindered settling (see Eqs 8.2 and 8.3 in Bosboom et al., 1997, Unibest-TC manual). The fall velocity $w_{s,0}$ of a single particle in infinite fluid, without wall effects, reads (Van Rijn, 1983):

$$\begin{aligned} w_{s,0} &= \frac{\Delta g d_s^2}{18\nu} & , & \quad 1\mu\text{m} < d_s \leq 100\mu\text{m} \\ w_{s,0} &= \frac{10\nu}{d_s} \left[\left(1 + \frac{0.01\Delta g d_s^3}{\nu^2} \right)^{1/2} - 1 \right] & , & \quad 100\mu\text{m} < d_s \leq 1000\mu\text{m} \\ w_{s,0} &= 1.1(\Delta g d_s)^{1/2} & , & \quad 1000\mu\text{m} < d_s \end{aligned} \quad (6.4)$$

Here d_s is the diameter of the suspended sediment, which is a user-defined property. Van Rijn (1987) concluded, on the basis of measurements, that d_s should be in the range of 60 to 100% of the diameter of the median bed material size d_{50} . In the current version of the POINT SAND model, d_s is set equal to d_{50} . A user-defined d_s will be implemented in a later stage. It appears that through the piecewise approximations (6.4), the settling velocity is a discontinuous function of the grain size. Although during the simulation the grain size is constant, this discontinuity is an undesired property and we recommend replacing (6.4) by a smooth function of d_s over the entire range.

In high concentration mixtures, the fall velocity of a single particle is reduced by the flow as well as fluid stresses induced by other particles. Following Richardson & Zaki (1954) we use:

$$w_s = \left(1 - \frac{\phi}{\phi_s} \right)^5 w_{s,0} \quad (6.5)$$

with $w_{s,0}$ defined by (6.4) and where ϕ is the volume fraction of the all suspended sediment i.e.

$$\phi = \sum_k \frac{c^{(k)}}{\rho_s^{(k)}} \quad (6.6)$$

Further, $\phi_s = 0.65$ is taken as the maximum volume fraction of solids in a non-cohesive porous bed. Through (6.6) the volume fraction becomes a temporarily and spatially varying property. The Richardson & Zaki formulation (6.5) then makes the settling velocity time and space varying.

6.2 Boundary conditions

Equation (6.1) is subjected to the boundary conditions of zero flux at the mean water surface and a specified time-dependent boundary condition at a reference level close to the bottom. Presently, the user can choose between the following two generic forms for the boundary condition based on reference concentration.

The first boundary condition prescribes the sediment concentration at a certain reference level z_a :

$$c(z_a, t) = c_b(t) \quad , \quad (6.7)$$

or reformulated in terms of a pick-up function:

$$w_s c_b(t) + (v + v_T / \sigma_T) \frac{\partial c}{\partial z} \Big|_{z=z_a} = 0 \quad . \quad (6.8)$$

The reference level z_a must correspond to the prescription of the bed-reference concentration c_b . Presently, we implemented the formulation of Zyserman and Fredsøe (1994) for the mass concentration $c_b(t)$:

$$c_b(t) = \frac{0.331(\theta - \theta_c)^{1.75}}{1 + \frac{0.331}{C_m}(\theta - \theta_c)^{1.75}} \quad \text{at} \quad z_a = 2d_{50} \quad . \quad (6.9)$$

In (6.9), the maximum concentration C_m has a value of 0.32 that deviates from the original value in (Zyserman & Fredsøe, 1994). Further, in (6.9), θ is the Shields parameter defined by

$$\theta = \frac{u_{*b}^2}{(s-1)g d_{50}} \quad ; \quad s = \frac{\rho_s}{\rho_w} \quad , \quad (6.10)$$

with s the relative sediment density and u_* the total instantaneous shear velocity

$$u_{*b}^2 = f_{hp} v_T \frac{\partial u}{\partial z} \Big|_{z=0} \quad (6.11)$$

as determined by the hydrodynamic module. Note that $f_{hp} = 1$ holds at the bed because of the small and rapid turbulent eddies. The computation of the bed-shear velocity (6.11) is treated in detail in Appendix C.

Finally, in (6.9), θ_c is the critical Shields parameter and Van Rijn (1993) proposes the following piecewise representation of the Shields curve:

$$\begin{aligned}
\theta_c &= 0.24 D_*^{-1} & , & & 1 < D_* \leq 4 \\
\theta_c &= 0.14 D_*^{-0.64} & , & & 4 < D_* \leq 10 \\
\theta_c &= 0.04 D_*^{-0.1} & , & & 10 < D_* \leq 20 \\
\theta_c &= 0.013 D_*^{0.29} & , & & 20 < D_* \leq 150 \\
\theta_c &= 0.055 & , & & 150 < D_*
\end{aligned} \tag{6.12}$$

with the dimensionless grain diameter D_* :

$$D_* = d_{50} \left(\frac{(s-1)g}{\nu^2} \right)^{1/5} . \tag{6.13}$$

It appears that through the piecewise approximations (6.12), the critical Shields parameter is a discontinuous function in D_* which is an undesirable property that we recommend for improvements.

Upward mixing of suspended sediment involves the conversion of Turbulent Kinetic Energy of the fluid into an increasing potential energy of the sediment. The latter is subsequently destroyed by viscous drag while the particles settle. The rate of conversion of TKE into the sediment's potential energy is called buoyancy flux. The latter is included in the implemented k-L and k- ϵ turbulence models by assuming the analogy between sediment-laden flows and flows with density stratification through temperature or salt. Accordingly, the buoyancy flux for the sediment is then estimated by the total fluid-sediment density ρ defined as:

$$\rho = \rho_w + \sum_k \left(1 - \frac{\rho_w}{\rho_s^{(k)}} \right) c^{(k)} \tag{6.14}$$

In (6.14), ρ_w represents the density of pure water and this density is determined by its temperature and salinity, the latter are specified by the user.

Note that at the instant of zero bed stress in an oscillatory flow (6.8) may yield a positive concentration $c(z_a)$ whereas (6.7) prescribes a zero concentration.

6.3 Mass conservation and inconsistency with dynamical equations for orbital motions

The horizontal advection by orbital motions in (6.1) needs careful attention for satisfying the conservation of sediment mass in an incompressible fluid and this subject is considered here.

We start with (6.1) for a constant sediment mass concentration, whence:

$$\frac{\partial \tilde{u}}{\partial x} + \frac{\partial \tilde{v}}{\partial y} + \frac{\partial \tilde{w}}{\partial z} = 0 \quad (6.15)$$

This well-known requirement is not guaranteed by the solution of the vertical momentum equation (3.21) even though the hydrodynamic pressure solution was formulated using (6.15) in conjunction with the linearized momentum equations, see Section 3.1. Moreover, the free-surface conditions for the momentum equations are prescribed at the (time-averaged) mean-water level rather than at the momentary water level $z=\zeta(t)$.

For correctly modelling horizontal and vertical sediment transport, the incompressibility condition (6.15) and its intimate relation to the advection-diffusion equation (6.1) is essential. Consequently, for satisfying mass conservation we derive the vertical orbital velocity for sediment transport from (6.15) rather than from the vertical momentum equation. This is the inconsistency announced in the title of this section.

We define \tilde{w}_c as the vertical orbital velocity component that satisfies (6.15) formulated now as follows:

$$\frac{\partial \tilde{w}_c}{\partial z} + \sum_n \frac{\partial \tilde{u}(x, y, z, t; \omega_n)}{\partial x} + \frac{\partial \tilde{v}(x, y, z, t; \omega_n)}{\partial y} = 0 \quad (6.16)$$

with summation over all spectral components ($n=1,2,3\dots$) related to the user-specified angular frequencies ω_n . The horizontal derivatives in (6.16) are converted to time derivatives through two steps that were introduced with reference to (3.28) and to Appendix B. The latter demonstrates that, by excellent approximation, the orbital velocity vector is in the vertical plane containing the wave number $\underline{k}(\omega_n)$. The latter simplifies (6.16) to

$$\frac{\partial \tilde{w}_c}{\partial z} + \sum_n \frac{\partial \tilde{u}(z, t; \omega_n)}{\partial x_k} = 0 \quad , \quad (6.17)$$

with x_k the horizontal co-ordinate parallel to $\underline{k}(\omega_n)$. Subsequently, we adopted in Section 2.3 the periodicity assumption which converts (6.17) into

$$\frac{\partial \tilde{w}_c}{\partial z} = \sum_n \frac{k(\omega_n)}{\omega_n} \frac{\partial \tilde{u}(z, t; \omega_n)}{\partial t} \quad , \quad (6.18)$$

Integrating (6.18) from the bed level $z=0$ upwards yields the vertical orbital velocity component in accordance with the incompressibility condition:

$$\tilde{w}_c(z, t) = \sum_n \frac{k(\omega_n)}{\omega_n} \int_{z'=0}^z \frac{\partial \tilde{u}(z', t; \omega_n)}{\partial t} dz' \quad . \quad (6.19)$$

The vertical orbital velocity, as defined by (6.19), is used in the advection term of (6.1) and the latter reads now:

$$\frac{\partial c^{(k)}}{\partial t} + \nabla \cdot (\mathbf{u}_c^{(k)} c^{(k)}) = \frac{\partial}{\partial t} \{ (1 - \tilde{u}_a) c^{(k)} \} + \frac{\partial}{\partial z} \{ (\tilde{w}_c - w_s^{(k)}) c^{(k)} \} \quad (6.20)$$

with the dimensionless velocity \tilde{u}_a defined by the summation over all spectral components ($n=1,2,3,\dots$):

$$\tilde{u}_a = \sum_n \frac{k(\omega_n)}{\omega_n} \tilde{u}(z, t; \omega_n) \quad (6.21)$$

being the sum of the ratio between horizontal orbital velocity and celerity per spectral component.

Finally, all equations are solved up to the mean-water level $z = \bar{\zeta}$ and to ensure depth-integrated mass conservation we must impose the zero flux condition at the mean-water level i.e.

$$z = \bar{\zeta}: \quad \tilde{w}_c - w_s^{(k)} = 0 \quad . \quad (6.22)$$

If the sediment concentration is not zero near the mean water level and if the net vertical velocity is upward than (6.22) creates a blocking of vertical sediment transport and consequently an increase of sediment concentration in the top layer. The latter increase is not realistic, but it is our sacrifice to obey strict mass conservation. However, all sand transport remains in a comparatively thin wave-affected boundary layer so that the artificial blocking imposed by (6.22) is not observed in practice.

The next section presents the numerical implementation that ensures mass conservation.

6.4 Numerical implementation

The advection-diffusion equation (6.1) is discretized in a finite volume and mass conservative formulation. Notice that this equation is solved once in the *inner-time loop* after the solution of all spectral orbital components.

The vertical grid for sediment transport equals the grid for the numerical solution of the hydrodynamic and turbulence equations.

The horizontal mean and orbital velocity component as well as the mass concentration $c(z,t)$ are defined in the centres of the grid boxes. The total vertical velocity component $\tilde{w}_c - w_s^{(k)}$, which includes the fall velocity $w_s^{(k)}$, as well as the turbulence fluxes are defined on the cell interfaces. The numerical integration (6.19) is based on the same spatial discretisation as for the advection diffusion equation and this discretisation guarantees mass conservation at the numerical representation.

The ceiling of the upper grid box corresponds to the mean water level. The definition of the lowest grid box depends on the selected boundary condition (6.7) or (6.8) and this definition is explained below.

For (6.7), the lowest computational grid box is defined as the box with its centre nearest to the level $z=z_a$ as defined by (6.9). For the pick-up formation (6.8), however, the lowest grid box has its bottom nearest to the level $z=z_a$ as defined by (6.9). In the code, the integer pointer to the lowest grid box is defined as KBED and, of course, $KBED \leq KMAX$ holds where KMAX is the user-specified number of grid boxes of the hydrodynamic and turbulence-model equations. Note that KBED depends on the grain diameter and KBED may thus vary between sediment fractions.

For extremely fine grids near the bed, it is possible that some grid boxes are excluded. Nevertheless, information on mass concentration must be known for the computation of:

- the horizontal sediment transport; and for
- the buoyancy flux using the total density defined by (6.14).

For these purposes we assume that

$$z \leq z_a: c(z, t) = c(z_a, t) \quad (6.23)$$

holds. Consequently, the advection diffusion equation (6.1) is thus solved for the grid boxes $1 \leq k \leq KBED$.

The vertical diffusion in (6.1) is formulated by the θ method although we recommend $\theta=1$ i.e. Euler-implicit for avoiding wiggles. The diffusive flux at the upper interface of cell number k is based on the finite difference of c_{k-1} (one cell up) and the sediment concentration c_k of this cell. The eddy viscosity ν_T is defined at the cell interface. The diffusive flux is zero at the mean-water level and guarantees mass conservation in conjunction with (6.22).

The vertical advection in (6.20) reads

$$\frac{\partial}{\partial z} \left\{ (\tilde{w}_c - w_s^{(k)}) c^{(k)} \right\} \quad (6.24)$$

and there are numerous ways for its discretisation. We implemented the following implicit advection schemes:

- first-order upwind;
- second-order central scheme;
- third-order ADI upwind-central scheme.

For the user we made just the first-order up wind scheme available. This scheme is the single advection scheme that guarantees monotonicity i.e. positive sediment concentration and no internal formation of new maxima or wiggles. The disadvantage is that the first-order upwind scheme introduces numerical diffusion by the amount:

$$\frac{1}{2} |\tilde{w}_c - w_s^{(k)}| \Delta z \quad (6.25)$$

with local cell height Δz . On the one hand, for large vertical orbital motions this artificial diffusion can be significant. On the other hand, in the wave-affected boundary layer the net vertical velocity in (6.25) remains of the order of the fall velocity.

Numerical experiments with zero fall velocity show that the third-order ADI scheme is the best of the three and creates minor over- and undershoots at very sharp sediment concentration jumps. The latter hardly occur in practice and on sufficiently fine grids. The third-order ADI scheme is computational much more involved than the first-order scheme. Compared to the effort in solving all the other momentum equation for the orbital motions as well as turbulence equations in the *inner-time loop*, the increase in computational effort is modest.

Therefore we recommend the final implementation of the bed-boundary conditions for the third-order ADI scheme in case of accurate estimation of sand transport with orbital motions.

Of course, in case of wave tunnel experiments all orbital velocity components in the previous considerations are set to zero and there is just vertical advection by the fall velocity. The first-order upwind scheme may then be the optimal choice.

7 Tests case

7.1 Introduction

The tests reported in this chapter were selected for demonstrating the capability as well as flexibility of the same POINT-SAND model for simulation constant flows, oscillatory wave-tunnel experiments and free-surface wave-channel experiments.

In Section 7.2, the hydrodynamic as well as the sediment modules are compared to analytic solutions for stationary turbulent flows with logarithmic-velocity and Rouse-concentration profiles. Use is made of built-in routines described in Appendix E.

Section 7.3 presents tests for the full hydrodynamic module i.e. for surface waves on a mean flow with comparison to extensive series of flume experiments. These test demonstrate the model's capability of simulating the hydrodynamics in a free-surface wave channel.

In Section 7.4 the hydrodynamic and sediment modules of the POINT-SAND model are combined for simulating experiments in a wave tunnel with a rigid lid rather than a mobile water surface. In order to do so, the model was run in wave-tunnel mode, which means that the vertical orbital velocity component is not taken into account. It does however give information on the behaviour of the model compared to wave boundary layer models (see Davies et al, 1997) that neglect the vertical velocity component. The aim of the comparison with the wave-tunnel experiments is to test whether the new model is able to give results which are at least of the same quality as the results presented in (Davies et al., 1997).

Finally, we refer to our ICCE paper in Appendix F and G presenting tests and discussions on the importance of the novel features of the POINT-SAND model i.e. the simulation of sediment transport in wave-driven flows.

7.2 Built-in test case

In steady turbulent flows, the vertical profiles of velocity as well as concentration are *nearly singular* so that their simulation requires careful validation. To that purpose, Appendix E presents the analytic solution for the depth-integrated sand-flux, being the product of a logarithmic velocity profile and the Rouse profile for suspended sand concentration. Both profiles are consistent with a parabolic profile for eddy viscosity. When the user runs the model with the extension *log* for the standard input file, the influence of sediment load on buoyancy is switched off and a subroutine adds the analytic solutions to another output file, for details see Appendix E.

Figure 2^{a+b} presents the graphs using directly the output data that is scaled when running the model with the built-in test case option for steady flows. The flow velocity is 1 m/s in 1 m deep water over a bed with $d_{50}=150 \mu\text{m}$ sand and with roughness $z_0=5d_{50}$. The non-diffusive second-order central advection scheme is used for simulating the settling of sand.

The bed concentration is prescribed at $2d_{50}$ in the centre of the computational bed boundary layer which thus has a thickness of just $4d_{50}=0.6$ mm i.e. roughly equal to z_0 .

The implemented option of using exponentially-increasing layer thickness is demonstrated here with just 50 layers for covering the 1000 mm water depth while starting with the 0.6 mm bed boundary layer. The time step is 1 s and 1000 steps are made and convergence is checked by 5000 steps.

Figure 2 presents a good comparison, using the k-L turbulence model. Notice that the particular definition of length scale $L(z)$, see (4.19), makes the eddy viscosity profile of the k-L turbulence model very close to a parabolic profile for which the analytic solutions of Appendix E were derived. The simulation with the k-L model yields a depth-integrated sand flux of $5.13 \text{ kg}\cdot\text{m}^{-1}\cdot\text{s}$ which is very close to the theoretical solution of $5.14 \text{ kg}\cdot\text{m}^{-1}\cdot\text{s}$.

Figure 3 shows a lesser comparison between the analytic solutions and the simulation based on the k- ϵ turbulence model with all other numerical settings equal to those of Figure 2. The difference begins with the eddy-viscosity profile estimated by the k- ϵ turbulence model deviating from the theoretical parabolic profile. These deviations gradually accumulate into the depth-integrated sand flux of $3.06 \text{ kg}\cdot\text{m}^{-1}\cdot\text{s}$ simulated by the k- ϵ model rather than the $5.14 \text{ kg}\cdot\text{m}^{-1}\cdot\text{s}$ of the theoretical solution.

Figure 4 exhibits, with all other numerical conditions the same, the performance of Davies' k-L model where L is based on a depth-integral of the turbulent kinetic energy k . The depth-integrated sand flux simulated by Davies' k-L model is $7.68 \text{ kg}\cdot\text{m}^{-1}\cdot\text{s}$ large compared to the analytic solution of $4.06 \text{ kg}\cdot\text{m}^{-1}\cdot\text{s}$ rather than the previously found (Figures 1 and 2) $5.14 \text{ kg}\cdot\text{m}^{-1}\cdot\text{s}$ theoretical solution.

The last deviation between theoretical results is unexpected but it is entirely due to a change of the Von Kármán constant $\kappa=0.41$ for implementation of the k-L and k- ϵ turbulence models whereas Davies' k-L model applies $\kappa=0.40$ which is used in the POINT-SAND model only when his model is selected. The large change in the theoretical result by such a minor change in the Von Kármán constant demonstrates the tremendous sensitivity of the theoretical depth-integrated sand flux to input as well as state parameters, see also Table E.2 in Appendix E.

Figure 5 is a repetition of Figure 2 i.e. using the k-L model but now the advection scheme is changed from the non-diffusive second-order central scheme to the diffusive first-order upwind scheme for advection by the settling velocity. By doing so, the estimated depth-integral of the sand flux increased from $5.13 \text{ kg}\cdot\text{m}^{-1}\cdot\text{s}$ to $6.76 \text{ kg}\cdot\text{m}^{-1}\cdot\text{s}$ due to the numerical diffusion. This is a large difference, although the concentration profiles (on log-log plots) in Figure 4^b show a minor overestimation.

After this demonstration of the implemented test case options, we conclude as follows. The built-in test case option with its comparison to theoretical results, appears to be instructive for the beginning as well as the experienced user in appreciating the sensitivity of numerically simulating sand transport to very fine scales.

Minor deviations in eddy viscosity amount to larger deviations in the logarithmic velocity profile, the bed shear stress and the Rouse-concentration profile so that finally the depth-integral of sand flux is the essential but unfortunately very sensitive outcome.

Further, we hope that the reader is not drawing the seemingly obvious conclusion that the k-L model is superior to the k- ϵ or Davies' k-L turbulence model. The good comparison between theory and the k-L model is due to the definition (4.19) of its mixing length L that nicely matches the parabolic eddy viscosity used in the theory. Note that there exist no fluid-mechanics law yielding a parabolic eddy viscosity as well as a parabolic eddy diffusivity profile, for more comments see Appendix E.

Nevertheless, we recommend using the k-L model when running the built-in test case simply because it can match the theoretical results so that the user can record easily the deviation introduced by varying numerical and state parameters, as we demonstrated briefly.

In the following section, the hydrodynamics of the POINT-SAND model are tested for simulation wave-current interactions where the simulated second-order wave phenomena depend on temporal or phase lags, either physically or numerically introduced.

7.3 Wave-current interaction; the Scheldt flume

This section presents a series of test cases for the wave-dynamics part of the POINT SAND model. All cases are based on observations made by Klopman (1994) in the Scheldt flume of WL|Delft Hydraulics. The comparison is limited to mean flow and orbital amplitude properties only. We recommend processing the available data for comparison in terms of turbulence properties as well as Stokes drift.

Klopman performed tests with monochromatic, bi-chromatic and random waves without current, following the current and opposing the current. Also a test series was performed for a steady current without waves. It was found that the mean horizontal current profile under combined wave-current motion is strongly affected by the presence of waves, not only inside but also outside the wave bottom boundary layer. In the upper half of the water column the velocity shear is reduced and may even change sign in the case of waves following the current. Waves opposing the current increase the velocity shear in the upper half of the water column.

Following Radder's proposition that he based on arguments derived from the Craik-Leibovich (CL) vortex force, additional observations were made in a cross section under the same wave and flow conditions and in the same facility. These observations revealed the secondary circulation in vertical cross sections perpendicular to the current as Radder anticipated, for more background see Section 2.2 as well as (Dingemans et al., 1996).

In qualitative agreement with observations, numerical simulations (Dingemans et al., 1996) for waves following the current show that the wave-driven secondary circulation contributes to the backward bending of the vertical profile of the horizontal current. This backward bending is due to the transfer of low momentum fluid from the upper part of the vertical walls to the upper part of the flow in the flume's centre plane.

This phenomenon, driven by CL vortex force, cannot be simulated explicitly by the POINT SAND model. Instead, we recommend the implementation of Radder's model (Dingemans, 1999) representing the net effects of the CL vortex force in terms of additional momentum transfer.

Figures 6 to 9 compare the observations in (Klopman, 1994) with the wave-current simulation using the POINT-SAND model but without an additional model for the net effect of the CL vortex force.

Figure 6 presents what appeared to be the most delicate test case for wave-current interaction by the POINT-SAND model. It is a test that in principle lies outside the intended range of applicability of the POINT-SAND model as it is designed for waves on turbulent shear flows rather than on laminar flows.

In Figure 6, the monochromatic wave propagates in positive U-direction on initially stagnant water while producing virtually no turbulence above a thin bed-boundary layer. In other words, most of the water column is a weak laminar flow. Particularly, the very weak streaming in the surface boundary layer relies now on the laminar flow solution of the model. Moreover, the crude zero-order approximations (3.19) and (3.2) for the stress-free water surface dominate in this test case.

The simulation for Figure 6 required careful selection of the time step as well as the relaxation time for temporarily smoothing, per computational layer, the otherwise oscillating WCI force. If the WCI force oscillates in time then also spatial oscillations along the water depth may be induced due to subtle phase differences of the temporal oscillations of the WCI force as a function of the depth co-ordinate. These vertical oscillations are virtually not damped because of the laminar flow. Nevertheless, the result is in qualitative agreement with observations and that is more than we anticipated of the model for laminar flow. Figures 2 and 3 of Appendix G exhibit additional evidence for this test case.

Note that in Figure 6 the monochromatic wave propagates in positive U-direction and visual inspection suggests that the depth-integrated flow is in negative U-direction. However, there is also the Stokes drift for the water-mass flux that we do not simulate explicitly. Instead, the user-specified depth-averaged velocity (zero here) is corrected by the Stokes drift through the pressure-gradient control procedure (5.1). Consequently, the depth-integral of the velocity profile in Figure 6 is compensated by the depth-integrated Stokes drift.

Figure 7 is devoted to the proper design conditions of the POINT SAND model i.e. waves propagating on a turbulent shear flow. The results in terms of mean flow and amplitude of the 1.44 s carrier wave are in good agreement with the observations. We cannot explain the underestimation of the wave amplitude (Figure 7^b) for a monochromatic wave against the current. Further investigation, including a check on the processing of the wave amplitude and the occurrence of wave reflection is recommended.

Figure 8 deals with bichromatic waves propagating with the turbulent current. This is the first test case where more than one spectral component is simulated by the POINT SAND model. The results are in good agreement with observations although the backward curvature in the mean current profile begins at higher levels than observed.

Figure 9 is a challenging simulation using 12 spectral components that Klopman constructed from his wave spectrum that was forced by significantly more spectral components. The 12 spectral components have nearly the same wave amplitude. Due to lacking digital data sets we did not compare the rms wave amplitude to observations but this is recommended for future analysis.

In addition to the previous cases, Figure 5 in Appendix F presents an example of simulating a second-order Stokes wave in a 3.4m wave channel with similar horizontal orbital velocity as for the C1 series in the rigid-lid wave tunnel. Figure 5 in Appendix F shows the deformation of the second-order Stokes wave inside the wave-boundary layer. Further, this figure exhibits a remarkable feature of local maximums in the eddy viscosity just after flow reversal. For more details we refer to the text of Appendix F describing that the high-pass filter function f_{hp} (Section 4.1) is responsible for these local maximums in eddy viscosity. Although local maximums in turbulence after flow reversal can occur due to turbulence to laminar and laminar-turbulence transitions, these phenomena are not intentionally modelled by f_{hp} nor by the implemented high-Reynolds $k-\epsilon$ turbulence model.

Note that the filter function can be applied only for orbital motions because each spectral component is simulated separately so that f_{hp} weights the strain rates per spectral component and as a function its wave period, see (4.12). In principle, the high-pass filter function is not designed for simulating wave tunnel experiments because then just the sum of all spectral components is simulated so that f_{hp} is not appropriately applicable.

We conclude that the wave-current interaction part of the POINT-SAND model is indeed capable of simulating complicated wave-current test cases also with multiple spectral components. we recommend the implementation of the model (Dingemans, 1999) for the net effect of the CL vortex force on momentum and mass transfer. It is anticipated that for the cases of waves following the current, the vertical profiles of the mean current would bend more backwards than shown in Figures 7, 8 and 9.

An experienced user is required for simulating wave-current interaction cases. The reason is that temporal and sometimes spatial oscillations in the WCI force occur. These oscillations disappear at some outer-loop time step as well as relaxation time, the latter smoothes the temporal behaviour of the WCI force. Unfortunately there is not yet a reliable rule-of-the-thumb for choosing these numerical parameters. Presently, the best advice we can give is setting the outer-loop time step equal to the period of the lowest subharmonic of the carrier waves and taking the relaxation time two times longer. Further, we found that with more spectral components the oscillations in the WCI vanish probably because of a lacking dominant subharmonics.

7.4 Sand transport; the wave tunnel

7.4.1 Test cases

Model results regarding the sediment concentration are discussed for 2 oscillating wave tunnel experiments:

1. Case C1: this is a case with asymmetrical waves. The following wave conditions were applied at a level of $z = 0.20$ m from the bed: $U(z = 0.2 \text{ m}) = U_0 + U_1 \cos \omega t + U_2 \cos 2\omega t$, where $T = 2\pi/\omega = 6.5$ s and $U_0 = 0.025$ m/s; $U_1 = 0.845$ m/s and $U_2 = 0.265$ m/s. The d_{50} of the applied sediment was 210 μm . This case is comprehensively described in Al-Salem (1993).
2. Case E1: this is a case with sinusoidal waves. The following wave conditions were applied at a level of $z = 0.075$ m from the bed: $U(z = 0.075 \text{ m}) = U_0 + U_1 \cos \omega t$, where $T = 2\pi/\omega = 7.2$ s and $U_0 = 0.15$ m/s and $U_1 = 1.60$ m/s. The d_{50} of the applied sediment was 210 μm . This case is comprehensively described in Katopodi *et al.* (1994).

7.4.2 Input/output

The input files used for the calculations are INDPM.C1, TUN_C1.LVL, TUN_C1.VEL and WAVSPC.C1 for the C1-case and INDPM.E1, TUN_E1.LVL, TUN_E1.VEL and WAVSPC.E1 for the E1 case. These files can be found on the accompanying diskette. The input files are listed and discussed in Appendix D. The file INDPM.* is the main input file where parameters can be set regarding the grid schematisation, turbulence model, bed roughness and sediment properties, amongst others. In the file *.VEL the wave conditions are specified, whereas in the file *.LVL the water levels (this is a dummy file for the wave tunnel conditions). In WAVESPC.* the frequencies for harmonic analysis are specified. Note that the velocities specified are depth-averaged velocities. If the user wishes to set the velocity at a certain level, the depth-averaged velocity should be chosen such that the required velocity at the required level is realised. In a future version of the program, it will be possible to apply the velocity at a user-defined level.

The output files generated by the computer program are: OUTDPM.C1 and OUTSPC.C1 for the C1-case and OUTDPM.E1 and OUTSPC.E1 for the E1-case. The output file OUTDPM.* consists of the following items: first a copy of the input, subsequently the output at each time step specified. A description of the output files can be found in Appendix D.

Results of the harmonic analysis can be found in the file OUTSPC.*. All input files for the two cases discussed are stored on the accompanying diskette. Also the executable of the 1DV-program is stored there. The output files are not stored on the diskette due to limited disk space, but may easily be generated running the executable using the input files. Answer 'c1' or 'e1' to the question 'Give filename extension for files indpm and outdpm:'. If the program aborts abnormally, an error diagnosis message is written to the file OUTSPC.*.

7.4.3 Results

In Fig. 10 the time-averaged concentration profile is plotted for case E1. Comparison with measurements shows that the calculated concentration profile closely matches the measured one near the bed and at a level of a few centimetres above the bed. At intermediate heights the calculated concentration is too high. This is also the case for the upper part of the water column. The observed curvature of the concentration profile near the bed, which separates two distinct regions, may be attributed to turbulent kinetic energy damping by vertical gradients in suspended sediment concentration. This has to be further examined.

Sediment concentrations as a function of time at several levels for case E1 are plotted in Fig. 11. Moreover, for two levels ($z=2.3$ and $z=3.7$ cm, Figs. 12 and 13) calculated profiles are compared with measured profiles. The calculated concentration at $z=2.3$ cm is much too high, whereas the concentration at $z=3.7$ is about right. Calculated and measured peaks during a wave cycle roughly coincide.

For case C1 (second-order Stokes wave) the calculated sediment concentration behaves approximately the same. In Fig. 14 the time-averaged concentration profile is plotted for case C1. Comparison with measurements again shows that the calculated concentration profile matches the measured one at a level of a few centimetres above the bed. In the lower and higher parts the calculated concentration is too high. Note that the results depend on the grid resolution: 500 layers result in a lower concentration than 100 layers, which suggest that full convergence has not yet been reached for 100 layers.

Sediment concentrations as a function of time at several levels for case C1 are plotted in Fig. 15. Moreover, for three levels ($z=3.2$, $z=0.7$ and $z=0.2$ cm, Figs. 16, 17 and 18) calculated profiles are compared with measured profiles. The calculated concentration at $z=0.7$ cm is much too high, whereas the concentrations at $z=3.2$ and $z=0.2$ cm are about right. Calculated and measured peaks during a wave cycle roughly coincide.

In Figure 19 the sediment flux is plotted as a function of z . Although the POINT SAND model does not perform worse than other published models (Davies et al., 1997), the measured reversal of sediment transport at about 2 cm above the bed is not reproduced. Moreover, the sediment flux near the bed appears to be too high.

7.5 Sand transport by waves and wave-driven current

We refer to Appendix G containing our paper for the ICCE symposium on sand transport in wave-driven currents using the POINT-SAND model. This paper compares observations in the wave tunnel with simulations but this paper presents just simulations of sand transport under free-surface waves without comparison to observations. The paper assesses the differences between rigid-lid wave tunnel and free-surface wave channel experiments as well as their contradictory influence on estimating onshore or offshore sand transport in the field.

Figure 5 of Appendix G compares simulations to observations for the wave-tunnel case E1 of an oscillatory flow superimposed on a current. This figure shows deviations from wave-tunnel observations similar to those noted in Figure 14 and 19 (case C1).

The most prominent deviations between simulation and wave-tunnel observations are the vertical profiles of mean sand concentration. Of course these strong deficiencies, note the application of logarithmic axes in the relevant figures, require serious study. It is expected that the POINT SAND model offers the efficient tool for it because that was the essential objective of its design.

These and other findings are repeated in the final Chapter 8.

8 Conclusions, discussion and recommendations

8.1 Conclusions

Hydrodynamic and wave conditions

This report with Appendices F and G demonstrates the applicability of the POINT-SAND model to the following flow configurations:

- Constant-flow channel (free surface);
- Confined wave tunnel (rigid lid);
- Field conditions without surface waves (wind-driven and tidal currents, varying water depth, varying flow direction);
- Combined wave-current channel (free surface, waves parallel to flow); or
- Field conditions with surface waves (wave propagation irrespective of flow direction).

Due to the one-dimensional nature of the POINT SAND model the following hydrodynamic conditions cannot be simulated explicitly:

- breaking waves;
- flow and waves with strong horizontal gradients;
- flow over ripples;
- secondary or Langmuir circulation driven by the CL vortex force.

Waves or horizontal oscillatory motions

- The POINT SAND model is designed for simulating wave tunnel experiments i.e. a horizontally oscillating flow without a coherent wave-related vertical velocity component;
- The same POINT SAND model has separate routines for simulating each spectral component of true orbital motions of waves propagating at arbitrary angle on a turbulent shear flow;
- The POINT SAND model simulates each component of a given wave spectrum with independent wave amplitudes, phase lags and propagation directions;
- The surface boundary conditions are imposed at the still water level (rigid-lid approximation);
- The rigid-lid approximation does not allow for the explicit simulation of the Stokes drift but that is included by a theoretical model. Instead, the Stokes drift for sand mass is simulated explicitly as long as the sand concentration is zero at the still water level;
- In principle, the rigid-lid approximation is too crude for representing the delicate surface boundary-layer flow in case of wave-current interaction in laminar stagnant water;
- Presently, for wave tunnel experiments, the POINT SAND model allows for forcing/prescribing the horizontal velocity at some given level in terms of given time series or harmonics.

Modelling turbulence

- The implemented turbulence models are based on eddy viscosity/diffusivity closures (Boussinesq hypothesis) for high-Reynolds turbulence;
- Nevertheless, the user can choose between no-slip conditions or partial-slip conditions for a hydraulically rough bed;
- A so-called high-pass filter function is derived that weights the turbulence-generating part of the wave-induced strain rates per spectral component;
- By its nature, the high-pass filter function is applicable only in wave-current simulations (wave channel or the field) but not for the wave-tunnel cases;
- The sand-water mixture is treated as a quasi single-phase fluid with variable density differences acting through the gravity term only (Boussinesq approximation). Turbulence damping by this quasi-buoyancy effect is included in the turbulence models;
- The laminar-turbulence and turbulence-laminar transitions are not included in the (high-Reynolds) turbulence models, although the high-pass filter function appears to mimic this phenomenon after flow reversal.

In terms of mean current profile and wave amplitudes, the hydrodynamic module in the POINT-SAND model simulates the wave-current experiments of Klopman (1994) and also the wave-tunnel experiments well.

Sand transport

- The sand-water mixture is treated as a quasi single-phase fluid with variable density differences acting through the gravity term only (Boussinesq approximation);
- Multiple sand fractions with different grain sizes are allowed;
- The settling velocity depends on grain size and on the time and space varying volume fraction (Richardson & Zaki formulation);
- Sand transport is modelled for sheet-flow conditions only;
- The simulation of vertical sand transport by waves includes the vertical orbital velocity component;
- The Stokes drift and streaming of sand mass is simulated explicitly as long as the sand concentration is zero at the still water level.
- The Zyserman-Fredsøe formulation for bed concentration is applied with the option of prescribing it as bed concentration or as a flux formulation;
- The built-in test case (Appendix E) allows the user to check his selection of numerical parameters and to appreciate the large sensitivity of the simulated depth-integrated sand flux to numerical methods, turbulence models, state parameters and user-defined input parameters;
- The k-L model matches the theoretical results well so that we recommended using this model for this particular test case allowing for easily recording deviations by other parameter of process choices;
- Our comparison with wave tunnel experiments shows that at the current level of development, the results with the POINT-SAND are comparable to 1DV models such as discussed in (Davies *et al.*, 1997). This is expected since for the idealised wave tunnel conditions, the underlying model equations reduce to equations similar as used in the wave boundary layer models described in (Davies *et al.*, 1997);

- We believe to have explored more thoroughly the sensitivity of our simulations to various numerical methods and parameter settings than published by others. We found that the simulation poorly converges and convergence is obtained at significantly more grid points than others publish their results.

8.2 Discussion

Hydrodynamics

We experienced a sensitivity of the simulations to time step and relaxation time for smoothing the numerical determined wave-current interaction (WCI) force. Under certain conditions this WCI force exhibits slow oscillations in time as well along the depth coordinate. These oscillations can be checked by the user because the WCI force is written to output in time series per z level as well as in depth records per time interval. Presently, we do not have a thorough rule-of-the thumb for the appropriate time integration input parameters, or a more robust scheme for better converging the WCI force to steady state, so that experience and careful testing is required.

Sand transport

- Despite the accurate simulation of analytic solutions (built-in test case), the comparison with observations in the wave tunnel is in general not satisfactory and occasionally even poor;
- This discrepancy suggests deficiencies in the implemented sand transport formulations in conjunction with some remaining deficiencies in turbulence modelling (e.g. laminar-turbulence transition at flow reversal);
- More analysis on the precise causes of the poor results is needed. This analysis may require additional options such as simulating sand transport using experimentally observed concentration signals (time series). This approach then by-passes some of the disputable sand transport closures.
- Comparisons should also be made outside the sheet flow regime, as bed ripples are commonplace both in laboratory tests and in the field. The effect of ripples on bringing and keeping sediment in suspension and the implications for sediment transport model need further research. Strictly speaking, the formulations used in this report are valid only for plane beds. The knowledge of sediment transport above rippled beds is limited such that it is difficult to properly model a rippled bed situation. Due to this lack in knowledge, in coastal engineering practice today, models for flat bed situations are often applied to rippled bed situations, using an increased bed roughness related to the ripple dimensions.

8.3 Recommendations

The previous conclusions and discussions yield the following recommendations.

Improving or extending the POINT SAND model

- The occasional oscillatory adjustment of the numerically determined WCI force must be eliminated. In view of our attempts this is expected to be a serious enterprise;
- The implementation of Reynolds Stress Models (RSM's) should avoid the application of the high-pass filter function for eddy viscosity closures. In principle, RSM's allow for a more suitable simulation of the response of turbulence to rapid oscillatory motions in wave tunnels or in wave channels;
- The implementation of Radder's model (Dingemans, 1999) on the net effect of secondary or Langmuir circulation on momentum exchange and mass transport;
- The design and implementation of a model about the role of bed ripples on turbulence production and momentum exchange e.g. by using analytic solutions or Direct Numerical Simulations (DNS) of the turbulent flow over wavy beds;
- In literature on particulate industrial flows, various models are given for the dependence of the settling velocity on turbulence levels as well as on turbulence damping;
- The piecewise approximations (6.2) and (6.4) to the settling velocity and Shields parameter are discontinuous and therefore should be replaced by continuous functions;
- Sediment in laminar shear flows also exhibit dispersion for which a thoroughly tested closure is available;
- The large sediment concentrations near the bed violate Boussinesq assumption i.e. the variable density of the sand-water mixture should also be included in the momentum equations;
- Rather than using some closure for the bed concentration, we recommend simulating the soil-mechanical and pore-pressure response on-line coupled to the hydrodynamic simulation;
- Prescription of sand concentration at some given level by time series derived from observations for by-passing or testing the empirical formulations of sand concentration near the bed;
- Extension of built-in test cases with analytic solutions for oscillatory flows such as presented in (Bosboom, 1999).

Data analysis

Nearly all tests cases in this report compare mean flow and wave amplitudes. We recommend further testing of turbulence and drift properties but this requires additional data analysis also dedicated to further model developments:

- Turbulence properties derived from the extensive wave-current data sets in (Klopman, 1994);
- Additional checks on wave amplitudes and wave reflections derived from observations (Klopman, 1994);
- Estimation of Stokes drift from (Klopman, 1994);

- Averaged properties of mean-flow, turbulence and sand transport derived from DNS of mean or oscillatory flows over plane and wavy beds including sand transport, e.g. (Vittori & Verzicco, 1998) and (Boersma, 2000).

Simulations

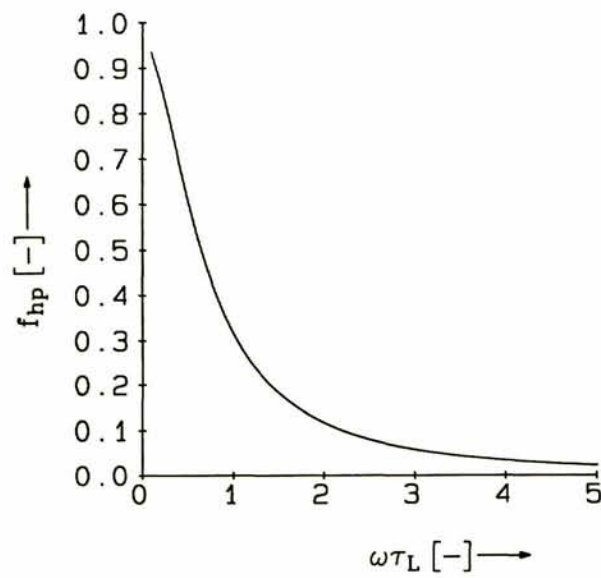
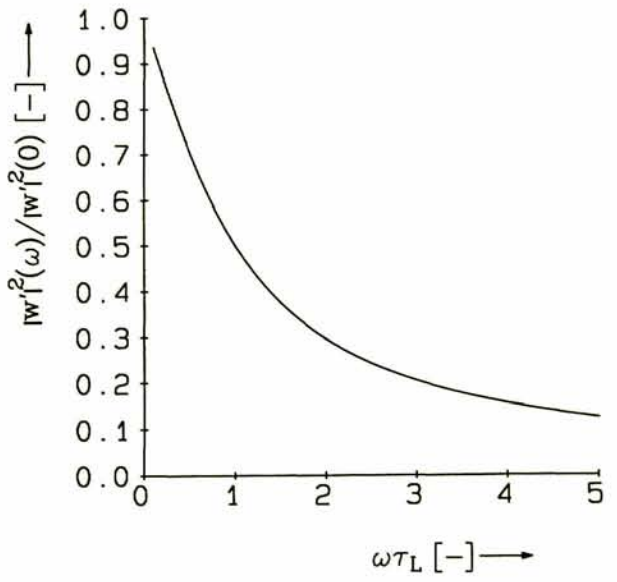
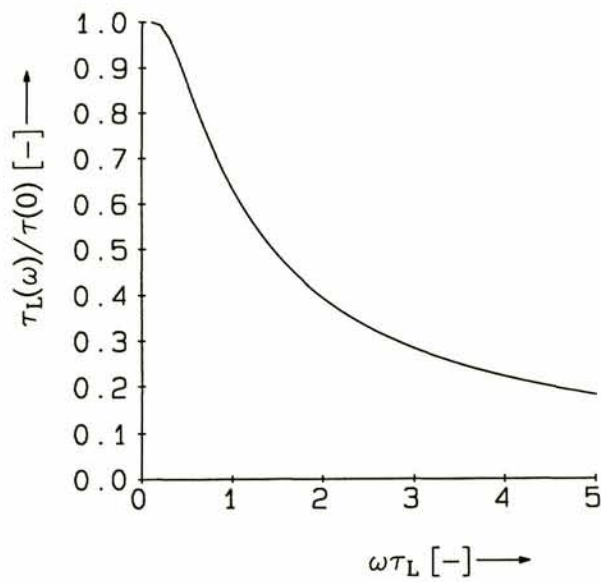
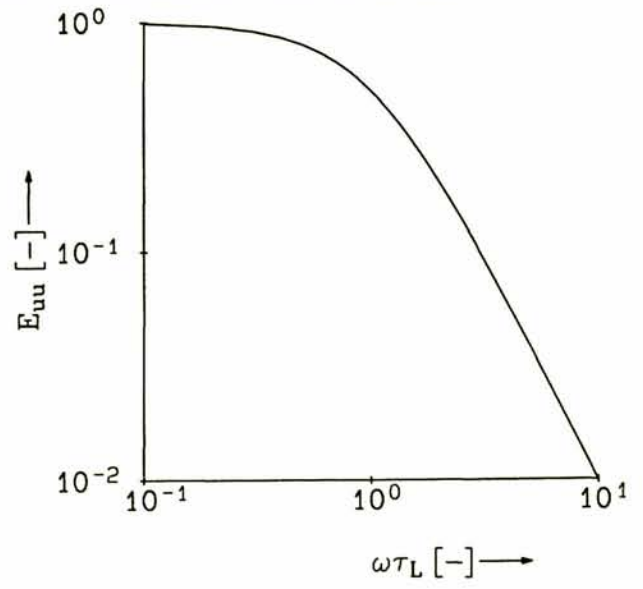
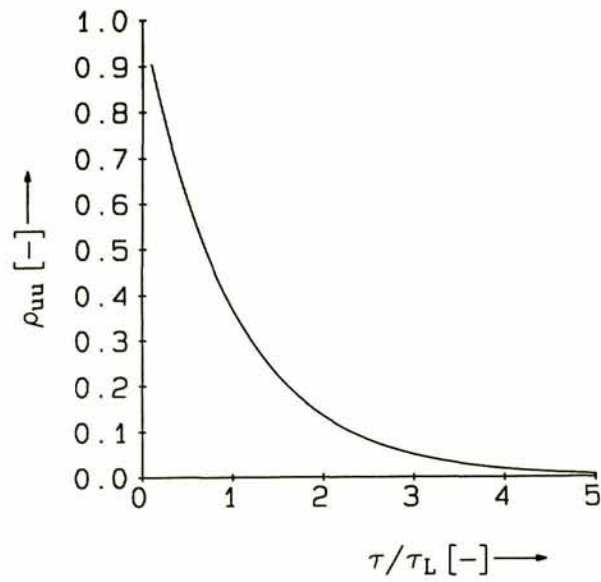
- In view of the demonstrated sensitivity of the simulated as well as theoretical depth-integrated sand flux to changes in input and process conditions, further development of sand transport processes as well as a more thorough analysis of, and inter-comparison with other 1DV models is strongly recommended;
- The first previous tests as well as the first exploration of the POINT-SAND model to sand transport under wave-driven flows demonstrates how this model can assist in research for sand transport in coastal seas. The experiments in Hannover and at Delft University on sand transport under waves are good candidates for further exploration with the POINT-SAND model;
- Ideally, comparison should also be made with field experiments, although it may prove to be hard to obtain a data set with sufficiently accurate near-bed velocities and concentrations. The study of sediment transport in coastal conditions (combined waves and current) is rather problematic, especially since an important part of the sediment transport will occur in the near-bed region. No reliable instruments are available for measuring velocities and sediment concentrations in the field below, say 5 cm above the bed.

References

- Abramowitz, M. & I.A. STEGUN 1972 *Handbook of mathematical functions*. Dover publ
- Al-Salem, A.A. 1993 *Sediment transport in oscillatory boundary layers under sheet-flow conditions*. Ph.D. thesis, Delft University of Technology
- Boersma, B.J. 2000 *DNS of sand transport in turbulent flow over a wavy bed*. Note J.M. Burgers Centrum, The Netherlands and Center for Turbulence Research (Stanford)
- Bosboom, J. & B. Cloin, 1998. 1DV transport models. Report Z2529, WL|Delft Hydraulics
- Bosboom, J. 1999 Analytical model for wave-related sediment transport. Report Z2733.42, WL|Delft Hydraulics
- Bosboom, J., S.G.J. Aarninkhof, A.J.H.M. Reniers, J.A. Roelvink & D.J.R. Walstra 1997 Unibest-TC, Overview of model formulations. Report H2305.42, WL|Delft Hydraulics
- Casulli, V. & G.S. Stelling 1998 Numerical simulation of 3D quasi-hydrostatic free-surface flows. *J. Hydr. Engng.*, Vol. 124, No. 7, July, pp. 678-686
- Davies, A.G., J.S. Ribberink, A. Temperville, J.A. Zyserman, 1997. Comparisons between sediment transport models and observations made in wave and current flows above plane beds. *Coastal Engineering* 31 p163-198
- Deleersnijder, E. & P. Luyten 1994 On the practical advantages of the quasi-equilibrium version of the Mellor and Yamada level 2.5 turbulence closure applied to marine modelling. *Appl. Math. Modelling*, vol. 18, May, pp. 281-287
- Dingemans, M.W., J.A.Th.M. van Kester, A.C. Radder & R.E. Uittenbogaard 1996 The effect of the CL vortex force in 3D wave-current interaction. *Proc. 25th Int. conf. on coastal Engineering*, Orlando, pp. 4821-4832
- Dingemans, M.W. 1999 *3D wave-current modelling*. WL|Delft Hydraulics, report Z2612
- Galperin, B., L.H. Kantha, S. Hasid & A. Rosati 1988 A quasi-equilibrium turbulent energy model for geophysical flows. *J. Atmos. Sc.*, vol. 45, no. 1, Jan., pp. 55-62
- Gradshteyn, I.S. & I.M. Ryzhik 1980 *Table of integrals, series and products; corrected and enlarged edition*. Academic Press
- Groeneweg, J & G. Klopman 1998 Changes of the mean velocity profiles in the combined wave-current motion described in a GLM formulation. *J. Fluid Mech.*, vol. 370, pp. 271-296
- Hinze, J.O. 1975 *Turbulence*. McGraw-Hill Classic Textbook Reissue Series
- Jackson, P.S. 1981 On the displacement height in the logarithmic velocity profile. *J. Fluid Mech.*, vol. 111, pp. 15-25
- Jiang, J.-H., R.L. Street & S.P. Klotz 1990 A study of wave-turbulence interaction by use of a non-linear water wave decomposition technique. *J. Geoph. Res.*, vol. 95, no. C9, Sept. 15, pp. 16,037-16,054
- Katopodi, I., J.S. Ribberink, P. Ruol, R. Koelewijn, C. Lodahl, S. Longo, A. Crosato and H. Wallace, 1994. Intra-wave sediment transport in an oscillatory flow superimposed on a mean current. Data report H 1684.33, Part III, WL|Delft Hydraulics
- Kester, J.A.Th.M. Van, R.E. Uittenbogaard & M.W. Dingemans 1996 *3D wave-current interaction; CL vortex-force, simulation of wave-flume experiments*. WL|Delft Hydraulics, report Z-751, Nov.
- Kester, J.A.Th.M. Van, R.E. Uittenbogaard & E.D. de Goede 1997 *Onderzoek naar numerieke modellering van thermocliene effecten in de Noordzee*. WL|Delft Hydraulics, report Z2034.30, Ma2
- Kitaigorodskii, S.A. & J.L. Lumley 1983 Wave-turbulence interaction in the upper ocean, I, The energy balance of the interacting fields of surface wind waves and wind-induced three-dimensional turbulence. *J. Phys. Oceanogr.*, vol. 13, pp. 1977-1987
- Klopman, G. 1994 *Vertical structure of the flow due to waves and currents*. Progress rep., DELFT HYDRAULICS, H840.32, Part 2
- Kraichnan, R.H. 1956 Pressure fluctuations in turbulent flow over a flat plate. *J. Acoustical Soc. America*, vol. 28, no. 3, May, pp. 378-390
- Mellor, G.L. & T. Yamada 1982 Development of a turbulence closure model for geophysical fluid problems. *Rev. Geophys. Space Phys.*, vol. 20, no. 4, Nov., pp.851-875
- Monin, A.S. & A.M. Yaglom 1975 *Statistical fluid mechanics: mechanics of turbulence*. J.L. Lumley (ed.), vol. 2, MIT Press

- Nezu, I. & W. Rodi 1986 Open-channel flow measurements with a Laser-Doppler Anemometer. *J. Hydr. Engng.*, vol. 110, no. 11, pp. 1613-1641
- Peyret, R. & T.D. Taylor 1983 *computational methods for fluid flow*. Springer Verlag
- Richardson, J.F. & W.N. Zaki 1954 Sedimentation and fluidization. *Trans. Inst. Chem. Engng*, Vol. 32, pp. 35-53
- Rodi, W. 1984 *Turbulence models and their application in hydraulics. A state of the art review*. 2nd revised ed. IAHR, Delft
- Russell, R.C.H., & J.D.C. Osorio 1957 An experimental investigation of drift profiles in a closed channel. *Proc. 6th Conf. Coastal Engng*, Miami, Chapt 10, pp. 171-193
- Rijn, L.C. van, 1987. *Mathematical Modelling of Morphological Processes in the Case of Suspended Sediment Transport. Thesis, Dep. of Fluid Mechanics*, Delft University of Technology, Delft, The Netherlands
- Rijn, L.C. van, 1993. *Principles of sediment transport in rivers, estuaries and coastal seas*. Aqua Publ. (The Netherlands)
- Sato & K. Yamamoto 1987 Lagrangian measurement of fluid-particle motion in an isotropic turbulent field. *J. Fluid Mech.*, vol. 175, pp. 183-199
- Tennekes, H. & J.L. Lumley 1983 *A first course in turbulence*. MIT Press (ninth printing)
- Uittenbogaard, R.E., J.C. Winterwerp, J.A.Th.M. van Kester & H. Leepel 1996 *3D cohesive sediment transport; part I: text, part II: figures and appendices*. WL|Delft Hydraulics, report Z-1022, March
- Uittenbogaard, R.E., J. Bosboom & Th. van Kessel 1999 *Numerical simulation of wave-current driven sand transport; theoretical background of the beta release of the POINT SAND model*. WL|Delft Hydraulics, report Z2733.41, November
- Uittenbogaard, R.E 2000 *Overview of the POINT SAND model*. WL|Delft Hydraulics, report Z2899.10, October
- Van Dyke, M. 1975 *Perturbation methods in fluid mechanics*. Parabolic Press, Stanford
- Velthuisen, H.G.M. & L. van Wijngaarden 1969 Gravity waves over a non-uniform flow. *J. Fluid Mech.*, vol. 39, part 4, pp. 817-829
- Vittori, G. & R. Verzicco 1998 Direct simulation of transition in an oscillatory boundary layer. *J. Fluid Mech.*, vol. 371, pp. 207-232
- Winterwerp, J.C. and R.E. Uittenbogaard, 1997, *Sediment transport and fluid mud flow*. Report Z2005, WL|Delft Hydraulics
- Zyserman, J.A. and J. Fredsøe, 1994. Data analysis of bed concentration of suspended sediment. *Proc. Am. Soc. Civ. Eng., Journal of Hydraulic Engineering*, 120(9):1021-1042.

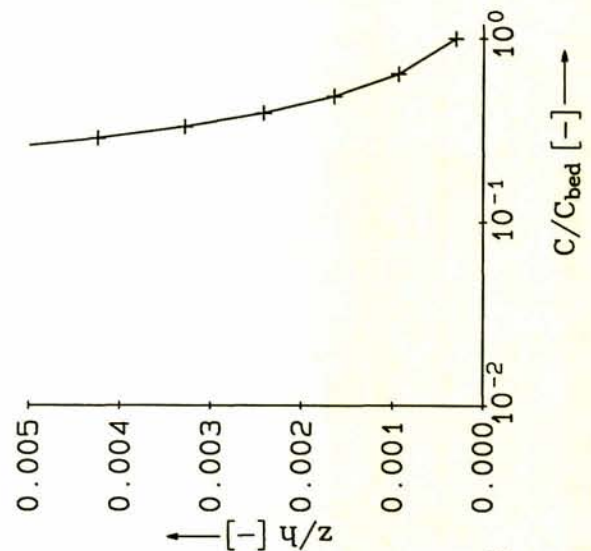
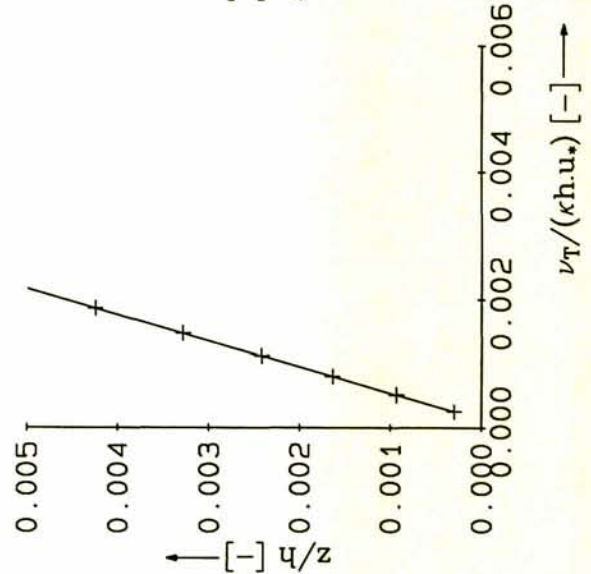
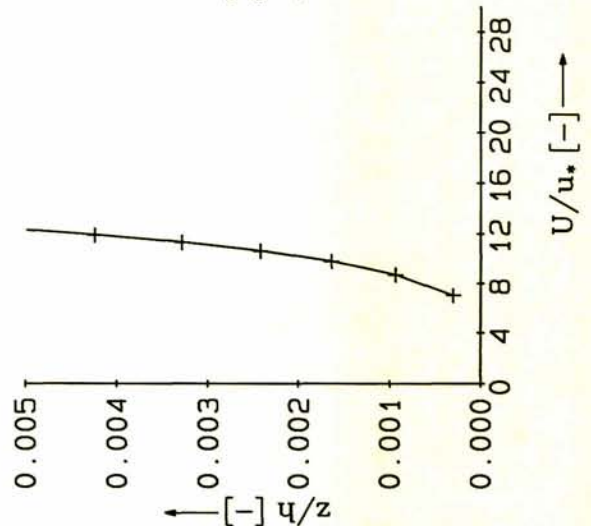
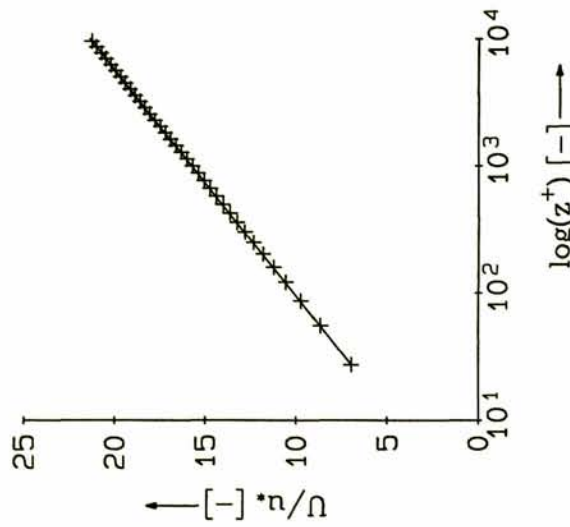
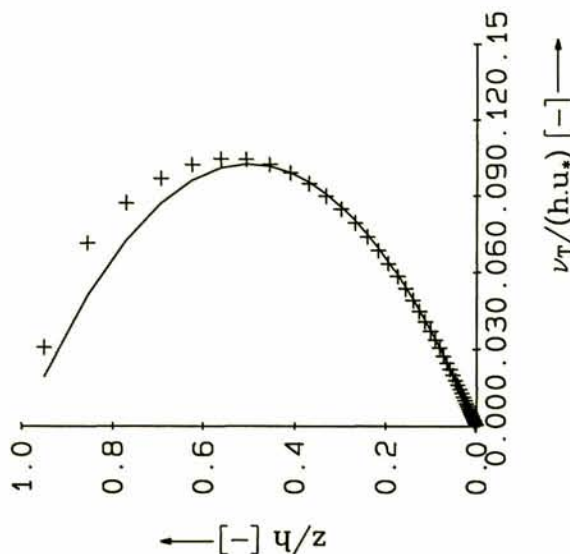
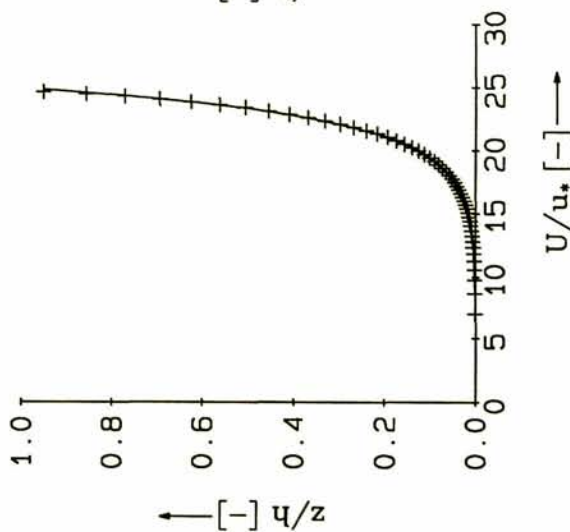
Figures



Terms for wave-turbulence interaction.

c:\dpm\surrwav\subinv

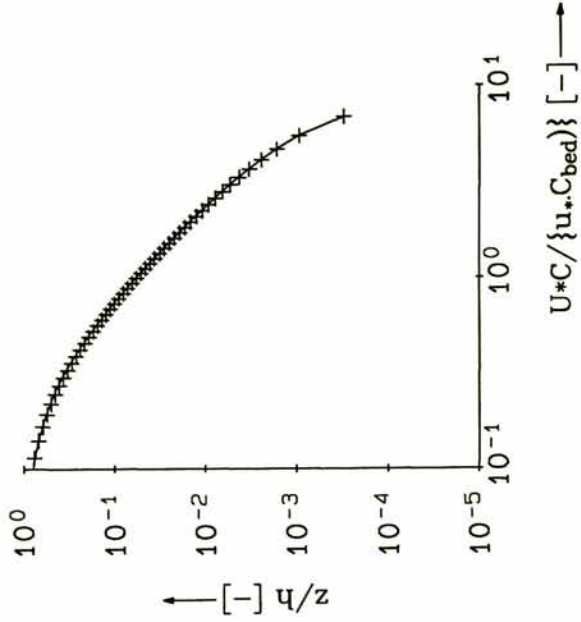
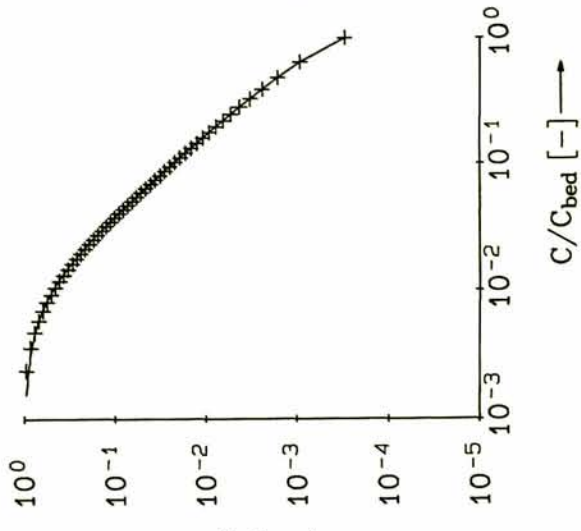
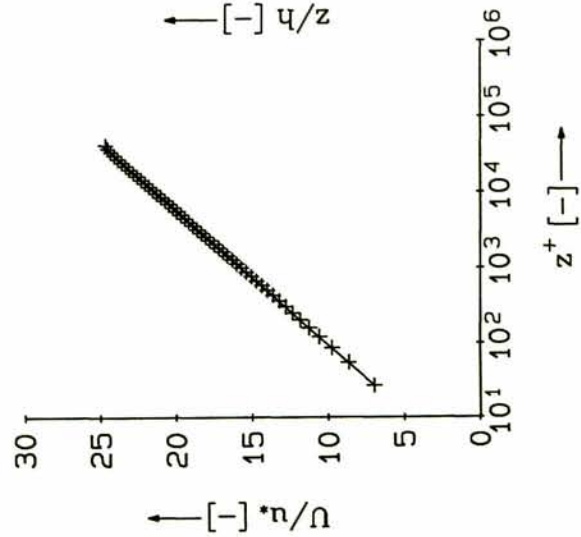
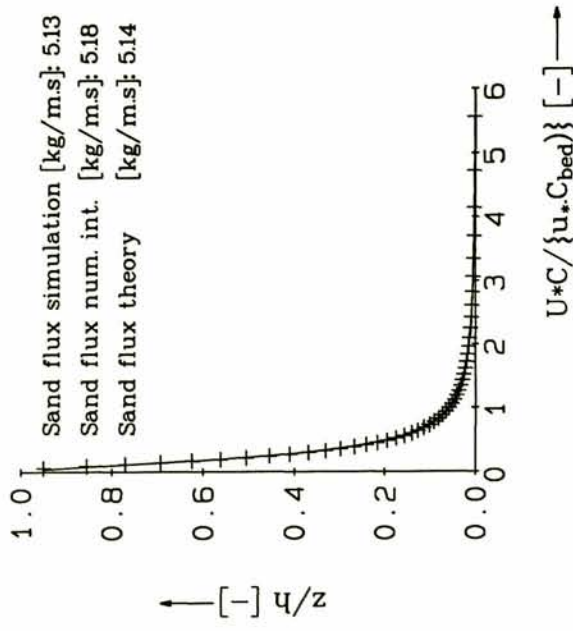
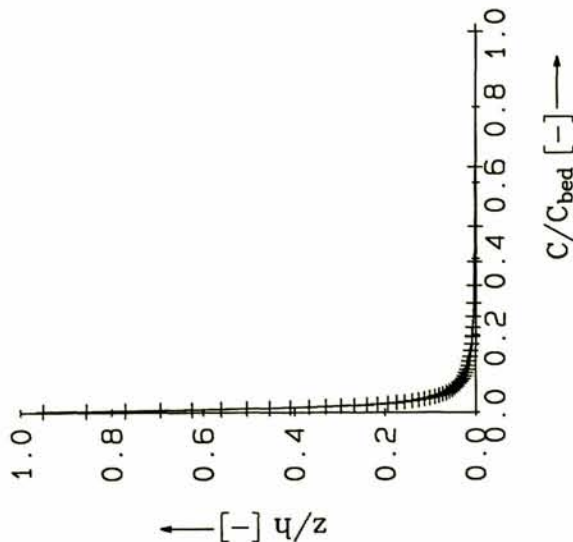
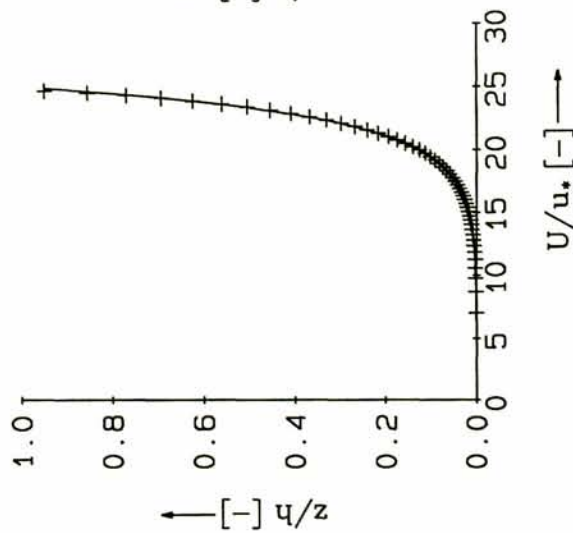
+model — Log/Rouse profile



Built-in test case ; $H=1$ [m] ; $U=1$ [m/s] ; partial slip ;
 exponential layer distribution with $k-l$ model ;
 Comput. bed layer 0.6 [mm] ; 50 layers ; 150 [μm] sand ;
 Central scheme for vertical advection.

d:\dpm\sedmoc\pltlog.kll

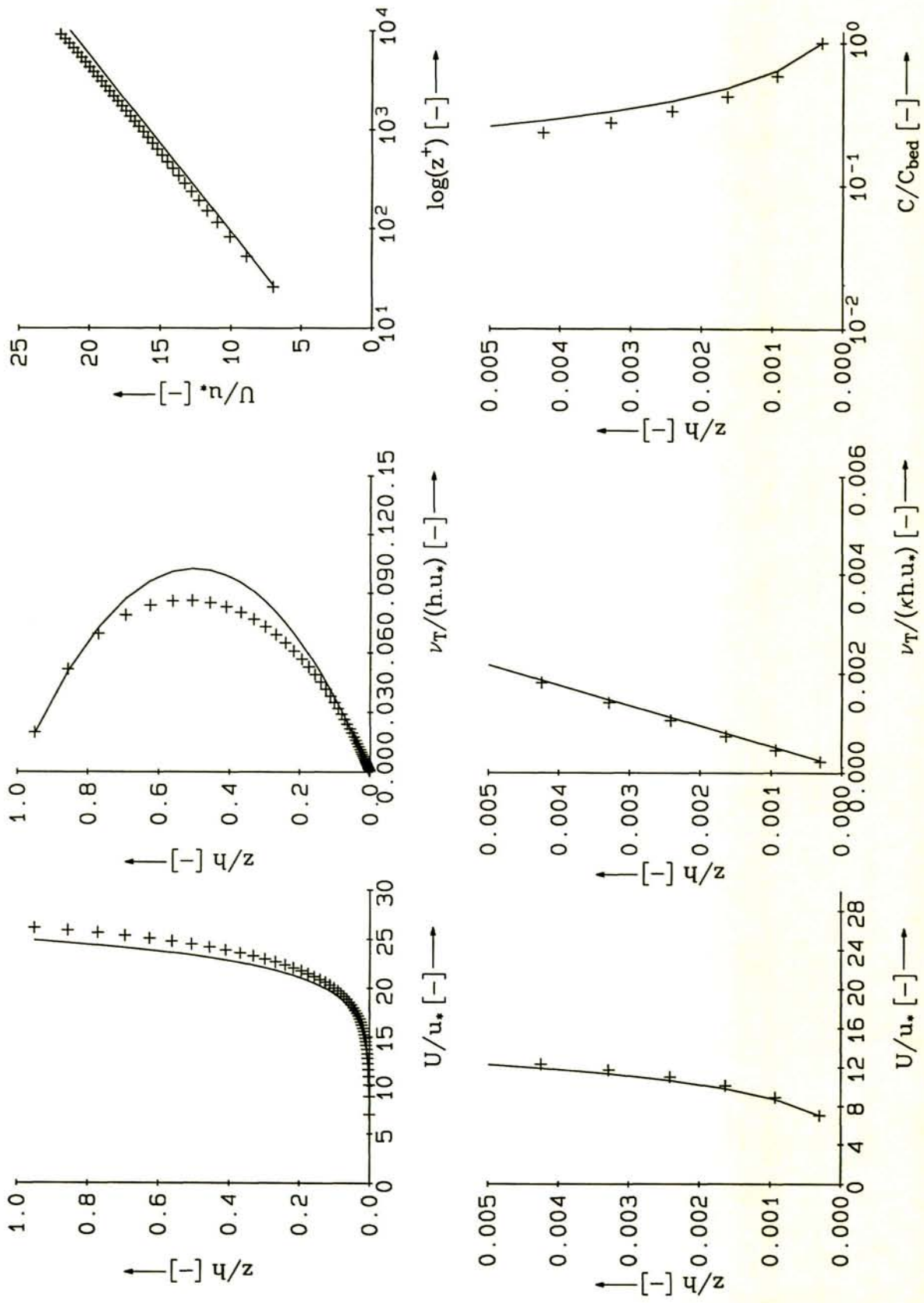
+model — Log/Rouse profile



Built-in test case ; $H=1$ [m] ; $U=1$ [m/s] ; partial slip ;
 exponential layer distribution with $k-l$ model ;
 Comput. bed layer 0.6 [mm] ; 50 layers ; 150 [μ m] sand ;
 Central scheme for vertical advection.

d:\dpm\sedmoc\sedlog.kll

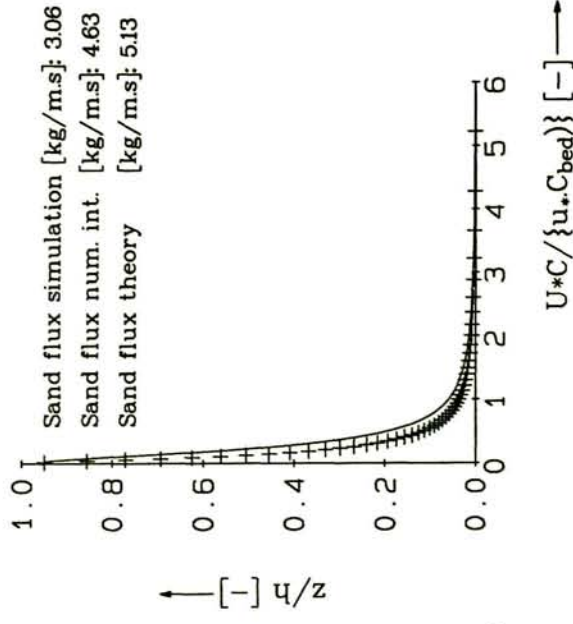
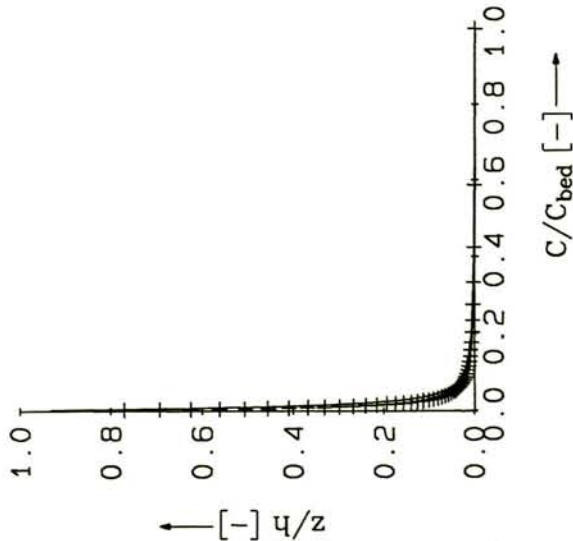
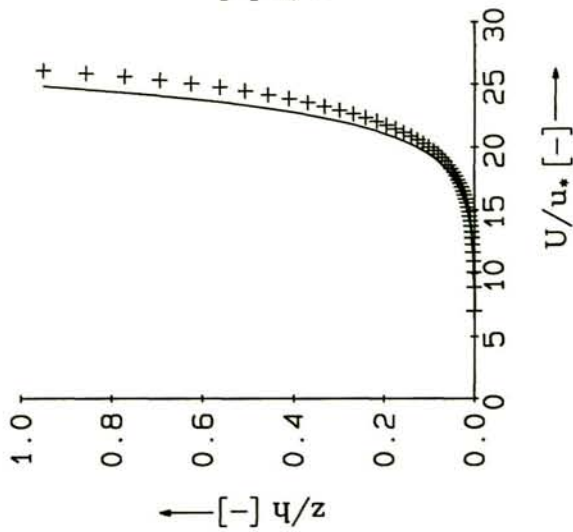
+model — Log/Rouse profile



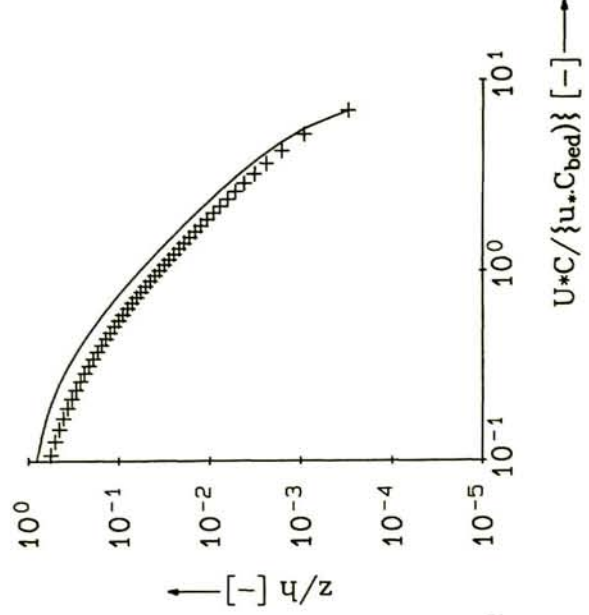
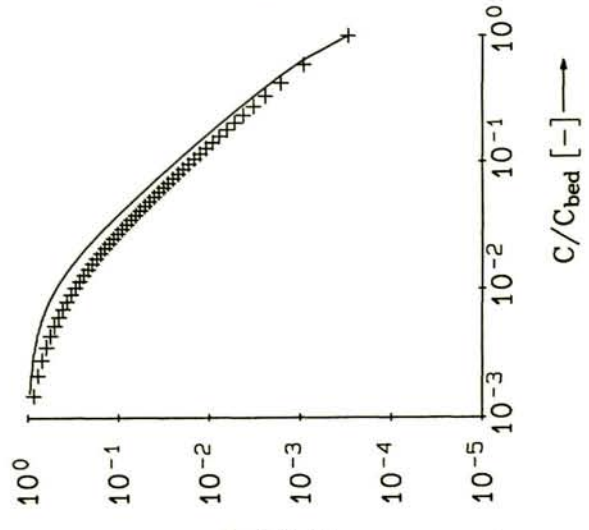
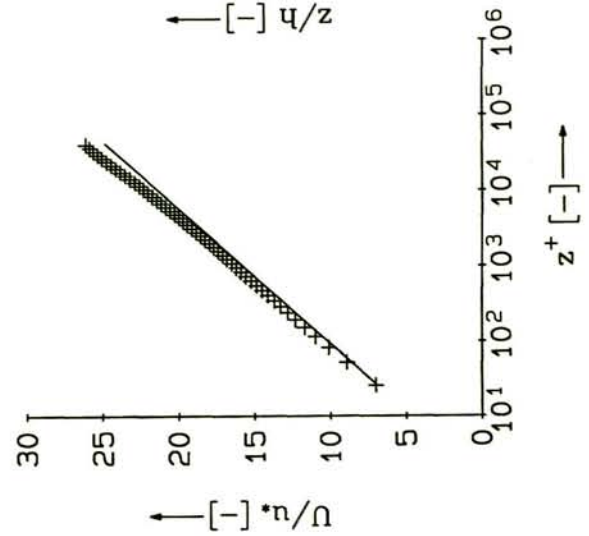
Built-in test case ; H=1 [m] ; U=1 [m/s] ; partial slip ;
 exponential layer distribution with k-ε model ;
 Comput. bed layer 0.6 [mm] ; 50 layers ; 150 [μm] sand ;
 Central scheme for vertical advection.

d:\dpm\sedmoc\pltlog.ke2

+model — Log/Rouse profile



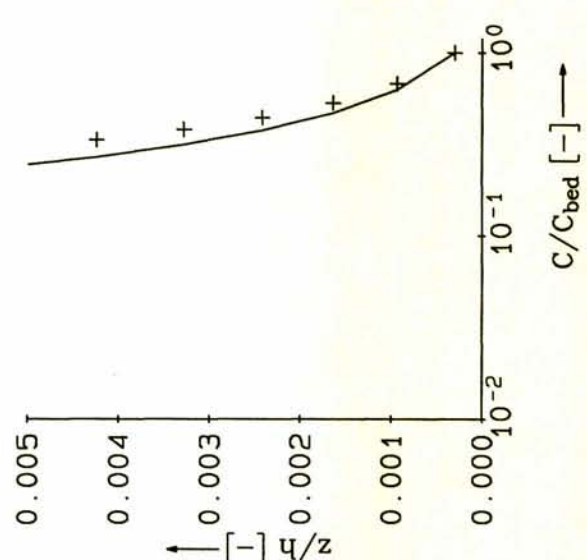
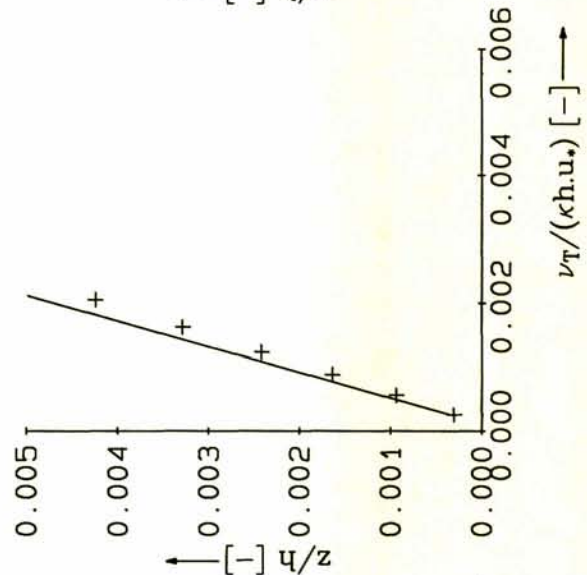
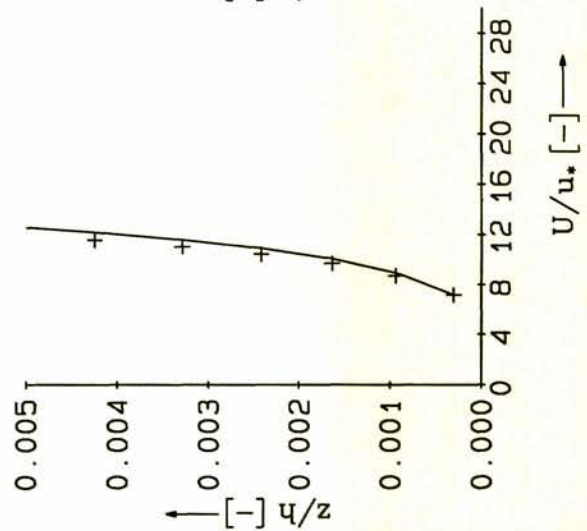
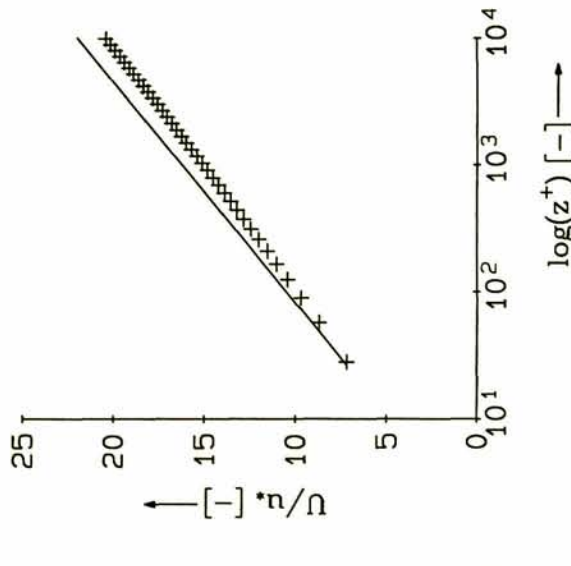
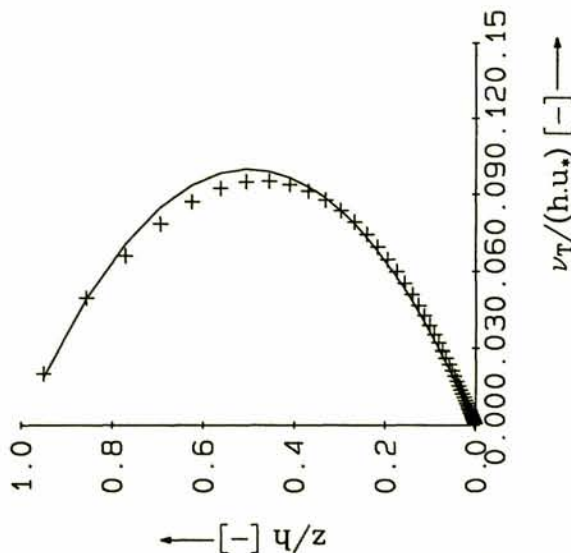
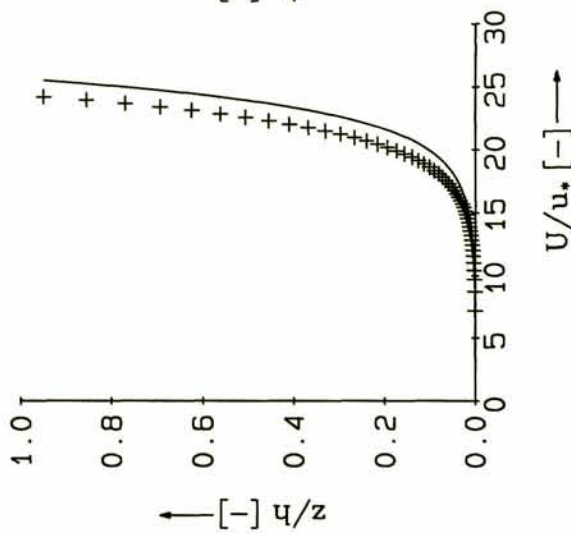
Sand flux simulation [kg/m.s]: 3.06
 Sand flux num. int. [kg/m.s]: 4.63
 Sand flux theory [kg/m.s]: 5.13



Built-in test case ; H=1 [m] ; U=1 [m/s] ; partial slip ;
 exponential layer distribution with k-ε model ;
 Comput. bed layer 0.6 [mm] ; 50 layers ; 150 [μm] sand ;
 Central scheme for vertical advection.

d:\dpm\sedmoc\sedlog.ke2

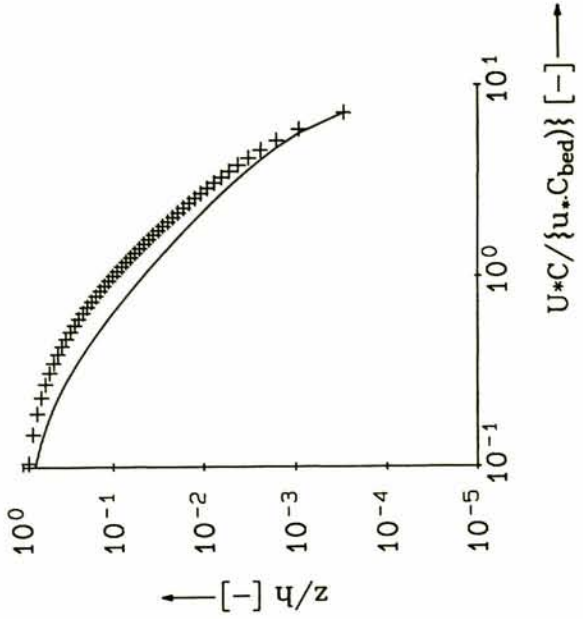
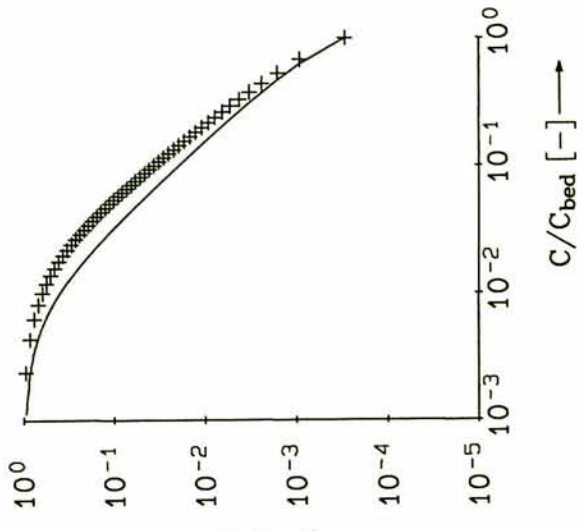
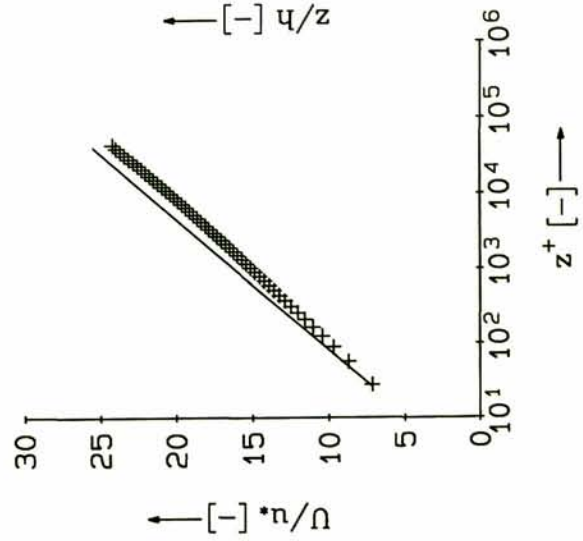
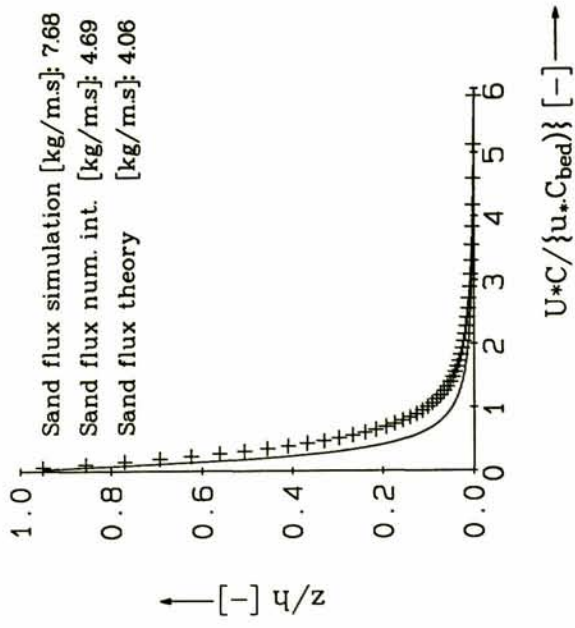
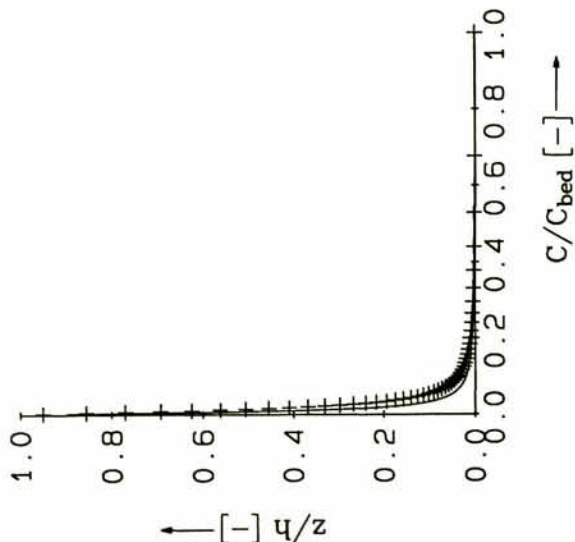
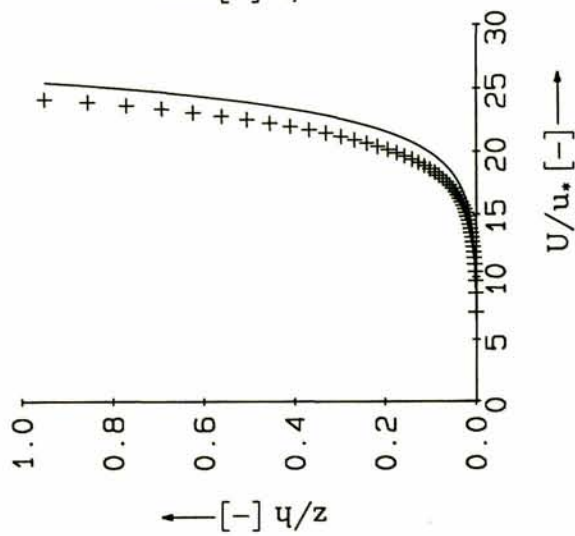
+model — Log/Rouse profile



Built-in test case ; $H=1$ [m] ; $U=1$ [m/s] ; partial slip ;
 exponential layer distribution with Davies $k-l$ model ;
 Comput. bed layer 0.6 [mm] ; 50 layers ; 150 [μm] sand ;
 Central scheme for vertical advection.

d:\dpm\sedmoc\pltlogkd3

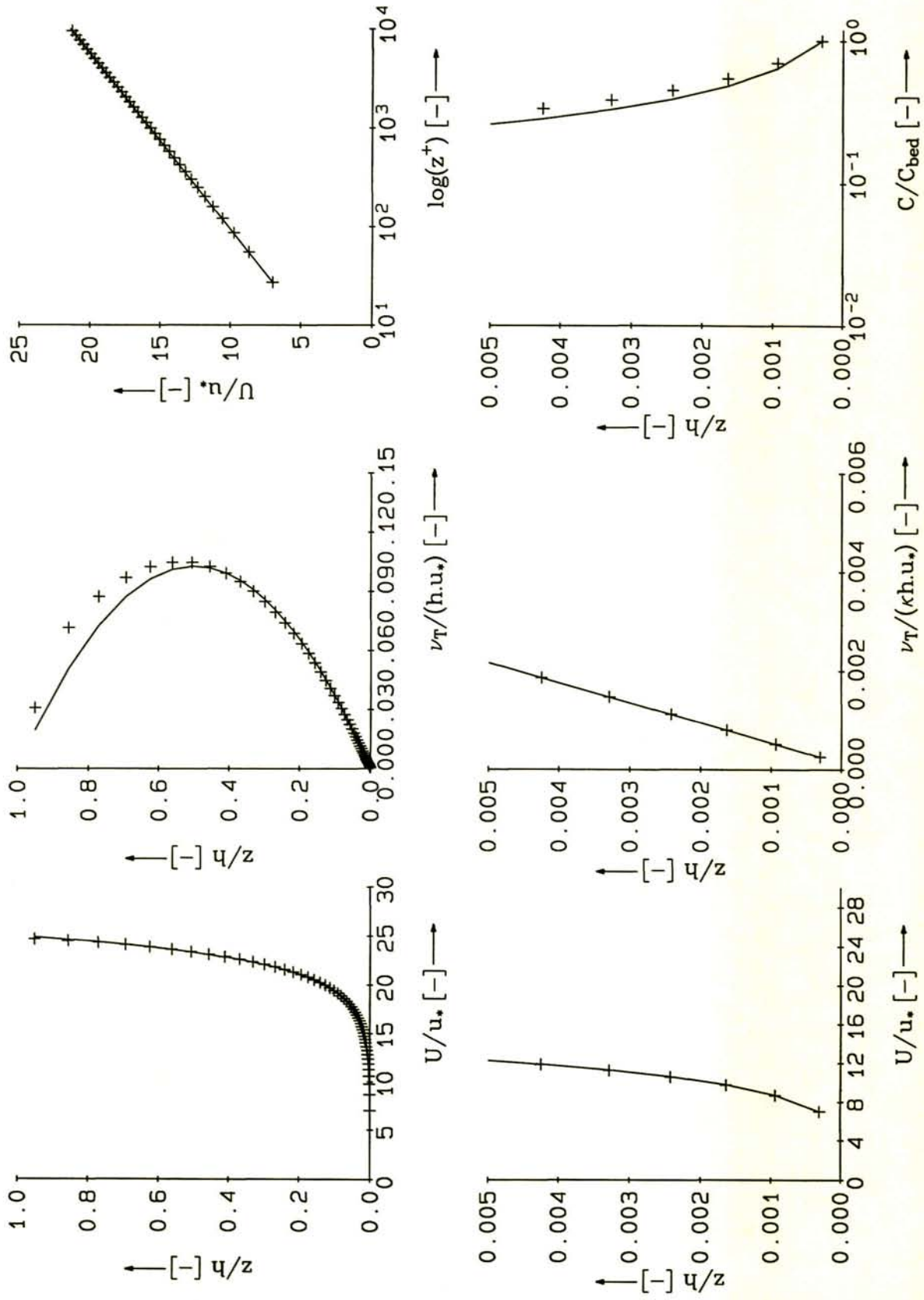
+model — Log/Rouse profile



Built-in test case ; $H=1$ [m] ; $U=1$ [m/s] ; partial slip ;
 exponential layer distribution with Davies $k-l$ model ;
 Comput. bed layer 0.6 [mm] ; 50 layers ; 150 [μ m] sand ;
 Central scheme for vertical advection.

d:\dpm\sedmoc\sedlog.kd3

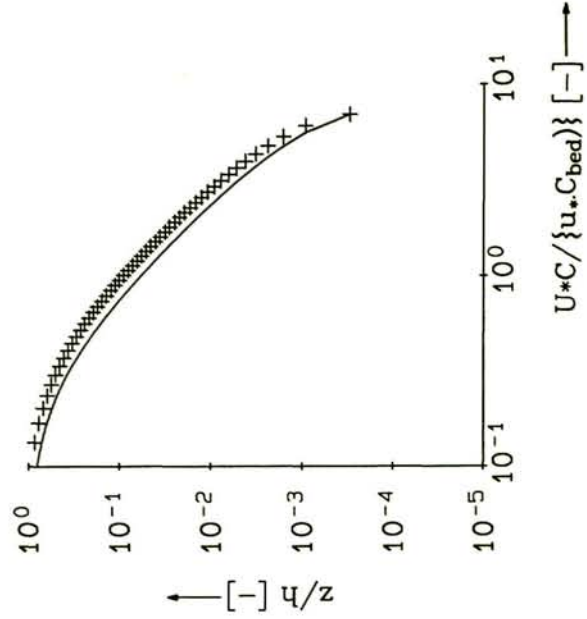
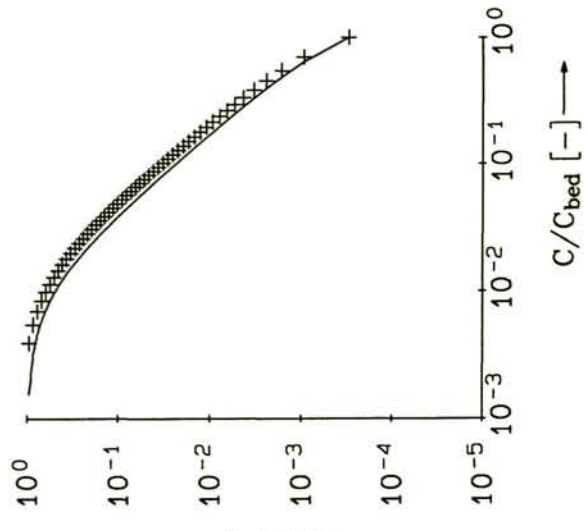
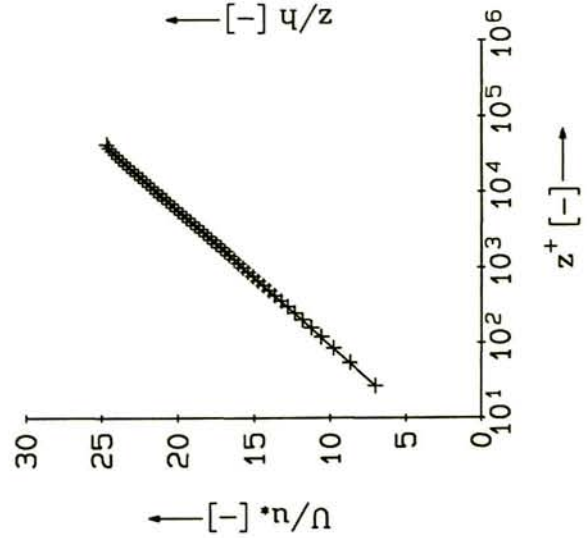
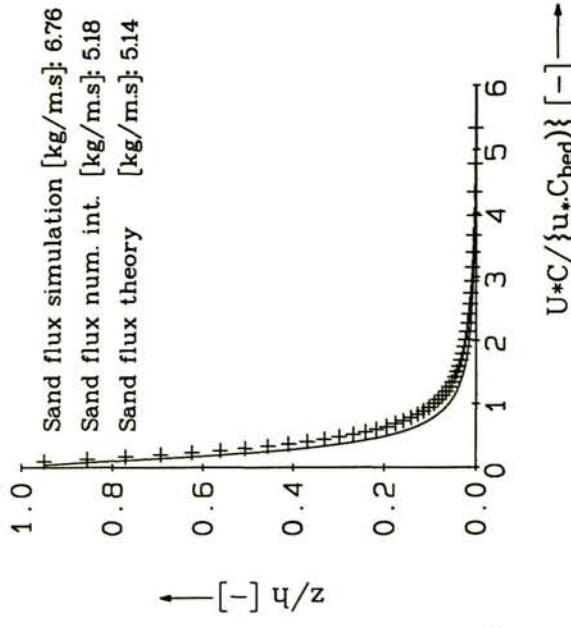
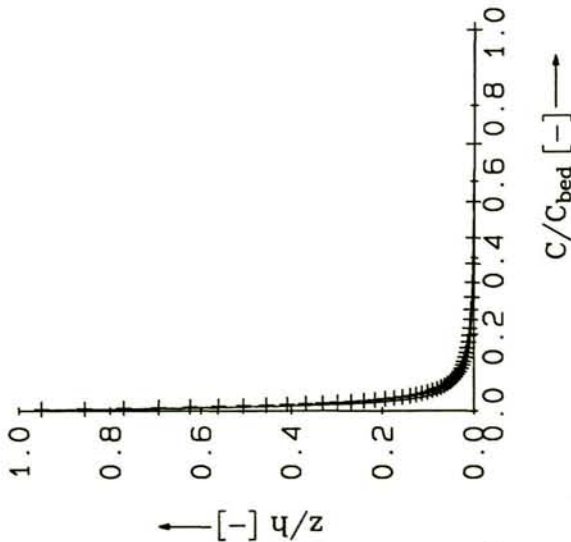
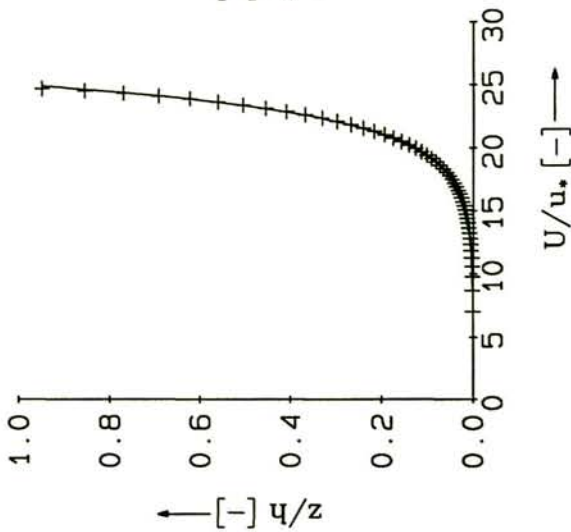
+ model — Log/Rouse profile



Built-in test case ; $H=1$ [m] ; $U=1$ [m/s] ; partial slip ;
 exponential layer distribution with $k-l$ model ;
 Comput. bed layer 0.6 [mm] ; 50 layers ; 150 [μm] sand ;
 First-order upwind scheme for vertical advection.

d:\dpm\sedmoc\ptlog.kl4

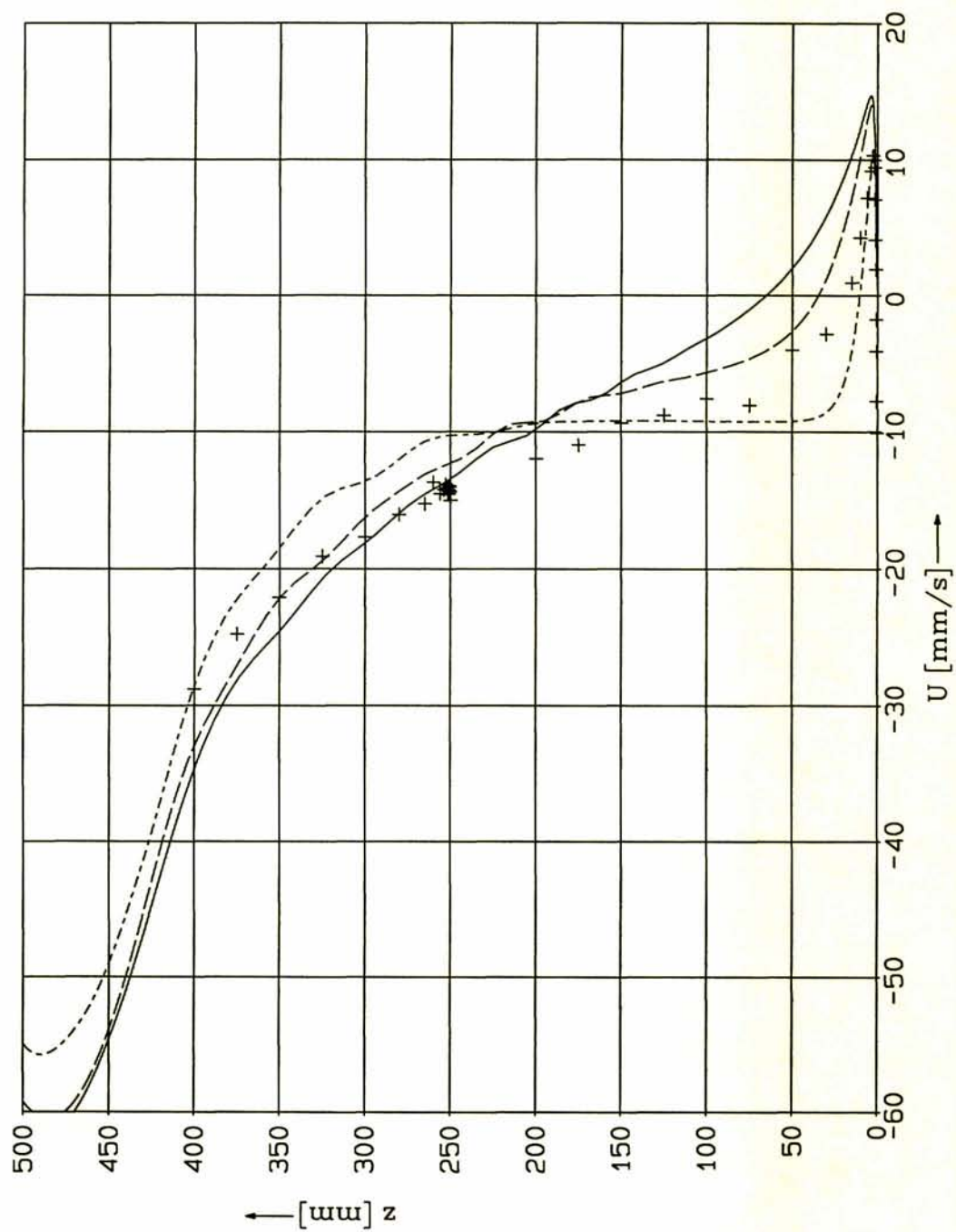
+model — Log/Rouse profile



Built-in test case ; $H=1$ [m] ; $U=1$ [m/s] ; partial slip ;
 exponential layer distribution with $k-l$ model ;
 Comput. bed layer 0.6 [mm] ; 50 layers ; 150 [μm] sand ;
 First-order upwind scheme for vertical advection.

d:\dpm\sedmoc\sedlog.k14

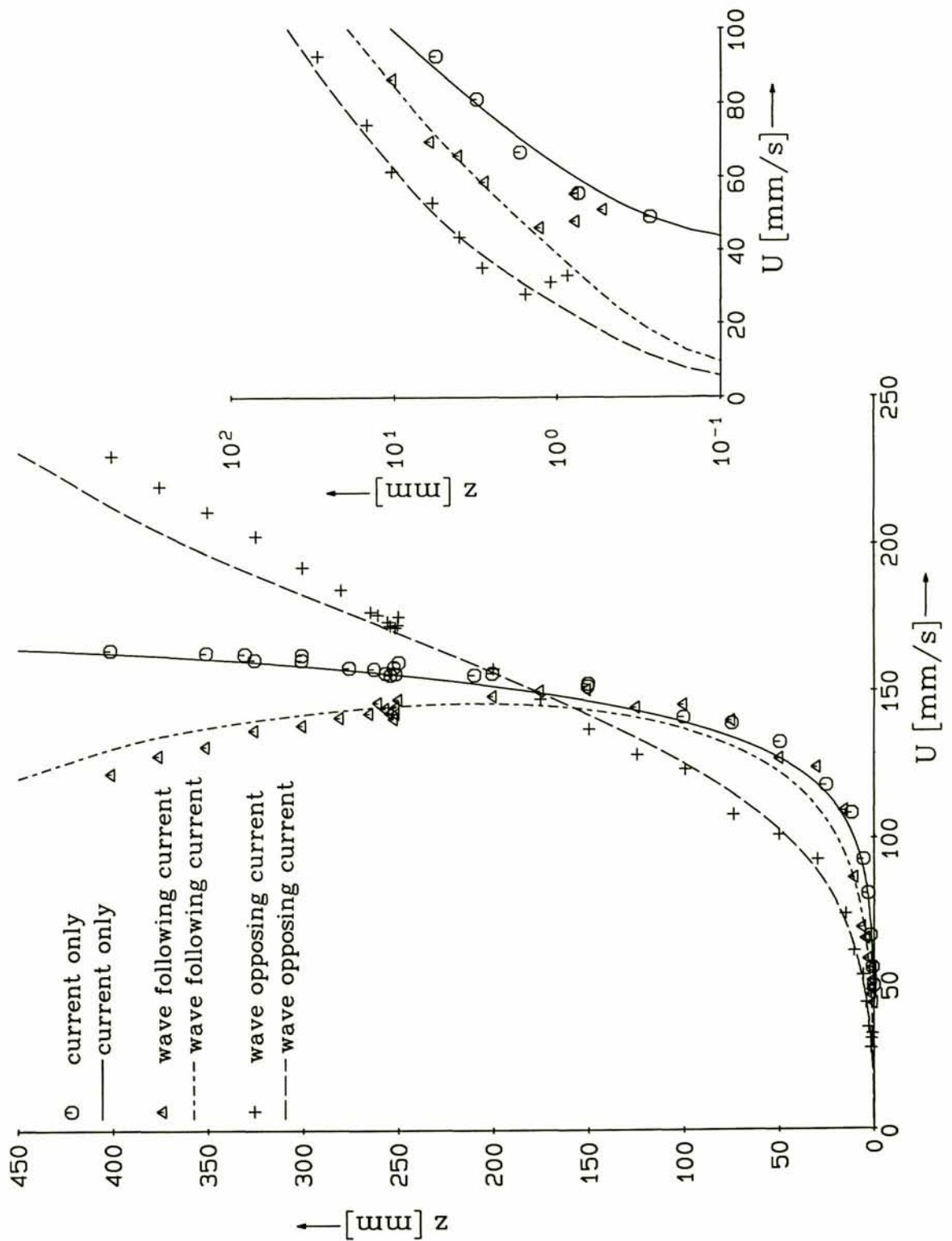
- - - after 50 wave periods
 - - - after 100 wave periods
 — after 150 wave periods
 + observations



Wave-current interaction with the POINT-SAND model.
 Monochromatic wave without current ; case WMN (Klopman, 1994);

150 double-exponential layers
 0.1 mm bed and top layer

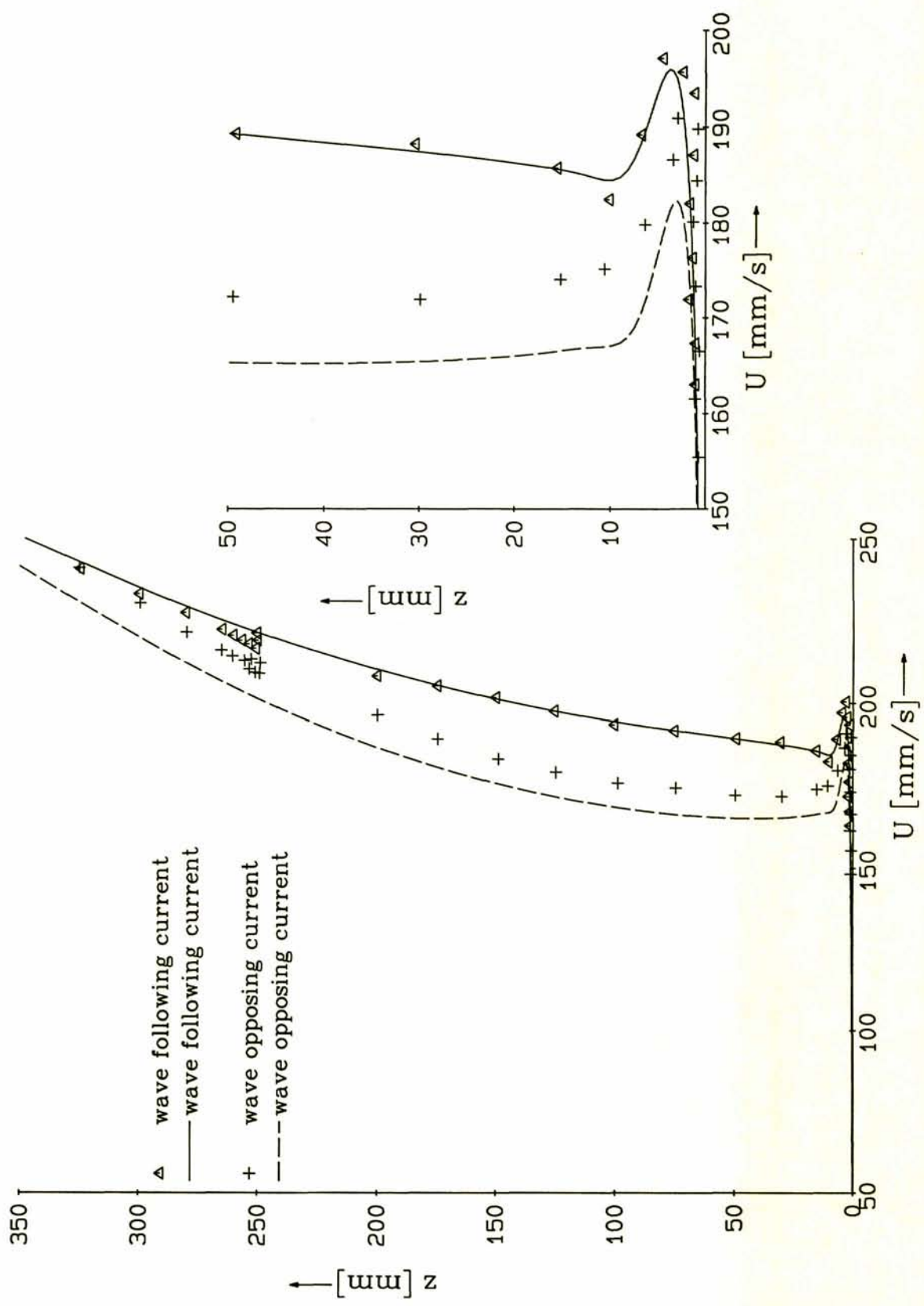
c:\dpm\vrijdag\wmn.inv



Wave-current interaction with POINT-SAND model.
Simulation of monochromatic waves following the current;
case CMP of (Klopman, 1994). Mean current profiles.

150 exponentially incr. layers
k-L turb. mod. with h.p. filter

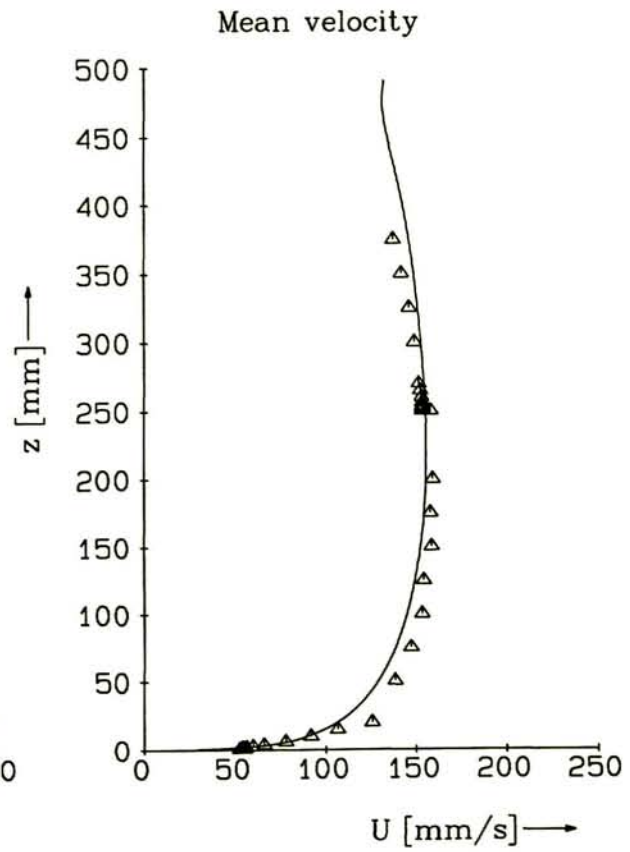
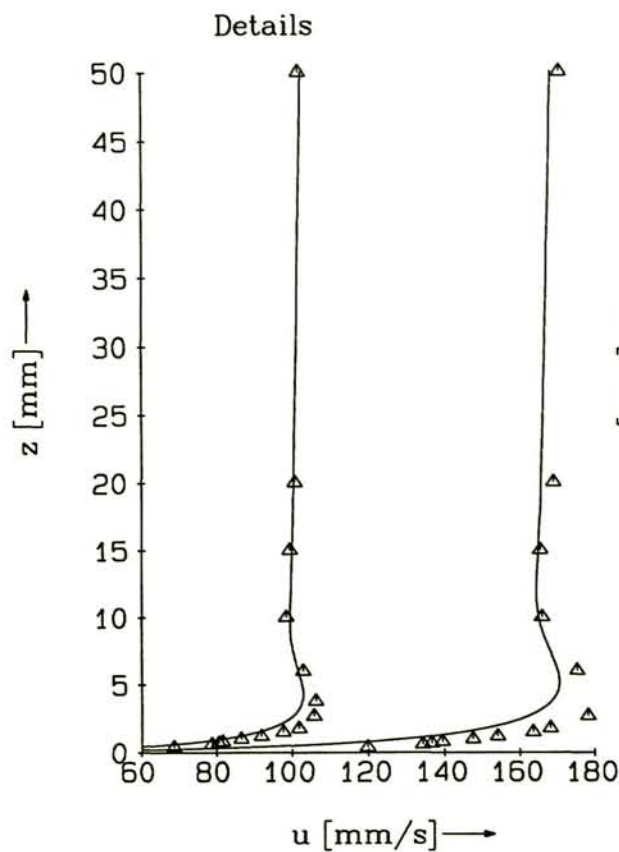
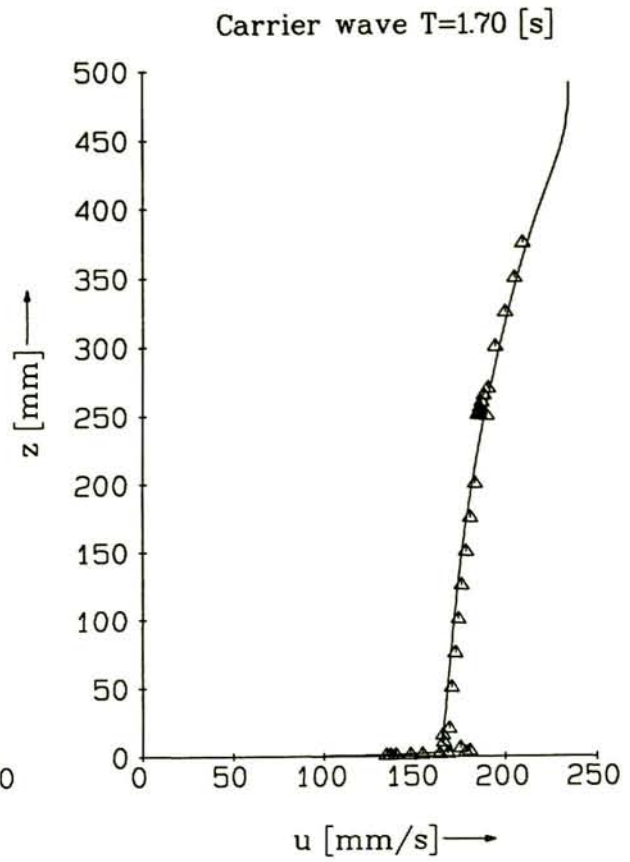
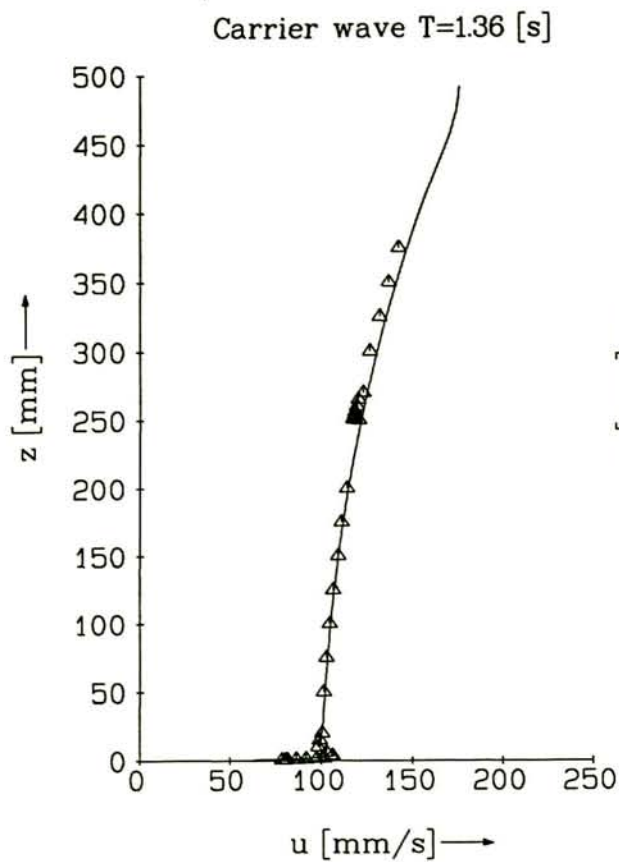
d:\dpm\sedmoc\mono.inv



Wave-current interaction with POINT-SAND model.
 Simulation of monochromatic waves following the current;
 case CMP of (Klopman, 1994). Carrier wave amplitudes.

150 exponentially incr. layers
 k-L turb. mod. with h.p. filter

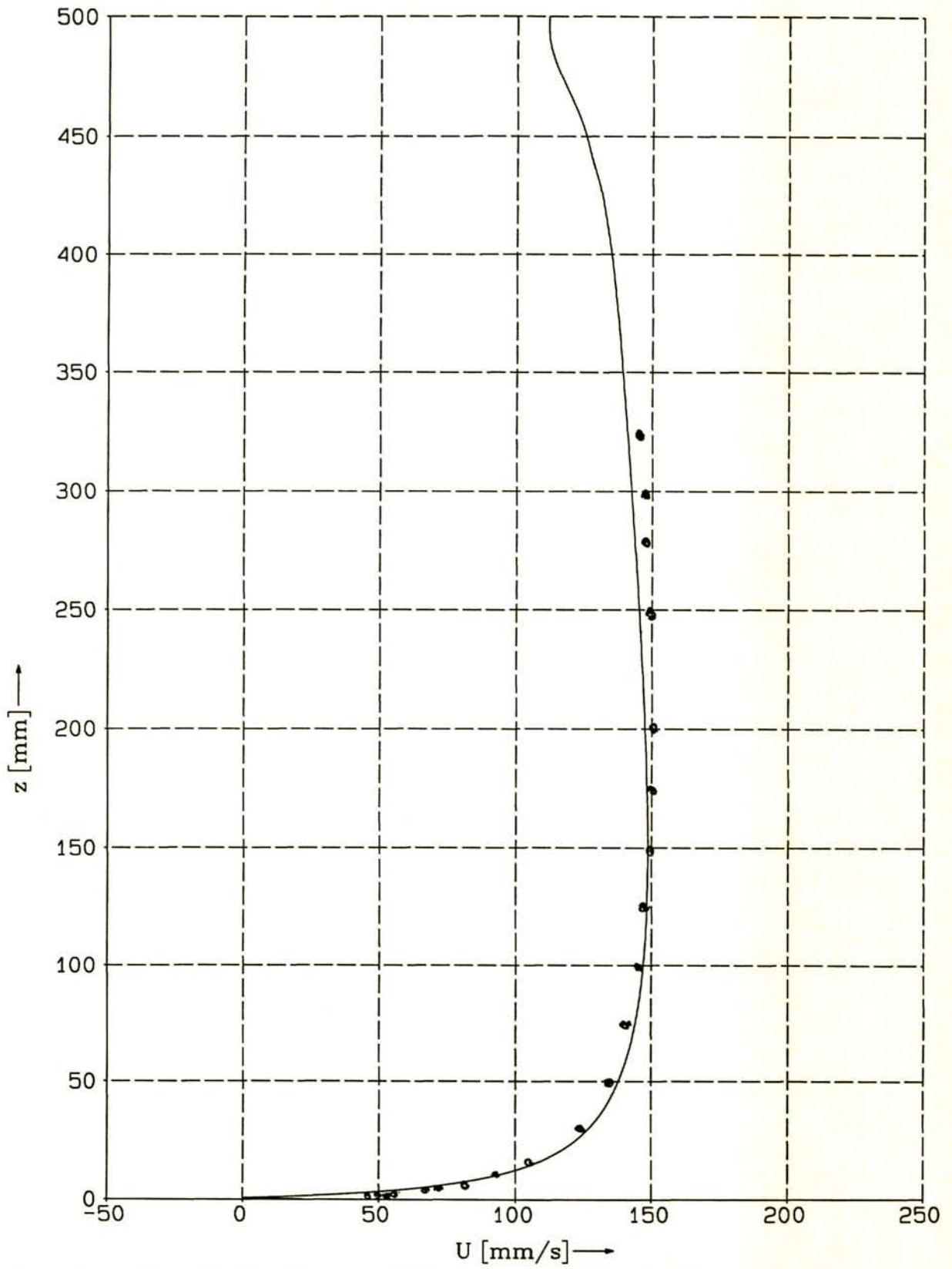
d:\dpm\sedmoc\monampinv



Wave-current interaction with POINT-SAND model.
Simulation of biharmonic waves propagating with a mean current; case CBP of (Klopman, 1994).

150 exponentially incr. layers
k-L turb. mod. with h.p. filter

d:\dpm\sedmoc\bihar.inv



Wave-current interaction with POINT-SAND model;
 random waves following current ; case CIP Klopman (1994).
 500 [mm] water depth; 12 spectral components.

150 double-exponential layers
 0.1 mm bed and top layer

c:\dpm\top\cip.inv

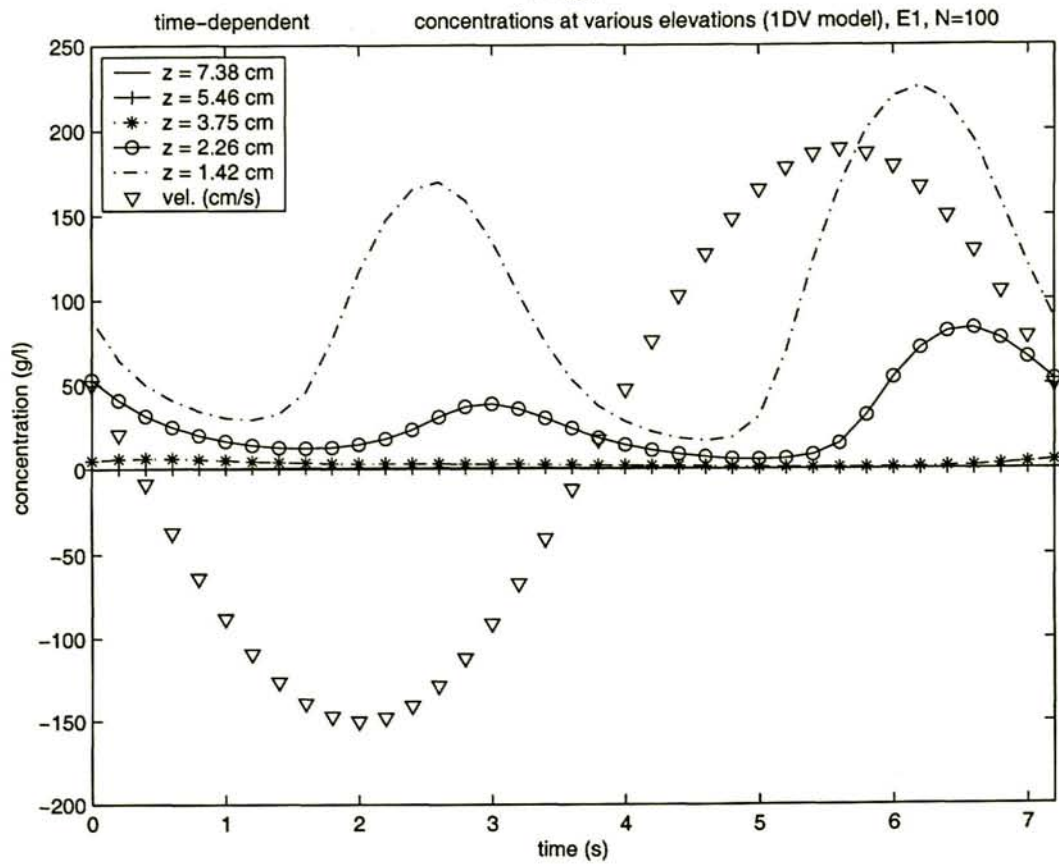
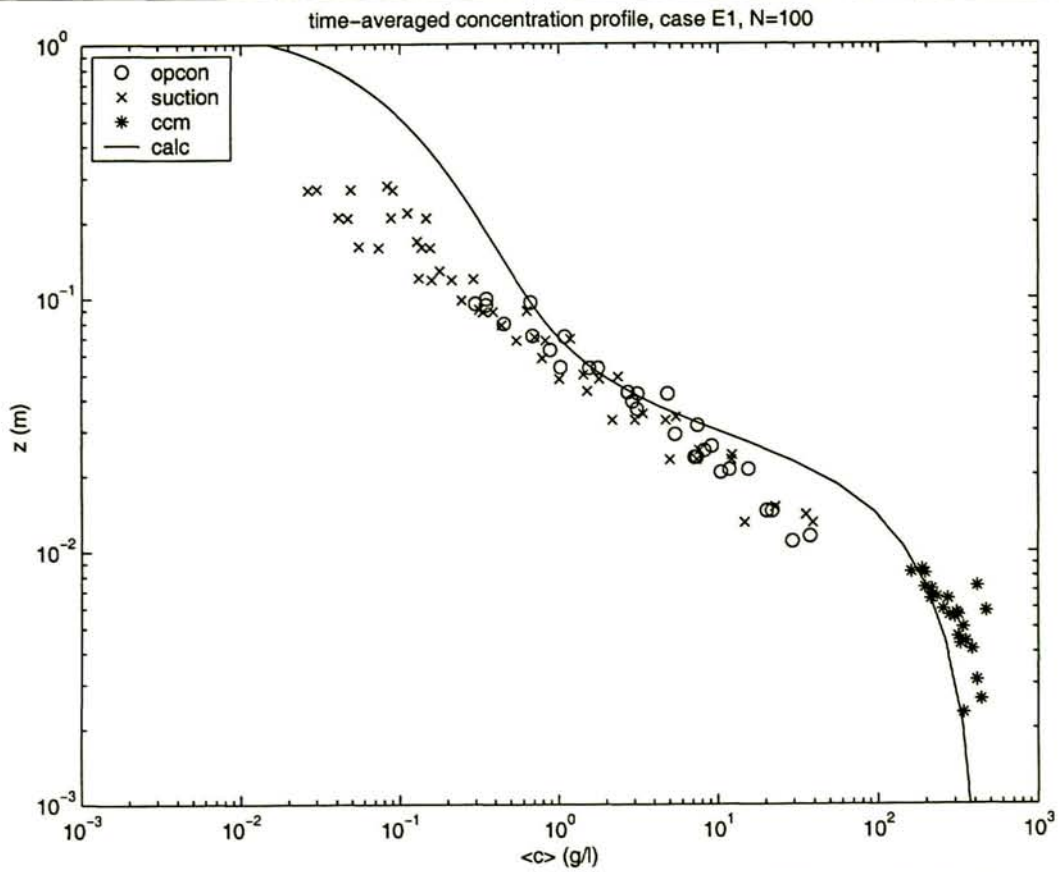


Fig. 10: Time-averaged concentration profile; case E1.

Fig. 11: Time-dependent concentrations at various elevations.

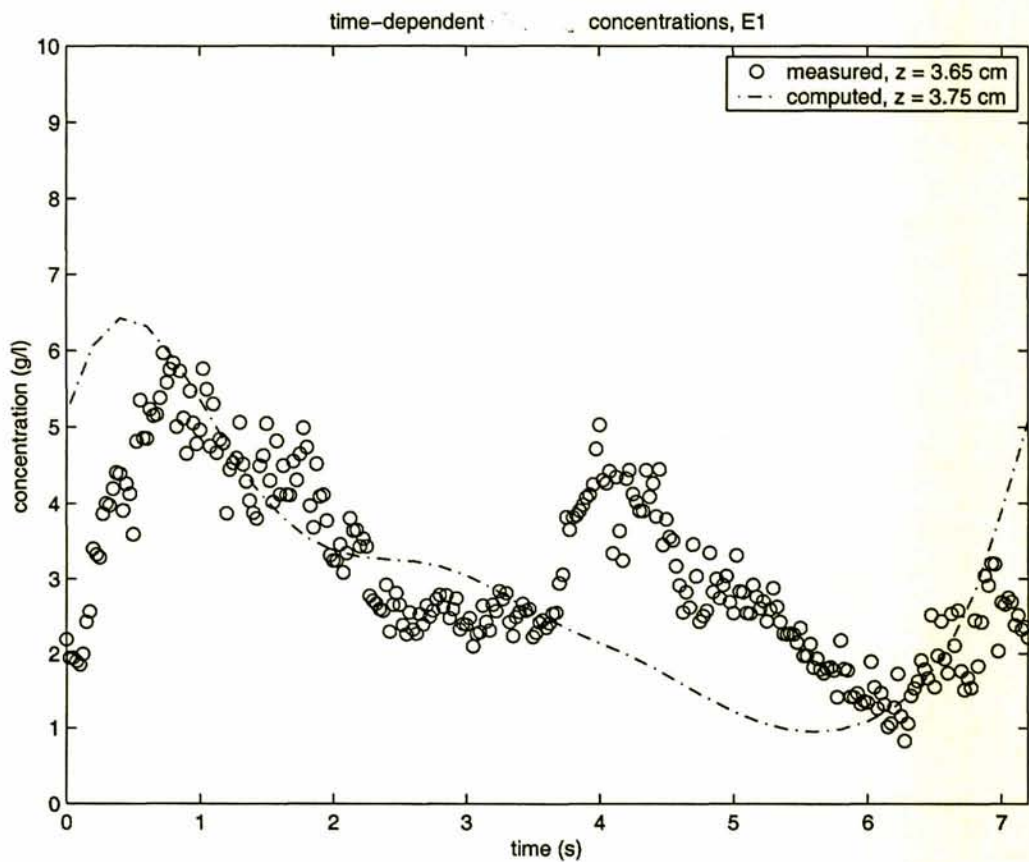
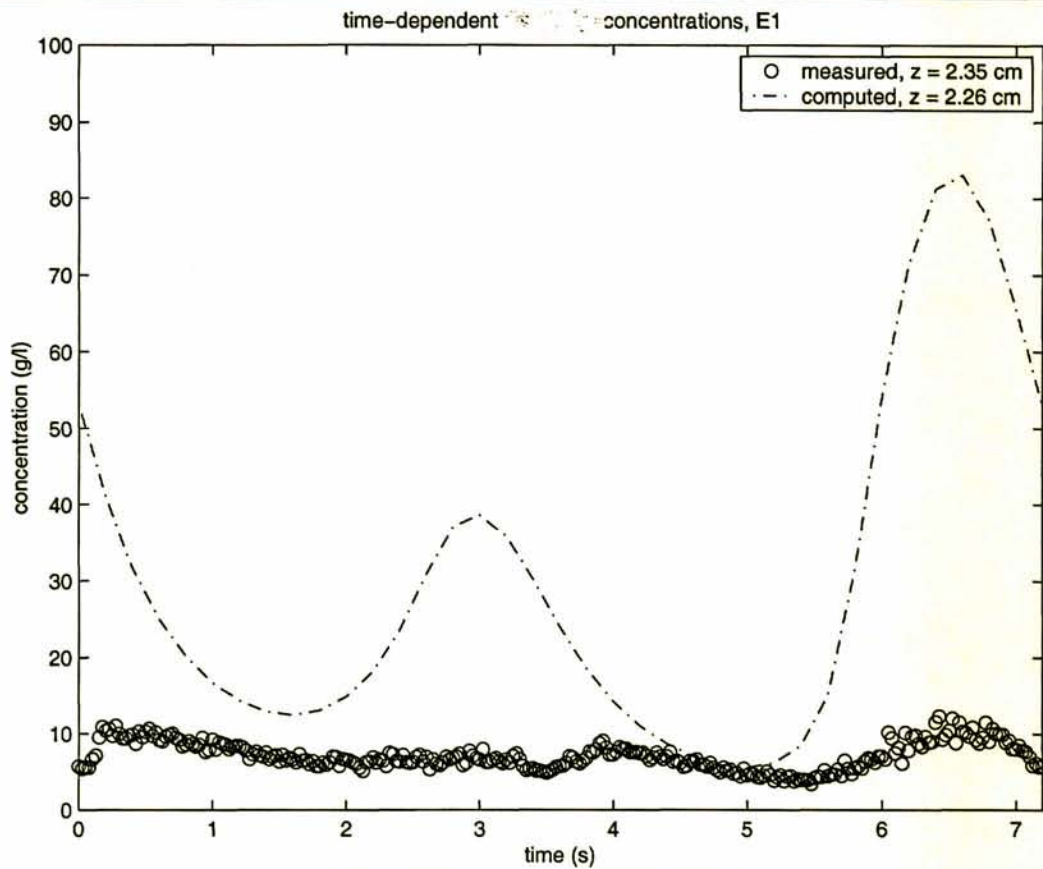


Fig. 12: Time-dependent concentrations, $z = 2.3$ cm case E1
 Fig. 13: Time-dependent concentrations, $z = 3.7$ cm case E1

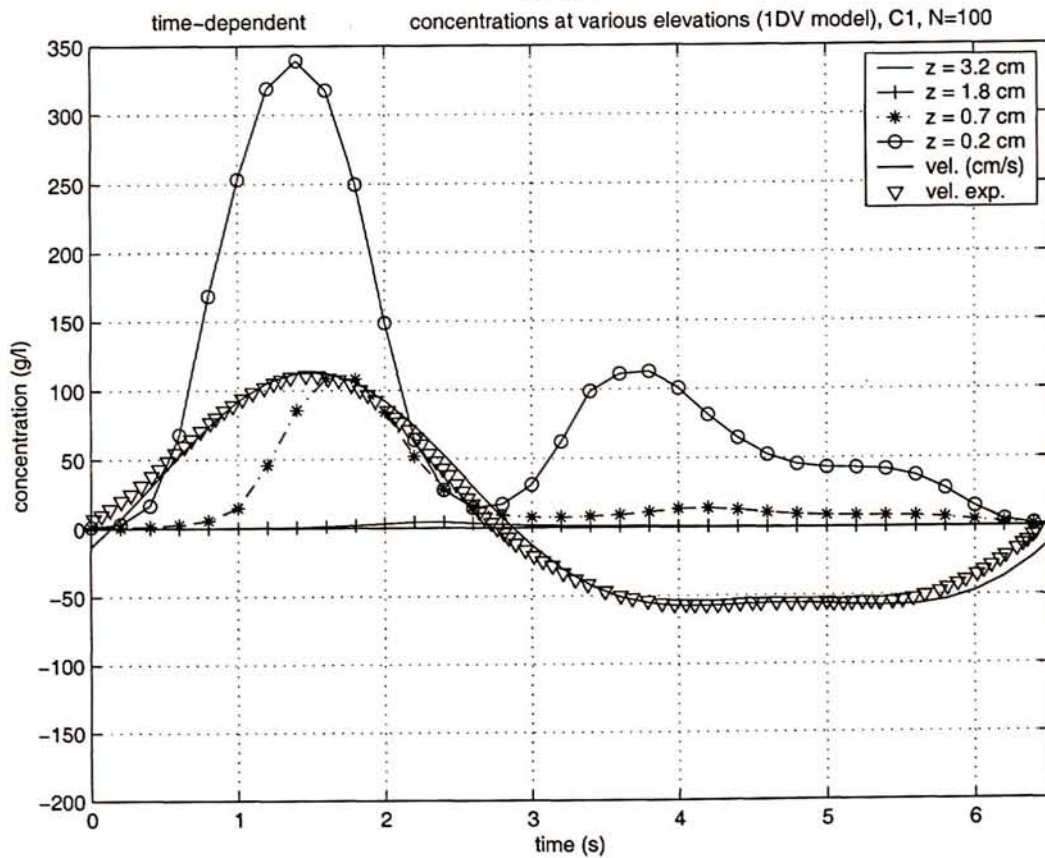
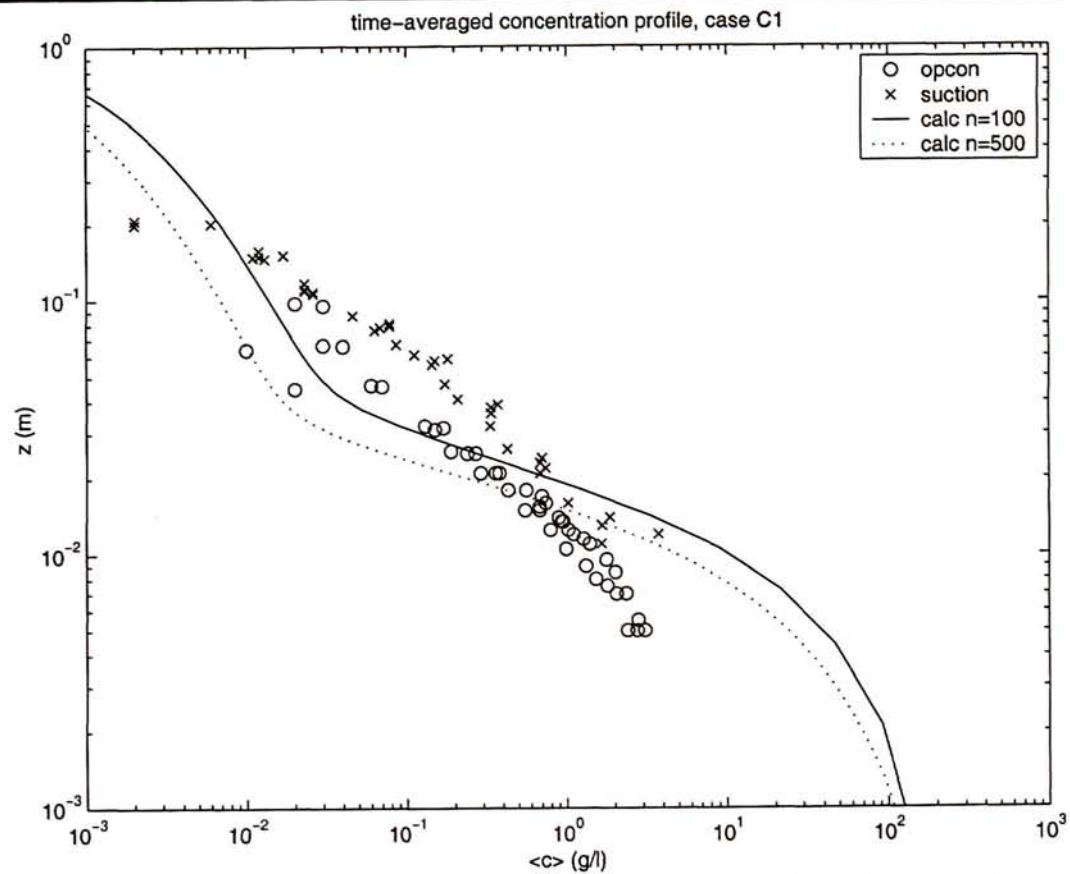


Fig. 14: Time-averaged concentration profile, case C1

Fig. 15: Time-dependent concentrations at various elevations.

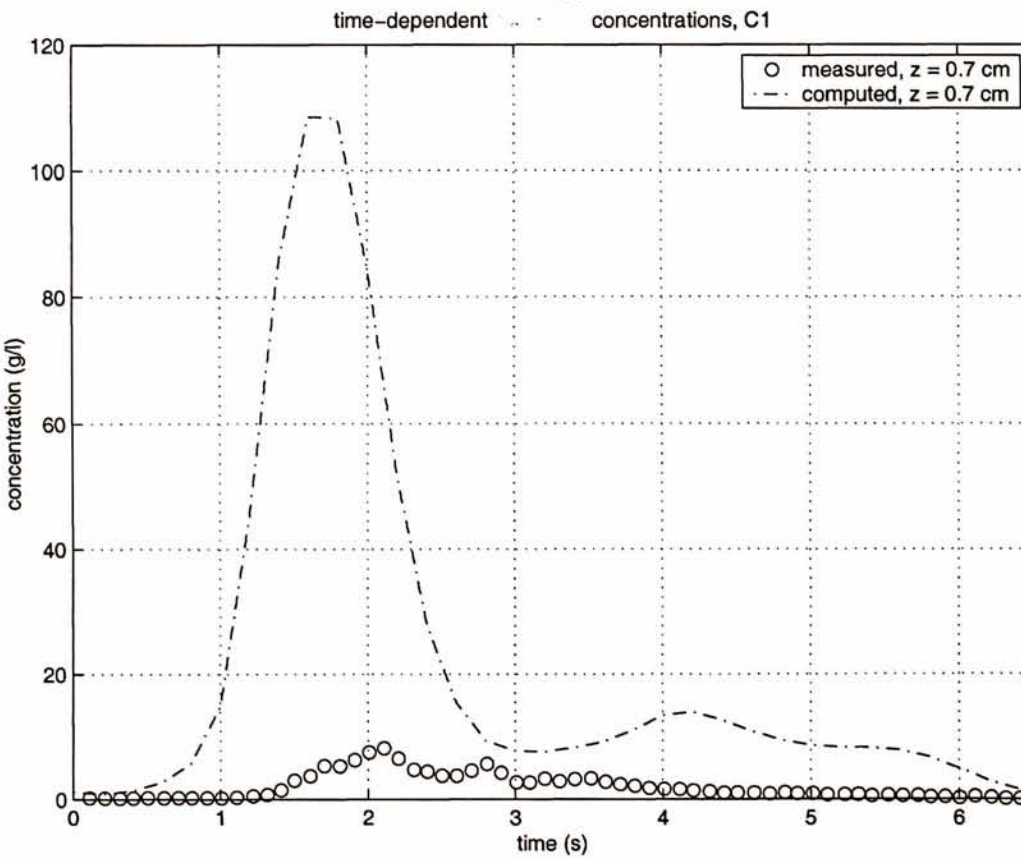
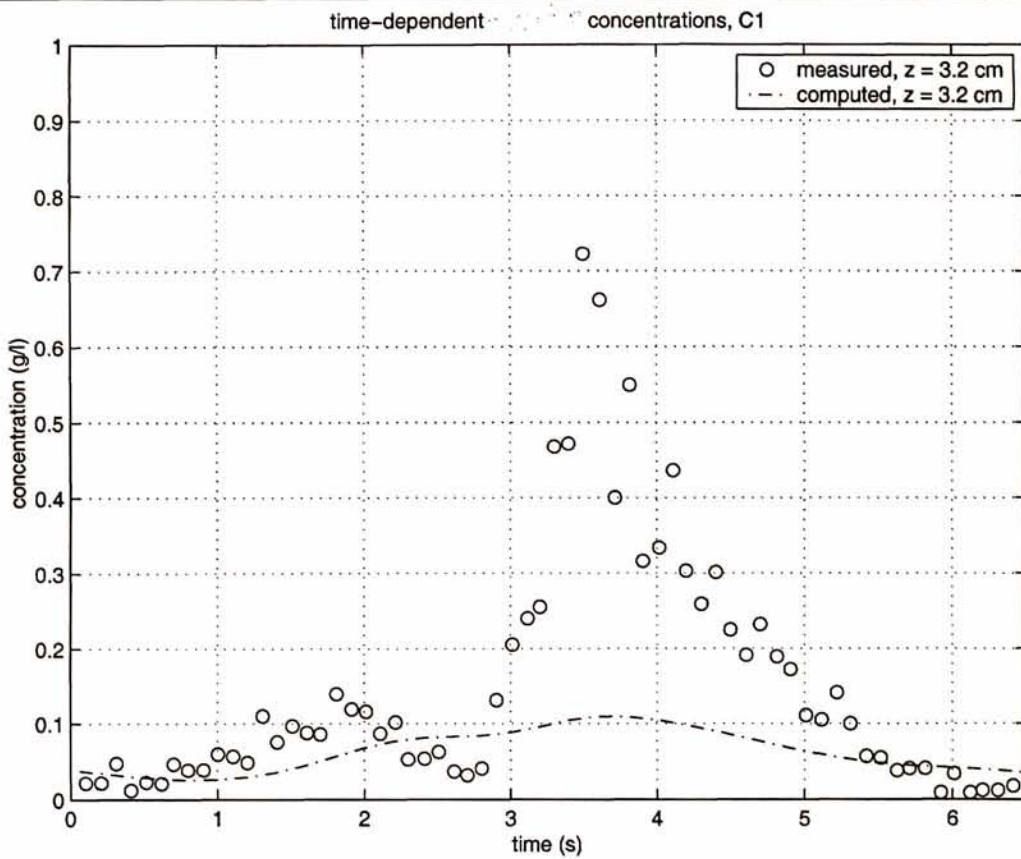


Fig. 16: Time-dependent concentration, z=3.2 cm, case C1

Fig. 17: Time-dependent concentration, z=0.7 cm, case C1

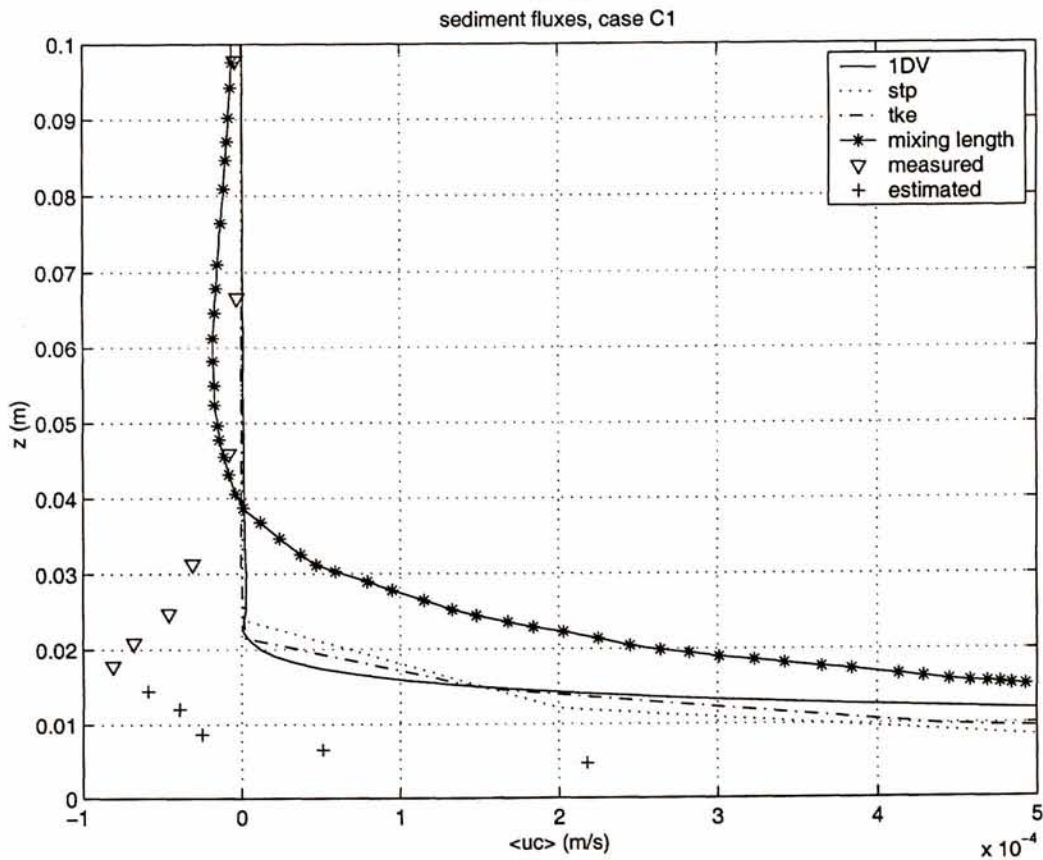
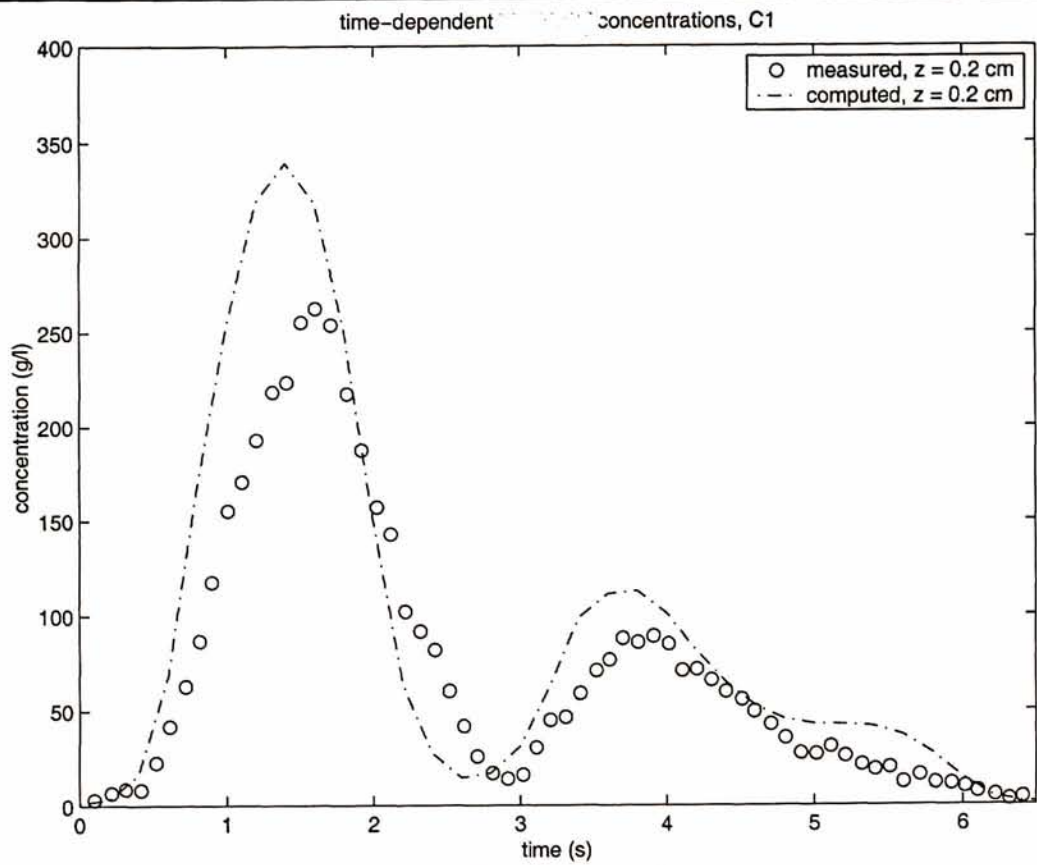


Fig. 18: Time-dependent concentration, $z=0.2$ cm, case C1

Fig. 19: Sediment fluxes, case C1

Appendices

A Overview of solution procedure

The names of the most important subroutines are indicated between brackets [...] and in capitals; the most important variable names are written between (..) and in italics.

Initialise the computation

- Initialise arrays [INIARR];
- Read input file named INDPM.ext0 with extension "ext0" [INPUT];
- Initialise mean flow and turbulence according to log profile [INIT];
- The input file allows for solving one or two mean-flow momentum equations, choose between Directional Point Model (DPM), possibly with Coriolis force included, or one-dimensional model (1DV) e.g. for wave-tunnel experiments ;
- The input file refers to other input files with harmonic components or time series for variable water level and depth-averaged mean flow to be solved by the mean-flow momentum equations. The latter also includes the definition of wave-tunnel oscillatory flow superimposed on mean flow;
- The input file refers to a file with harmonic components (angular frequency, phase and surface amplitude) of orbital motions to be simulated as well as other harmonic components for harmonic analysis only such as subharmonics;
- The input file defines the time step (*timest*) for solving the mean momentum equations;
- The input file defines the relaxation time step (*reltim*) for control over depth-averaged mean flow velocity, *reltim* serves as response time to following the prescribed depth-averaged flow and WCI forcing;
- The input file defines the number (*numwav*) of orbital time step per time step (*timest*) of the mean flow;
- If *numwav*=0 then just the mean flow equations are solved e.g. for simulating wave tunnel experiments or tidal flow only;
- The input file allows for selection of the k- ϵ or k-L turbulence models (*kep* or *k-l*) or just laminar (*lam*) flow. In case of sediment, salt or temperature transport, buoyancy effects are included in the turbulence models;
- The bed friction is by Chezy, Manning or bed roughness (note z_0 not k_s);
- The input file allows for the definition of various sediment fractions (*sand* or *floc*), the type of boundary condition for sand transport (*pickup* or *bedcon*) as well as initial concentration profiles.
- For the time being, the output is limited to just two sediment fractions;
- The output file OUTDPM.ext0 contains a copy of input as understood by the code (please check).

- ◇ **Start outer loop for solving mean-flow momentum equations with time step $\Delta t^{(\text{mean})}$.**
 - ◇ Define depth-averaged mean flow vector [UPDTS or UPFOU];
 - ◇ Define wind vector [UPWIN];
 - ◇ Solve mean-flow momentum equations [UVMOM] depending on vector sum of WCI forces, Stokes drift and low-pass filtered eddy viscosity;
 - ◇ Solve wave numbers and amplitude profile of hydrodynamic pressure for all wave frequencies for the given mean flow [SOLVEP], note that if mean flow oscillates then wave numbers respond accordingly;
 - ◇ **Start inner loop for solving all orbital momentum equations with time step $\Delta t^{(\text{orbit})}$**
 - ◇ Time step $\Delta t^{(\text{orbit})}$ is an integer fraction (*numwav*) of $\Delta t^{(\text{mean})}$ (*timest*) of solving mean-flow equations;
 - ◇ **Start frequency loop per frequency $f^{(n)}$ with time step $\Delta t^{(\text{orbit})}$:**
 - ◇ Start with longest wave which usually has most energy and prescribe water surface elevation of spectral component [DEFWAV];
 - ◇ Project z-dependent mean-flow vector on direction of wave propagation [PROJEC];
 - ◇ Update sum of orbital velocities and project it on direction of wave propagation $\underline{k}^{(n)}$ [PROJEC];
 - ◇ Compute time dependent pressure [SOLVEP] with amplitude profile defined outside loop;
 - ◇ Define high-pass filtered eddy viscosity [TURCLO];
 - ◇ Solve orbital momentum equation for $\underline{u}^{(n)}$ in direction of wave propagation [WWAV;UWAV];
 - ◇ Compute double-contracted strain rate $d_{ij}d_{ij}$ induced by $\underline{u}^{(n)}$ [INCOMP];
 - ◇ Add frequency-weighted strain rates $f_{hp}d_{ij}d_{ij}$ for turbulence production [ALLDIJ];
 - ◇ Add contribution to vertical orbital velocity w_{inc} according to incompressibility [INCOMP];
 - ◇ Stop averaging operation at every second zero crossing of free-surface elevation and
 - ◇ compute Stokes drift and WCI force in direction of wave propagation [AVERAG];
 - ◇ **End frequency loop**
 - ◇ Define fall velocity [FALLVE] for sand, hindered settling included;
 - ◇ Low-pass filter bed friction for mean flow [USTAR];
 - ◇ Harmonic analysis of velocity, TKE, eddy viscosity, sediment concentration and horizontal sediment transport [ORBIT];
 - ◇ Define total density by salt, temperature and sediment [DENS];
 - ◇ Solve turbulence model [TRATUR (k- ϵ); KLMOD] including buoyancy;
 - ◇ Define fall velocity [FALLVE] for sand, hindered settling included;
 - ◇ Define bed condition for sand transport [REFCON];
 - ◇ Solve sediment transport with advection and mixing due to all orbital motions [SEDWAV 1st upwind], built-in options are [SEDCEN central advection] and [DIFUID 3rd order upwind ADI];
 - ◇ **End inner loop**
 - ◇ Apply vector summation of all frequency-dependent WCI forces and Stokes drift;
 - ◇ **End outer loop**
 - ◇ Summarize all temporary output files [OUTMAP] and write to OUTDPM.ext0;
 - ◇ Write results of harmonic analysis [SPCTRL] to OUTSPC.ext0.
 - ◇ **End simulation**

B Direction of orbital velocity and wave number vectors

Consider a mean flow $U(z)$ in x-direction and possible with a vertical profile; this flow is without friction, viscosity and turbulence. Superimposed on this flow are infinitesimal waves propagating with horizontal wave number $\underline{k}=(k, \ell)$ and we define the orbital velocity as

$$\underline{\tilde{u}} = \underline{\hat{u}}(z) \exp[i(kx + \ell y) - i\omega t] \quad (\text{B.1})$$

with angular frequency ω . In this appendix we investigate under what conditions and how much the direction of the velocity amplitude $\underline{\hat{u}}(z)$ deviates from the wave number direction \underline{k} . Consider therefore the two horizontal momentum equations for these waves:

$$\frac{\partial \tilde{u}}{\partial t} + U \frac{\partial \tilde{u}}{\partial x} + \tilde{w} \frac{dU}{dz} + \frac{\partial \tilde{p}}{\partial x} = 0 \quad (\text{B.2a})$$

$$\frac{\partial \tilde{v}}{\partial t} + U \frac{\partial \tilde{v}}{\partial x} + \frac{\partial \tilde{p}}{\partial y} = 0 \quad (\text{B.2b})$$

The direction of $\underline{\hat{u}}(z)$ is obtained by eliminating the pressure from (B.2) and this proceeds by using (B.1) also for the wave-induced pressure. Equation (B.2a) then yields

$$-ik\hat{p} = i(kU - \omega)\hat{u} + \hat{w} \frac{dU}{dz} \quad (\text{B.3a})$$

Likewise, (B.2b) is converted into

$$-i\ell\hat{p} = i(kU - \omega)\hat{v} \quad (\text{B.3b})$$

Multiplication of (B.3a) with (ik) and (B.3b) with $(i\ell)$ and adding the two equations provides

$$(k^2 + \ell^2)\hat{p} = i(kU - \omega)(ik\hat{u} + i\ell\hat{v}) + ik\hat{w} \frac{dU}{dz} \quad (\text{B.4})$$

From incompressibility follows

$$ik\hat{u} + i\ell\hat{v} + \frac{d\hat{w}}{dz} = 0 \quad (\text{B.5})$$

and substitution of this relation in (B.4) yields:

$$\hat{p} = -\frac{i(kU - \omega)}{k^2 + \ell^2} \frac{d\hat{w}}{dz} + \frac{ik\hat{w}}{k^2 + \ell^2} \frac{dU}{dz} \quad (\text{B.6})$$

This expression for the pressure amplitude is substituted into (B.3) and provides the desired relations from which follows the direction of the velocity amplitude.

$$i(k^2 + \ell^2)\hat{u} = -k \frac{d\hat{w}}{dz} + \frac{\ell^2\hat{w}}{\omega - kU} \frac{dU}{dz} \quad (\text{B.7a})$$

$$i(k^2 + \ell^2)\hat{v} = -\ell \frac{d\hat{w}}{dz} - \frac{k\ell\hat{w}}{\omega - kU} \frac{dU}{dz} \quad (\text{B.7b})$$

The last terms in (A7a+b) is responsible for the deviation between the direction of the horizontal vector of the wave velocity amplitude $\hat{u}(z)$ and the wave number \underline{k} . For waves perpendicular to the mean flow $k=0$ holds and then

$$i\hat{u} = \frac{\hat{w}}{\omega} \frac{dU}{dz} \quad ; \quad i\hat{v} = -\frac{1}{|\underline{k}|} \frac{d\hat{w}}{dz}$$

Consequently, the angle difference between horizontal wave velocity vector and wave number vector follows from

$$\frac{\hat{u}}{\hat{v}} = \frac{|\underline{k}|}{\omega} \frac{\hat{w}}{d\hat{w}/dz} \frac{dU}{dz} \approx \frac{\tanh(|\underline{k}|z)}{\omega} \frac{dU}{dz} \quad (\text{B.8})$$

where in the last approximation the potential theory solution $\hat{w} \propto \sinh(|\underline{k}z|)$ for infinitesimal waves without shear is implemented. We estimate this angle difference due to a logarithmic velocity profile with

$$\frac{dU}{dz} = \frac{u_*}{\kappa z}$$

This ratio is large near the bed and there we can approximate $\tanh(|\underline{k}|z) \approx |\underline{k}|z$ whence

$$\frac{\hat{u}}{\hat{v}} \approx \frac{\tanh(|\underline{k}|z)}{\omega} \frac{dU}{dz} \approx \frac{|\underline{k}|u_*}{\kappa\omega} \quad (\text{B.9})$$

The angle is thus proportional to the ratio between bed shear velocity u_* and the wave's celerity and this ratio is negligible because u_* is a small fraction, typically 1/10, of the mean flow and the Froude number for the waves is also significantly less than unity.

More generally, the order-of-magnitude of the ratio between the last terms in (B.7a+b) and the first terms reads:

$$\frac{\text{shear terms}}{\text{without shear}} = O\left\{\frac{1}{c_p - kU/|k|} \frac{\tanh(|k|z)}{|k|} \frac{dU}{dz}\right\} \approx O\left\{\frac{u_*}{c_p - kU/|k|}\right\} ; \quad c_p = \frac{\omega}{|k|} \quad (\text{B.10})$$

and the same order of magnitude appears. The ration (B.10) shows that it becomes significant if the wave's celerity approach the mean flow velocity U and this occurs first for waves propagating with the current. However, then there is no change in wave direction.

We conclude, therefore, that the orbital velocity amplitude $\hat{u}(z)$ is practically parallel with the wave number vector \underline{k} , the deviation being of the order of the ratio between shear stress velocity and the wave's phase speed relative to the mean flow.

C Partial slip condition

In this appendix we present details of the implementation of the partial slip condition for the turbulent flow along a bed in the fully-rough regime. We follow closely (Hinze, 1975) and (Jackson, 1981).

Hinze (1975, p. 636) defines the condition of a fully-rough bed by:

$$\frac{u_* k_s}{\nu} \geq 55 \quad (\text{C.1})$$

with k_s the Nikuradse length scale which is of the order of the geometrical height of the roughness forming elements that create the fluid-bed interface. Note, however, that condition (C.1) is satisfied only for long and high waves or strong currents. The implementation of the transitional roughness regime is recommended.

The essential and very subtle problem is the definition of reference level normal to the bed, here the z -direction, and z is positive away from the bed. Hinze (1975, eq. 7-76) defines the plane $z=0$ as the average of the top levels of the roughness forming elements. Subsequently, Hinze defines the logarithmic profile above a rough bed by

$$\frac{U(z)}{u_*} = \frac{1}{\kappa} \ln \left\{ \frac{u_* (z + k_e)}{\nu} \right\} + B - \frac{\Delta U(z)}{u_*} \quad ; \quad \kappa = 0.41 \quad , \quad B = 4.9 \quad , \quad (\text{C.2})$$

and, based on various observations (Hinze, 1975, fig. 7-16), Hinze (1975, eq. 7-76) estimates the apparent origin of the logarithmic velocity profiles at $z=-k_e$ and $k_e=0.25 k_s$. The latter conclusion is substantiated by Jackson (1981) who derives the meaning of this origin and shows for various roughness elements that

$$k_e = 0.3k_s \quad (\text{C.3})$$

holds. In the following, we adopt (C.3).

For $\Delta U=0$, the formulation (C.2) is equivalent to the turbulent layer flow along a hydraulically smooth wall but with the origin $0.3k_s$ below the mean top levels of the fluid-bed interface. For a rough bed, there occurs a velocity shift ΔU and Hinze (1975, p. 637) concludes from his figure 7-16:

$$\frac{\Delta U(z)}{u_*} = \frac{1}{\kappa} \ln \left\{ \frac{u_* k_e}{\nu} \right\} + C \quad ; \quad C \approx -0.4 \quad , \quad (\text{C.4})$$

where C is given an average value for various type of roughness elements. Combining (C.2), (C.3) and (C.4) yields

$$\frac{U(z)}{u_*} = \frac{1}{\kappa} \ln \left\{ 8.78 + \frac{29.3z}{k_s} \right\} ; \quad \kappa = 0.41 \tag{C.5}$$

Given the customary relation $z_0=k_s/30$ between roughness length scale z_0 and geometrical scale k_s as well as the uncertainty range in the various parameters (κ , B and C), we simplify (C.5) as:

$$\frac{U(z)}{u_*} = \frac{1}{\kappa} \ln \left\{ \frac{9z_0 + z}{z_0} \right\} . \tag{C.6}$$

We apply formulation (C.6) in conjunction with the precise definition of the plane $z=0$. It is this plane $z=0$ that equals the bottom of the first computational grid box above the bed. We believe the concept (C.6) should be followed strictly. For instance when using the mean shear rate at the level $z=0$ of the bed-grid box:

$$\left. \frac{\partial U}{\partial z} \right|_{z=0} = \frac{u_*}{9\kappa z_0} . \tag{C.7}$$

The equally strict consequence of (C.7) is that the eddy viscosity at the bed level $z=0$ follows from the definition u_*^2 i.e.

$$u_*^2 = \left\{ \nu_T(z) \frac{\partial U}{\partial z} \right\} \Big|_{z=0} : \quad \nu_T(z=0) = 9\kappa u_* z_0 \tag{C.8}$$

Note that in the first expression of (C.8) the kinematic viscosity is excluded in accordance with the hydraulically rough regime (C.1) for which (C.6) has been derived. On the other hand, if the kinematic were included in (C.8) it would be negligible provided (C.1) is satisfied but this not always the actual application of the previous formulation. Therefore, we exclude the kinematic viscosity in (C.8).

The bed boundary conditions for the k-L as well as k-ε model should match the eddy viscosity defined by (C.8) and at $z=0$.

In our k-L model the closure for eddy viscosity reads:

$$\nu_T(z) = c'_\mu L(z) \sqrt{k(z)} \tag{C.8}$$

and at the bed we define the Turbulent Kinetic Energy by:

$$k(z=0) = \left(\frac{u_*}{c'_\mu} \right)^2 \tag{C.9}$$

Consequently, given (C.8), the mixing length scale must be defined as:

$$L(z=0) = 9\kappa z_0 \quad (\text{C.10})$$

This completes the boundary conditions for the k-L model. The Bakmetev length scale profile is then defined with $z=-9z_0$ as virtual origin for $L(z)$.

Next we continue with the appropriate bed boundary conditions for the k- ε model. Near the bed under high-Reynolds turbulence conditions and a logarithmic boundary layer must hold:

$$\varepsilon = \nu_T \left(\frac{\partial U}{\partial z} \right)^2 \equiv \frac{u_*^3}{\kappa(z + 9z_0)} \quad (\text{C.11})$$

D Description of program in- and output

As an illustration, the format of the input and output files is discussed using the C1-case of the wave tunnel calculations. Only the input files are listed, as the length of the output files is too large. Instead, the output files are schematically discussed.

The main input file is the file `indpm.id`, where `id` stands for the identification string of the calculation (i.e. `c1` in our case). The input of this file is typeset in `Courier`, whereas the explanation is typeset in `Times`.

```
*****General          input*****
1DV          DIMENS: choose 1DV or DPM
```

If 1DV is chosen, only one velocity component is solved. If DPM (directional point model) is chosen, two velocity components (u and v) are solved. In the β -release distributed with this report, the DPM-variant does not work properly with the sediment subroutines.

```
0.0          FCORIO: Coriolis parameter
Coriolis parameter (0 in the wave tunnel and flume experiments, 1 in the field)
```

```
0.          DP      : depth
Depth of the water column below the  $\zeta$  (zeta) = 0 plane. For the present calculations the plane  $\zeta = 0$  is defined at the bottom of the wave tunnel, therefore DP = 0.
```

```
0.0          ZETA   : water-level (or)
          FILTSZ: file time series ZETA (or)
tun_c1.lv1   FILFOZ: file fourier comp. ZETA (or)
Surface elevation, in the current case specified in fourier components in the file tun_c1.lv1. The value of ZETA in the first line is neglected if a file is specified in the second or third line.
```

```
0.0          UMEAN  : West-to-East depth-averaged velocity (or)
          FILTSU: file time series UMEAN (or)
tun_c1.vel   FILFOU: file fourier comp. UMEAN (or)
Horizontal velocity, in the current case specified in fourier components in the file tun_c1.vel. The value of UMEAN in the first line is neglected if a file is specified in the second or third line. Note that the depth-averaged velocity is specified, not the velocity at a certain level.
```

```
sec          TUNIT  : time unit (SEC/MIN)
Chose time unit: seconds or minutes.
```

```
0.05         TIMEST: time step (in TUNIT)
15600        NUMTIM: number of timestep simulation
0            NUMWAV: number of timestep orbital motion per TIMEST
In order to solve orbital motions accurately at a large time step (compared with the wave period), the orbital motion can be solved using a smaller time step, being the wave period divided by NUMWAV.
```

```
0.05         RELTIM: relaxationtime (in TUNIT)
The relaxation time should not be chosen smaller than the time step!
```

```
65 0.20 78 TIMEWR: STRT-INC-STOP time frame writing output (TUNIT)
The first number is the start time, the second number the time increment and the third number the stop time with regard to writing to the output file.
```

```
1.0          TETA   : par. theta-method(rec. theta =1)
This is a input parameter for the integration method used. It is recommended to set  $\theta$  at 1.
```

```
KEP          MODEL  : choice between LAM (laminar flow) or KEP (k-epsilon turb. model)
Chose turbulence model: lam (laminar flow), k-l or kep (k-epsilon model).
```

```
1e-6         VISCOU: kinematic viscosity [m^2/s]
20           ROUMET: roughness meth. MANN/CHEZ/20
Chose roughness method: Manning, Chézy or  $z_0$ .
```

```

3.2e-5      ROUCOF: roughness height (ROUMET)
1           IRO   : IRO=0: hydr.smooth, IRO=1: hydr.rough

           FLTWIN: file time series (directional) wind and surface waves (or)
0.         DIRWI : direction from which the wind blows
0.         WIND  : wind speed, 10 m above free surface

```

The three lines here are intended for wind-generated waves and are not used in the wave tunnel case.

```

wavspc.cl  FLTSPC: file with directional spectrum of surface waves (or)
0.         DIRWA : direction from which the surface waves come
0.         HSIG  : significant wave height
0.         PERIO : significant wave period
1000.0     RHOM  : reference density
*****Layer      Input*****

```

VARIA LAYDIS: choose EQUIDistant or VARIABLE

If VARIA is selected, the layer distribution is logarithmic with a power specified below; with EQUID a equidistant distribution is selected.

```

500        KMAX  : number of layers

```

Here the number of layers is specified. The maximum is 1000.

```

1.5        ALFA  : >1 power in layer distribution, ALFA ignored for equidistant
layers

```

```

*****Constituent Input*****
0          LMAX  : number of constituents
0          LSAL  : index nr for salinity
0          LTEM  : index nr for temperature
10.0       SALEQS: eq. of state salinity (always input)
5.0        TEMEQS: eq. of state temperature (always input)

```

The constituent input is not used for the wave tunnel calculations.

```

*****Sediment      Input*****
1          LSED  : number of sediment

```

The number of sediment types can be specified here, each to be assigned a name label and sediment properties.

```

sand       SEDTYP(L): type of sediment
0.7        SIGSED(L): prandtl schmidt number
2650       RHOSOL(L): density sediment
0.21e-3    SEDDIA(L): D_50 [m] of sand

```

```

bedcon     EROTYP(L): PICKUP or BEDCON for type of bed condition

```

Two types of bed boundary conditions can be selected: PICKUP or BEDCON.

```

step       SEDDIS  : "step" or "linear"

```

An initial sediment concentration distribution may be applied, either a 'step' or a linear distribution.

```

0.0        SEDTOP(L): sediment concentration above step
0.0        SEDBED(L): sediment concentration below step
100        KSTEP   : k-value of sediment step position
*****End      Input*****

```

The files to which is referred in the input file indpm.cl are: tun_cl.lvl, tunc1.vel and wavspc.cl. These are discussed below.

tun_cl.lvl

```

2          01      K1      nfc [number of harmonic component]

```

Specify number of harmonic components and their label.

```

199385    398769    frequency(n=2:nfc) [degrees/hour] must equal those in zeta-
file

```

Specify frequencies in degrees per hour!

```

1.1       0.0      0.0      ampl (n=1:nfc) [m]

```

The first number is the constant component of the water level, i.e. the height of the wave tunnel section (1.1 m).

```

0.0       0.0      phase (n=1:nfc)

```

tunc1.vel

```

2      1          nfc ; ksec
Specify number of harmonic components and number of velocity components to be weighed.
1.0          weight (k=1:ksec)
Specify the time unit (k=1: ksec).
199385      398769      frequency (n=2:nfc) [degrees/hour] must equal those in zeta-
file
Specify frequencies in degrees per hour!
0.042      0.844      0.265      U_ampl (k=1;n=1:nfc)
Specify the velocity amplitudes in m/s; the first number is the constant component.
          0.0          0.0          U-phase (k=1;n=1:nfc)
0.000      0.000      0.0          V_ampl (k=1;n=1:nfc)
          0.0          0.0          V-phase (k=1;n=1:nfc)

```

wavespc.cl:

```

0      NSPC : number of spectral components for solving orbital motions
With this parameter the number of spectral components for solving orbital motions can be specified,
i.e. the spectrum of  $\zeta$  (surface elevation). For the wave tunnel case NSPC is set at 0. If flume
experiments with surface waves are to be modelled, NSPC should be given a value equal to or larger
than one.
3      NSPCAD: in addition to NSPC other spectral components for harmonic analysis
only
** remark: if NSPC > 1, specify here nr. of spectral component; angular freq.;
** amplitude; phase; direction from which the waves come
** Additional spectral components for harmonic analysis only, angular frequency is
essential:
1 0.0          0.0          0.0          0.
2 0.96665      0.0          0.0          0.
3 1.93329      0.0          0.0          0.
nr.;angular freq.;amplitude;phase;direction from which the waves come; number of
spectral components

```

Description of output files

Results are written to two output files: outdpm.id and outspc.id, where id stands for the identification string of the calculation (i.e. cl in the case described here). The file outdpm.id first lists the values of the input parameters as specified in the input files, including the specified layer thickness and the initial sediment concentration distribution. Subsequently, the following information is written:

At each time step specified for output three tables are displayed. The first table consists of 8 columns listing for each layer:

1. z-coordinate layer interface
2. turbulent energy
3. turbulent dissipation
4. eddy viscosity
5. du/dz
6. dv/dz
7. dp/dz
8. Richardson number

The second table consists of 6 columns listing for each layer:

1. z -coordinate concentration point
2. u -velocity
3. v -velocity
4. uv -magnitude
5. uv -direction
6. density

The third table consists of 2 (or 3 if two types of sediment have been specified: the current program supports 2 sediment types) columns listing for each layer:

1. z -coordinate
2. sediment concentration

After the last time step, three tables are displayed containing the same information as the tables specified above, but each of them containing information for all time steps. In one additional column (the first one) the time information is displayed.

The last table in the file outdpm.id contains 12 columns (or more if more than one type of sediment has been specified) displaying for each time step specified for output the following parameters:

1. time (seconds)
2. depth value
3. free surface
4. depth-averaged u -velocity
5. calculated depth-averaged velocity
6. difference UREAL-UMEAN for depth-averaged velocity
7. depth-averaged v -velocity
8. calculated depth-averaged velocity
9. difference VREAL-VMEAN for depth-averaged velocity
10. Shields parameter sediment fraction 1
11. critical Shields parameter sediment fraction 1
12. prescribed bed conc. sediment fraction 1

The file `outspc.id` contains the following information:

- the period of each spectral component;
- tables for the parameters *tkc* (turbulent kinetic energy), *vicw* (eddy viscosity), *uw*, *utot*, *vtot*, *fWCI* (force wave current interaction), *sedi* (sediment concentration fraction *i*), *uc_i* and *vc_i* containing 7 columns:
 1. z-coordinate *w*-point
 2. amplitude component NF= 1
 3. phase component NF= 1
 4. amplitude component NF= 2
 5. phase component NF= 2
 6. amplitude component NF= 3
 7. phase component NF= 3

In this example 3 components are specified, of which the first is the steady flow component.

E Built-in test case

Introduction

The well-established concept of Prandtl's mixing length in a high-Reynolds stationary boundary layer flow along a rough plane wall invokes that sufficiently near the wall for the eddy viscosity $\nu_T = \kappa u_* z$ holds with the origin at some level αz_0 below the fluid-bed interface, see Appendix C. It is well known that then the velocity profile becomes logarithmic and the concentration profile proportional to z^β . Here, β is the so-called Rouse parameter and $\beta = w_s \sigma_T / \kappa u_*$ holds with settling velocity w_s , and σ_T is the turbulence Prandtl/Schmidt number. The latter being the ratio between eddy viscosity and eddy diffusivity.

The consequence of Prandtl's classical but well-established law is that both the mean velocity profile as well as the mean sand concentration profile are *nearly singular*. The strict reader is asked for some tolerance in the latter mathematically poor but intuitively clear definition.

In a steady current along a horizontal bed, the horizontal sand flux profile is the product of the *nearly singular* mean velocity and *nearly singular* mean sand concentration profiles. The latter product thus suggests that the numerical solution of the horizontal sand flux is overly sensitive to numerical errors.

Consequently there is a need for comparing the POINT-SAND model against analytic solutions. These are presented in this appendix. The results are implemented in a subroutine in the POINT-SAND model. When the user runs the code with *log* as extension to the standard input file *indpm.** then in the code the density coupling between sediment and turbulence (buoyancy flux) is switched off. Further, the simulation results are appropriately scaled by subroutine *tstlog* and then written to the output file *tstdpm.log*. All other formulations for settling velocity, bed concentration, turbulence closures etc. remain the same as for general use.

The new output file *tstdpm.log* also contains the analytic solutions, using the same scaling for making a detailed one-to-one comparison through e.g. plots. The great advantage for the user is that he can check his expertise of correctly setting numerical control parameters such as layer distribution, number of time steps, time step etc. Further, after any correction to the code, at least this test case should yield the proper results.

The analytic solutions are based on the frequently observed logarithmic velocity profile in stationary high-Reynolds number channel flows. For a constant pressure gradient normal to the bed, the eddy viscosity profile then should be parabolic. With significantly more scatter such a parabolic profile is indeed derived from the observable mean velocity gradient divided by the observed Reynolds shear stress, see e.g. (Nezu and Rodi, 1986).

In this appendix we shall assume this seemingly one-to-one connection between logarithmic velocity profile and parabolic eddy viscosity profile. It should be remembered, however, that this is a convenient algebraic relation rather than an experimentally proven fact.

This appendix presents the analytic solution for the depth-integrated sand flux due to a logarithmic velocity and the Rouse concentration profile derived from the parabolic eddy viscosity/diffusivity. Based on these solutions, we present a sensitivity analysis. Much

attention is paid to the proper definition of the origin of the logarithmic velocity profile over a hydraulically rough bed and the precise expressions for eddy diffusivity as well as for the concentration profile.

In the subsequent analysis, the following five length scales play a role:

1. d_{50} the grain size diameter of 50% sieve passage;
2. z_a , usually $2d_{50}$, the level above the fluid-bed interface where the concentration of suspended sediment is prescribed by some empirical formula depending on e.g. bed shear stress;
3. z_0 the hydraulic roughness length scale of a plane granular bed, usually one-order of magnitude smaller than the d_{50} of the grains in the bed;
4. αz_0 the position of the origin of the logarithmic velocity profile below the bed-fluid interface;
5. h the water depth, measured between free surface and the bed-fluid interface.

The z -axis is vertically upwards and the level of fluid-bed interface is defined at $z=\alpha z_0$. The integrals appearing in the following text have marginal corrections to exact solutions. The latter, however, are valid for the Rouse parameter $\beta < 1$. Note that this limitation of our analysis does not imply that $\beta > 1$ is physically impossible. The dedicated output file *tstdpm.log* reports the following depth-integrated sand fluxes:

1. numerical integration, along the entire water depth, of the product between the computed horizontal velocity and the computed concentration;
2. numerical integration, along the entire water depth, of the product between the analytic logarithmic velocity and the analytic Rouse profile both based on the computed bed shear stress;
3. For $\beta < 1$ also the analytic solution to the previous integral based on the analytic solutions for velocity and concentration and based on the theoretical bed-shear stress.

Obviously the most reliable comparison is made with the third option but then $\beta < 1$ must hold.

E.1 Logarithmic velocity profile

The logarithmic velocity profile for a high-Reynolds number flow over a hydraulically rough but plane bed is defined as

$$\alpha z_0 \quad ; \quad \alpha \approx 9 \quad (\text{E.1.1})$$

below the top levels of the sand bed, the magnitude of α is estimated in Appendix C. For simplicity of formulation we define the level $z=\alpha z_0$ as the origin of the logarithmic function describing the velocity profile which, according to Appendix C, is located just below the tops of the sand grains forming the fluid-bed interface.

The water depth is defined as h i.e. the free surface is at $z=h+\alpha z_0$ and for notational simplicity we define:

$$H=h+\alpha z_0 \quad (\text{E.1.2})$$

With these definitions, the logarithmic velocity profile for a high-Reynolds number flow over a hydraulically rough bed reads:

$$u = \frac{u_*}{\kappa} \left\{ \ln \left(\frac{H}{z_0} \right) + \ln Z \right\} \quad \text{with} \quad Z = \frac{z}{H} \quad , \quad (\text{E.1.3})$$

and $Z = \alpha z_0 / H$ corresponds to the fluid-bed interface with non-zero velocity. The definition of the depth-averaged velocity then reads:

$$\bar{u} = \frac{1}{h} \int_{\alpha z_0}^{h+\alpha z_0} u(z) dz = \frac{u_*}{\kappa} \left\{ \left(1 + \frac{\alpha z_0}{h} \right) \ln \left(1 + \frac{h}{\alpha z_0} \right) - 1 - \frac{\alpha z_0}{h} \ln \alpha \right\} \quad . \quad (\text{E.1.4})$$

It will be convenient to define the following usually very small and positive parameter:

$$\varepsilon = \frac{\alpha z_0}{H} \equiv \frac{\alpha z_0}{h + \alpha z_0} \quad \text{or inversely} \quad \frac{\alpha z_0}{h} = \frac{\varepsilon}{1 - \varepsilon} \quad \text{and} \quad \frac{H}{h} = \frac{1}{1 - \varepsilon} \quad . \quad (\text{E.1.5})$$

Using (E.1.6), the logarithmic velocity profile (E.1.3) then reads:

$$u = \frac{u_*}{\kappa} \left\{ \ln Z + \ln \left(\frac{\alpha}{\varepsilon} \right) \right\} \quad . \quad (\text{E.1.6})$$

Likewise, the depth-averaged velocity:

$$\bar{u} = \frac{u_*}{\kappa(1 - \varepsilon)} \left\{ \ln \left(\frac{\alpha}{\varepsilon} \right) - \varepsilon \ln \left(\frac{\alpha}{\varepsilon} \right) \right\} \quad \text{with} \quad e = \exp(1) \quad .$$

or

$$\bar{u} = \frac{u_*}{\kappa(1 - \varepsilon)} \ln \left\{ \frac{1}{\varepsilon} \left(\frac{\alpha}{e} \right)^{1 - \varepsilon} \right\} \quad \text{with} \quad e = \exp(1) \quad . \quad (\text{E.1.7})$$

Usually, ε is less than (10^{-4}) so that ε in (E.1.7) can be neglected however the ε^{-1} term in the logarithm is retained.

E.2 Eddy-viscosity profile

In agreement with (E.1.3), the eddy viscosity profile is derived here and it should yield the linear profile of Reynolds shear stress R_{xz} for a stationary high-Reynolds flow with hydrostatic pressure distribution and neglecting viscous stresses:

$$R_{xz} = u_*^2 \frac{H - z}{h} \quad . \quad (\text{E.2.1})$$

Note in (2.1), $R_x = u_*^2$ holds at the zero-velocity level $z = \alpha z_0$. The corresponding definition of the eddy viscosity follows from the Boussinesq hypothesis:

$$R_x \equiv \nu_T \frac{\partial u}{\partial z} \quad (\text{E.2.2})$$

and using $Z = z/H$ the corresponding expression for the eddy viscosity reads

$$\nu_T = \kappa u_* \frac{H^2}{h} Z(1-Z) \equiv \kappa u_* H \frac{Z(1-Z)}{1-\varepsilon} \quad (\text{E.2.3})$$

The last expression uses the definition of the small positive parameter ε , see (E.1.6). Note that (E.2.3) yields a non-zero eddy viscosity at the zero-velocity level $Z = \alpha z_0/H$. From the Reynolds analogy, using the turbulence Prandtl/Schmidt number σ_T , the eddy diffusivity Γ_T is related to the eddy viscosity through:

$$\Gamma_T = \frac{\kappa u_* H}{\sigma_T} \frac{Z(1-Z)}{1-\varepsilon} \quad (\text{E.2.4})$$

E.3 The equilibrium concentration profile

For stationary conditions in a channel of uniform dimensions the settling flux due to a constant settling velocity w_s is balanced by upward mixing i.e.

$$\Gamma_T \frac{\partial c}{\partial z} = -w_s c \quad (\text{E.3.1})$$

The solution to (E.3.1) is the well-known Rouse profile for a parabolic eddy diffusivity profile. It is customary that the integration constant appearing in solving (E.3.1) is converted to some given concentration c_a at level z_a above the fluid-bed interface. In the present purpose the so-called Zyserman-Fredsoe formulation for c_a is applied at $z_a = 2d_{50}$ above the fluid-bed interface. In the scaled Z -coordinate the level z_a is defined by

$$\delta = \frac{\alpha z_0 + z_a}{H} = \varepsilon + 2 \frac{d_{50}}{H} \quad (\text{E.3.2})$$

Consequently, the Rouse profile reads:

$$c(z) = c_a \left(\frac{\delta}{1-\delta} \right)^\beta \left(\frac{1-Z}{Z} \right)^\beta, \quad (\text{E.3.3})$$

with c_a given by the empirical Zyserman-Fredsoe formula.

In the following we define that below the level $z=z_a$ no suspended sediment transport occurs but just bed-load transport (by rolling and jumping grains) and the latter is not part of the suspended sand-flux formulation that we seek here.

The difference between ε and δ is very small. Nevertheless in computing depth-averaged concentration and sand flux, we integrate over the physical interval (z_a, h) and divide by the total water depth h . In view of the very small ratio d_{50}/h , we acknowledge the division by h , rather than by $(h-z_a)$, is just a formality.

The so-called Rouse parameter β , appearing in (E.3.3), follows from (E.2.4):

$$\beta = \frac{(1-\varepsilon)w_s \sigma_T}{\kappa u_*} \quad . \quad (E.3.4)$$

Typically, $\beta < 1$ holds for profiles representing significant suspended sediment loads. In the following section, $\beta < 1$ is assumed for exploiting exact solutions to miscellaneous integrals.

E.4 Miscellaneous integrals

Depth integrals of the previously derived concentration profile and the related sand-flux profile can be expressed analytically at high accuracy. The essential function appearing in these expressions is the Gamma function $\Gamma(z)$ defined through Euler's integral (Abramowitz & Stegun, 1972, p.255):

$$\Gamma(z) = \int_0^{\infty} t^{z-1} e^{-t} dt \quad . \quad (E.4.1)$$

The Gamma function satisfies the recurrency formula $\Gamma(1+z) = z\Gamma(z)$ showing that $\Gamma(1+n) = n!$ holds for integer argument $n=1,2,..$. Related to (E.4.1) is the Psi or Digamma function:

$$\psi(z) = \frac{1}{\Gamma(z)} \frac{d\Gamma(z)}{dz} \equiv \frac{d \ln\{\Gamma(z)\}}{dz} \quad . \quad (E.4.2)$$

In view of the depth-integral of the concentration profile (E.3.3), the Beta function is of relevance and it is related to the Gamma function (E.4.1) through:

$$B(u, v) = \int_0^1 t^{u-1} (1-t)^{v-1} dt = \frac{\Gamma(u)\Gamma(v)}{\Gamma(u+v)} = B(v, u) \quad . \quad (E.4.3)$$

The depth-integral of the logarithmic velocity profile (E.1.3) and the Rouse concentration profile (E.3.2) yields the (total) sediment flux. The solution for the depth-integrated sand flux is derived on the following integral (Gradshteyn & Ryzhik, 1980, eq. 4.253):

$$\int_0^1 x^{\mu-1} (1-x^r)^{\nu-1} \ln x \, dx = \frac{1}{r^2} B\left(\frac{\mu}{r}, \nu\right) \left\{ \psi\left(\frac{\mu}{r}\right) - \psi\left(\frac{\mu}{r} + \nu\right) \right\} . \tag{E.4.4}$$

The lower limit of the actual depth integrals, however, is not $Z=0$ but $Z=\delta$ being a very small number, considering that the grain size is at least four orders-of-magnitude smaller than the water depth h . Consequently, the following two approximations are sufficient, provided $\beta < 1$ holds:

$$\int_0^\delta \left(\frac{1-Z}{Z}\right)^\beta dZ = \frac{\delta^{1-\beta}}{1-\beta} \{1 - O(\delta)\} ; \tag{E.4.5}$$

$$\int_0^\delta \left(\frac{1-Z}{Z}\right)^\beta \ln Z \, dZ = \frac{\delta^{1-\beta}}{(1-\beta)^2} \{ \ln(\delta^{1-\beta}) - 1 \} \{1 - O(\delta)\} .$$

We begin with the depth-averaged concentration due to (E.3.3) yielding:

$$\bar{c} = \frac{c_a}{1-\varepsilon} \left(\frac{\delta}{1-\delta}\right)^\beta \int_\delta^1 \left(\frac{1-Z}{Z}\right)^\beta dZ . \tag{E.4.6}$$

Note the appearance of ε in (E.4.6) due to depth-averaging over h rather than over $(h-z_a)$.

The integral in (E.4.6) is related to the Beta function (E.4.3) but reduced by the first approximation in (E.4.5):

$$\int_\delta^1 \left(\frac{1-Z}{Z}\right)^\beta dZ = B(1-\beta, 1+\beta) - \frac{\delta^{1-\beta}}{1-\beta} \{1 + O(\delta)\}. \tag{E.4.7}$$

Note that in (E.4.7)

$$B(1-\beta, 1+\beta) = \Gamma(1-\beta)\Gamma(1+\beta) \tag{E.4.8}$$

holds. The depth-averaged concentration thus reads:

$$\bar{c} = \frac{c_a}{1-\varepsilon} \left(\frac{\delta}{1-\delta}\right)^\beta \left\{ B(1-\beta, 1+\beta) - \frac{\delta^{1-\beta}}{1-\beta} [1 + O(\delta)] \right\} . \tag{E.4.9}$$

Finally, the sediment flux, averaged over depth h follows from:

$$\overline{uc} = (1-\varepsilon)^{-1} \int_\delta^1 u(Z)c(Z) \, dZ , \tag{E.4.10}$$

after substituting the Rouse profile

$$c(z) = c_a \left(\frac{\delta}{1-\delta} \right)^\beta \left(\frac{1-Z}{Z} \right)^\beta, \tag{E.3.2}$$

as well as the logarithmic velocity profile

$$u = \frac{u_*}{\kappa} \left\{ \ln Z + \ln \left(\frac{\alpha}{\varepsilon} \right) \right\}. \tag{E.1.3}$$

Substitution of (E.3.2) and (E.1.3) into (E.4.10) yields the full expression:

$$\overline{uc} = \frac{u_* c_a}{\kappa(1-\varepsilon)} \left(\frac{\delta}{1-\delta} \right)^\beta \left\{ \int_\delta^1 \left(\frac{1-Z}{Z} \right)^\beta \ln Z dZ + \ln \left(\frac{\alpha}{\varepsilon} \right) \int_\delta^1 \left(\frac{1-Z}{Z} \right)^\beta dZ \right\}. \tag{E.4.11}$$

In (E.4.11), the first integral is related to (E.4.4) with $r=1$; $v=1+\beta$; $\mu=1-\beta$ whence

$$\int_0^1 \left(\frac{1-Z}{Z} \right)^\beta \ln Z dZ = B(1-\beta, 1+\beta) \{ \psi(1-\beta) - \psi(2) \}; \quad \psi(2) = 1-\gamma \tag{E.4.12}$$

holds. In (E.4.12), γ is Euler's constant and $\gamma=0.577\dots$

Using (E.4.5) as correction to the lower limit in:

$$\int_\delta^1 \left(\frac{1-Z}{Z} \right)^\beta \ln Z dZ = B(1-\beta, 1+\beta) \{ \psi(1-\beta) - \psi(2) \} - \frac{\delta^{1-\beta}}{(1-\beta)^2} \{ \ln(\delta^{1-\beta}) - 1 \} \{ 1 - O(\delta) \}. \tag{E.4.13}$$

The second integral in (E.4.11) is expressed in the exact solution for $\delta=0$ and subsequently corrected by the first approximation in (E.4.5):

$$\ln \left(\frac{\alpha}{\varepsilon} \right) \int_\delta^1 \left(\frac{1-Z}{Z} \right)^\beta dZ = \ln \left(\frac{\alpha}{\varepsilon} \right) \left\{ B(1-\beta, 1+\beta) - \frac{\delta^{1-\beta}}{1-\beta} \{ 1 - O(\delta) \} \right\},$$

or converting the multiplication with $\ln(\alpha/\varepsilon)$:

$$\ln \left(\frac{\alpha}{\varepsilon} \right) \int_\delta^1 \left(\frac{1-Z}{Z} \right)^\beta dZ = \ln \left(\frac{\alpha}{\varepsilon} \right) B(1-\beta, 1+\beta) - \frac{\delta^{1-\beta}}{(1-\beta)^2} \ln \left\{ \left(\frac{\alpha}{\varepsilon} \right)^{1-\beta} \right\} \{ 1 - O(\delta) \}. \tag{E.4.14}$$

In view of (E.4.11), (E.4.14) is added to (E.4.13), yielding:

$$\int_\delta^1 \left(\frac{1-Z}{Z} \right)^\beta \ln Z dZ - \ln \left(\frac{\alpha}{\varepsilon} \right) \int_\delta^1 \left(\frac{1-Z}{Z} \right)^\beta dZ = B(1-\beta, 1+\beta) \left\{ \psi(1-\beta) - \psi(2) + \ln \left(\frac{\alpha}{\varepsilon} \right) \right\} - \Sigma, \tag{E.4.15}$$

with

$$\Sigma = \frac{\delta^{1-\beta}}{(1-\beta)^2} \left\{ \ln \left(\frac{\alpha \delta}{\varepsilon} \right)^{1-\beta} - 1 \right\} \{ 1 - O(\delta) \}.$$

For obtaining the depth-averaged sand flux (E.4.11), (E.4.15) must be multiplied by

$$\frac{u_* c_a}{\kappa(1-\varepsilon)} \left(\frac{\delta}{1-\delta} \right)^\beta$$

E.5 Summary

Here the derivations of the previous sections are summarised for the purpose of testing the POINT-SAND model. In case of the extension *log* for the input file *indpm*, the POINT-SAND model is tested for a given:

- depth-averaged velocity;
- bed roughness length;
- grain diameter;
- sand density and
- turbulence Prandtl/Schmidt number.

For the bed roughness length z_0 Van Rijn (1993, p. 4.15) proposes for sand $k_s=6d_{50}$ and with $z_0=k_s/30$ this yields $z_0=d_{50}/5$. Table E.1 presents the formulae implemented in subroutine TSTLOG. This is routine is called when the user applies the extension *log* to the standard input file *indpm*.

parameter	explanation
h	water depth: distance fluid-bed interface to free surface
\bar{u}	depth-averaged velocity
d_{50}	grain diameter
z_0	$d_{50}/5$ (Van Rijn, p. 41.5)
α	αz_0 distance below fluid-bed interface of origin of logarithmic velocity profile
w_s	settling velocity, as implemented in the POINT-SAND model
c_a	bed concentration as implemented in the POINT-SAND model
$2d_{50}$	distance above fluid-bed interface where c_a is given; below this level no suspended sediment transport is assumed.
H	$h + \alpha z_0$
ε	$\alpha z_0 / H$
δ	$(\alpha z_0 + 2d_{50}) / H$
κ	Von Karman constant, defined in the POINT-SAND model
u_*	$\frac{\kappa(1-\varepsilon)\bar{u}}{\ln\left\{\frac{1}{\varepsilon}\left(\frac{\alpha}{e}\right)^{1-\varepsilon}\right\}}$; bed friction velocity
β	$\frac{(1-\varepsilon)w_s\sigma_T}{\kappa u_*}$; Rouse parameter
Γ	Gamma function
ψ	Psi or Digamma function
\bar{c}	$\frac{c_a}{1-\varepsilon}\left(\frac{\delta}{1-\delta}\right)^\beta \left\{ \Gamma(1-\beta)\Gamma(1+\beta) - \frac{\delta^{1-\beta}}{1-\beta} [1 + O(\delta)] \right\}$
\overline{uc}	$\frac{u_* c_a}{\kappa(1-\varepsilon)}\left(\frac{\delta}{1-\delta}\right)^\beta \left\{ \Gamma(1-\beta)\Gamma(1+\beta) \left[\psi(1-\beta) - \psi(2) + \ln\left(\frac{\alpha}{\varepsilon}\right) \right] - \Sigma \right\}$
Σ	$\frac{\delta^{1-\beta}}{(1-\beta)^2} \left\{ \ln\left(\frac{\alpha\delta}{\varepsilon}\right)^{1-\beta} - 1 \right\} \{1 - O(\delta)\}$
\overline{huc}	depth-integrated flux of suspended sediment

Table E.1 Overview of formulae for the analytic solution of the depth-integrated sand flux

E.6 Sensitivity analysis

Table E.2 presents the powers in the proportionality relation between depth-integrated sand flux and the listed inputs and their magnitude, here for 200 μm sand. Using energy arguments and the powers appearing in the Zyserman-Fredsoe bed concentration most powers in Table E.2 can be accounted for.

Input parameter	magnitude	dim.	power
Density of water (ρ_s)	1000	kg.m^{-3}	4.3
Water depth (h)	1	m	0.15
Mean velocity (U)	2	m.s^{-1}	4.5
Ratio α (in zero-velocity level αz_0)	9	-	0.23
Bed roughness length (z_0)	$4 \cdot 10^{-5}$	m	0.59
Turbulence Prandtl/Schmidt number (σ_T)	0.7	-	-2.9
Density of sand (ρ_s)	2650	kg.m^{-3}	-3.3
Sand grain diameter (d_{50})	$2 \cdot 10^{-4}$	m	-4.3

Table E.2 Powers in local proportionality relation between input parameters and depth-integrated sand flux.

F ICCE Paper on simulating wave-current interaction

1DV Simulation of Wave Current Interaction

R.E. UITTENBOGAARD^{1,2}

Email: Rob.Uittenbogaard@wldelft.nl

¹ WL | delft hydraulics, PO Box 177, 2600 MH Delft, The Netherlands

² J.M. Burgers Centre, Delft University of Technology

ABSTRACT

This paper presents the contents as well as examples of the hydrodynamic part of our time and depth-dependent 1DV solver using a Poisson solver for pressure for explicitly simulating various wave-current-turbulence interactions of periodic non-breaking surface waves propagating on horizontally uniform currents and horizontal beds. The accompanying paper (Bosboom and Klopman, 2000) presents the sand transport module interacting with this hydrodynamic solver.

The reduction in spatial dimensions excludes the simulation of some intriguing wave-current interactions such as Langmuir cells. These circulations augment the vertical exchange of horizontal momentum and of matter. Radder, see (Dingemans, 1999), proposes a cell-averaged model that will be added to our 1DV code.

Progress is also made of implementing our hydrodynamic 1DV solver into a 3D free-surface hydrostatic solver, as an interface for depth-averaged wave-forecasting models such as HISWA and SWAN, see (Groeneweg & Uittenbogaard, 2000).

1. INTRODUCTION

For stationary long-crested surface waves following or opposing a stationary turbulent current Kemp and Simons (1982, 1983) and Klopman (1994) observed in the laboratory the changes in mean-flow profile as indicated by symbols in figure 1. Using the Generalized Lagrangian Mean (GLM) theory, Groeneweg and Klopman (1998) simulated these observations excellently. The latter study induces several important questions that are addressed in this paper other subjects are included as well.

The first question is whether the observations of figure 1 can be simulated through solving this wave-current interaction (WCI) problem in Eulerian co-ordinates and with explicitly simulating the orbital motions rather than in the wave-averaged GLM. The second question is about the force distribution exerted by surface waves on the wave-averaged flow. The third question deals with describing wave-turbulence interaction. The last two questions are important for developing WCI models in 3D shallow-water solvers coupled to wave forecasting models. Apart from these questions we dedicate the 1DV solver also to the following subjects.

In The Netherlands much research is devoted to morphology and to sand transport in coastal seas through the combined action of waves and tidal or wind-driven currents. Most simulations on sand transport aim at wave-tunnel experiments (Davies et al., 1997) i.e. oscillatory flows without a free surface. The latter has no Stokes drift and exhibits boundary-layer streaming effects that differ from those due to surface waves. Consequently, a code is needed that allows for a thorough comparison of wave-tunnel experiments with wave-channel experiments. Preferably, this code should also simulate sand transport at fixed horizontal locations in shallow lakes, estuaries and coastal seas due to a directional as well as frequency spectrum of waves propagating on steady, tidal and wind-driven turbulent shear flows. This paper presents the hydrodynamic part of such a 1DV code as well as its limitations. The accompanying paper (Bosboom & Klopman, 2000) presents the sand transport module and relevant examples. The entire code is called *National Sand Transport Model* and it is intended to be used and to be improved by Dutch researchers at various universities and institutes.

The outline of this paper is as follows. Section 2 presents, in general, the methodology, the applicability and the limitations of the 1DV hydrodynamic module. Section 3 briefly exhibits the most relevant mathematical equations solved by the hydrodynamic module. Section 4 presents some examples for monochromatic and bichromatic surface waves following or opposing a stationary turbulent shear flow. Section 5 concludes and announces future work.

2. METHODOLOGY

For the applications and questions raised in the previous section, a spectral-type of 1DV solver has been designed, for all details see (Uittenbogaard et al., 1999). This solver assumes periodicity of surface waves i.e. all horizontal derivatives are converted by $\nabla_{hor} = -\underline{k} \omega^{-1} \partial / \partial t$ into temporal derivatives for given angular frequency ω but with wave-number vector \underline{k} solved by the dispersion relation, see section 3.

In this 1DV model, the orbital motions are simulated in time by solving their vertical and horizontal momentum equations as a function of the depth co-ordinate z . The solver is designed for waves propagating at arbitrary angle to a flow with an arbitrary depth-dependent direction of the current.

For each spectral wave component the user specifies the wave period, wave amplitude, wave direction and relative phase. For the mean flow the user specifies the velocity vector, either depth-averaged or at some given depth and possibly time dependent for tides, and also the mean water depth, bed roughness and time-dependent wind vector.

The solution procedure is split into an *outer loop* for the mean-flow equations and into *inner loops* for each spectral component of the orbital motions. The time stepping for solving all spectral components is synchronous. The time step used in

the *inner loop* is a fraction of the shortest wave period, the time step of the *outer loop* usually equals the shortest wave period but this choice is not strict.

A time-independent and non-equidistant grid is used with appropriate staggering of mean as well as orbital flow variables i.e. turbulence properties, vertical derivatives and vertical velocity at cell interfaces and all others at grid centres. We prefer a grid size that increases exponentially from a user-specified bed-layer thickness of $O(10.z_0)$ with z_0 the hydraulic roughness.

At every start of a new *inner loop* i.e. a new wave cycle, the wave number magnitude is solved for each spectral component of a freely propagating wave at arbitrary angle with respect to the mean flow velocity vector which is solved in the *outer loop*.

The vertical profile of the hydrodynamic pressure amplitude is solved by its linearized Poisson equation for waves on shear flows. The actual pressure is in phase with the surface elevation. The horizontal derivatives in the Poisson equation are simply replaced by their respective wave number components so that an ordinary differential equation in z is obtained, its solution is straightforward and it is based on compact differentiation (Hermite interpolation). The latter procedure is not unlike pseudo-spectral methods, see e.g. (Canuto et al., 1988).

By definition, the *inner loop* covers a single wave period, in which the intra-wave orbital-velocity vector is solved as a function of z and at time steps significantly smaller than their period. The vertical and horizontal orbital momentum equations are driven by the hydrodynamic pressure gradient. The free surface conditions are approximated and imposed at the mean water level (rigid lid) rather than exactly at the mobile water level.

The equations for turbulence, vertical sand transport, bed concentration, bed friction are also solved at *inner-loop* time steps and turbulence production depends on the sum of all spectral orbital motions and mean-flow properties, the latter remain frozen over an *outer-loop* time step.

After the completion of a wave period of a spectral component, the WCI force and other related wave-averaged quantities are updated. These wave-averaged quantities are used for the solution, in the *outer-loop*, of the mean flow vector as a function of z ; by definition the mean flow is horizontal and horizontally uniform. Per spectral component, the z -dependent horizontal WCI force vector is adjusted for maintaining a zero horizontal orbital velocity vector, averaged over the last wave cycle. The vertical WCI component is discarded, see below. The total z -dependent horizontal WCI force vector is the sum of all spectral contributions and this total WCI force appears in the horizontal momentum equations for the mean flow. The summation involves a sign change so that the action of the horizontal WCI force represents the transfer of mean horizontal momentum in the orbital motions to the mean-flow momentum. In other words, the WCI force disappears in the sum of mean-flow and all (spectral) orbital momentum equations.

The orthogonal horizontal velocity components are solved by the mean-flow equations, which are time dependent and mutually coupled through Coriolis force, turbulence eddy viscosity and bed friction. The mean flow is assumed to be

horizontal and horizontally uniform and to be driven by *hydrostatic* pressure gradients. The latter are adjusted so that the desired depth-averaged velocity vector is maintained. Note that the user specifies the depth-averaged mean-flow vector or the mean-flow vector at some given depth, either by time series or by harmonics (tidal motions).

In wave-tunnel experiments the turbulence-averaged flow is horizontal and the horizontal pressure gradients are independent of z and these flow properties are represented by the mean-flow momentum equations. Consequently, for simulating wave-tunnel experiments, the user switches off the entire *inner-loop* solution procedure and specifies the velocity harmonics (period, velocity amplitude, phase and direction) at constant water depth of the “mean flow” solved in the *outer-loop*. The *outer-loop* time steps are now a fraction of the shortest wave period. Turbulence and sand transport equations are now solved at *outer-loop* time steps. The latter procedure then simulates wave-tunnel rather than wave-channel experiments using the same code, input, turbulence model and sand transport equations as for surface waves propagating on a flow.

This completes the overview of the solution procedure. The next section presents the most important equations solved by the 1DV code but first we conclude with some comments and a summary of limitations.

The previous overview suggests that, at least by its design, the code is applicable for wave-tunnel or wave-channel experiments or the local hydrodynamics of waves in wind-driven lakes, tide-driven estuaries as well as coastal seas. The outer-loop has options for computing the net surface heat flux for given air temperature, pressure, air humidity, cloudiness and position on the globe and for simulating the density stratification (thermocline) by water temperature, see (Van Kester et al., 1997).

Obviously, this 1DV solver for wave-current-turbulence interactions has the following limitations. In principle, although some tolerance may be allowed, the waves should be subcritical, non-breaking, horizontally periodic and with small surface elevations. The bed should be horizontal without sand ripples; the mean flow should be horizontal and uniform in horizontal planes. There are no limitations on mean flow shear rates. Presently, the subtle surface-boundary conditions for purely viscous flows are crudely approximated (rigid lid) suggesting this 1DV solver is primarily suitable for waves on turbulent shear flows.

3. THE EQUATIONS

In view of the previous description of the methodology, this section presents most of the code’s mathematical equations with brief comments only. The order of presentation equals the sequence by which these equations are solved. For notational convenience all orbital variables obtain a tilde and are assumed to be period through:

$$\tilde{\psi} = \hat{\psi} \operatorname{Re} \left\{ \exp(i \underline{k} \cdot \underline{x} - i \omega t) \right\} ; \quad i = \sqrt{-1} \quad . \quad (1)$$

Uittenbogaard et al. (App. B, 1999) show that for waves on a shear flow at arbitrary

directions the orbital velocity vectors of a single spectral component are in single vertical plane with directional deviations of $(u./c_p)$ where $u.$ is the bed-shear velocity and c_p the wave's phase speed. Therefore, the horizontal part of the orbital velocity vector is assumed to be parallel with its wave-number vector.

At the start of each wave cycle the *inner loop* begins with solving the vertical profile of the hydrodynamic pressure amplitude \hat{p} . Its Poisson equation is linearized in orbital motions; turbulence stresses are neglected and devoted to dealing with shear flows yielding:

$$\nabla^2 \tilde{p} = -2 \frac{\partial \underline{U}}{\partial z} \cdot \nabla \tilde{w} \quad , \quad (2)$$

where \underline{U} is the mean horizontal flow, p is the fluid pressure divided by mean density and \tilde{w} is the vertical orbital velocity. For (2) we apply the boundary conditions

$$\left(\frac{d \tilde{p}}{dz} \right)_{z=0} = 0 \quad ; \quad \tilde{p}|_{z=\bar{\zeta}} = g \tilde{\zeta} \quad (3)$$

the latter imposed at mean water level $z=\bar{\zeta}$ (rigid lid), the bed level is $z=0$. Substituting the linearized equation for vertical momentum (6) in (2) and using (1) yields the following ordinary differential equation, equivalent to Rayleigh's equation,

$$\frac{d^2 \hat{p}}{dz^2} + 2B \frac{d\hat{p}}{dz} - |\underline{k}|^2 \hat{p} = 0 \quad ; \quad B = \frac{1}{\Omega(z)} \cdot \frac{\partial \underline{U} \cdot \underline{k}}{\partial z} \quad ; \quad \Omega(z) = \omega_s - \underline{k} \cdot \underline{U}(z) \quad (4)$$

for the pressure amplitude with given angular frequency ω_s but yet unknown horizontal wave-number vector \underline{k} . The latter is obtained by the dispersion equation

$$\text{for } \omega_s : \left(\frac{\partial}{\partial t} + \underline{U} \cdot \nabla \right)^2 \tilde{\zeta} + \frac{\partial \tilde{p}}{\partial z} \Big|_{\bar{\zeta}} = 0 \quad (5)$$

derived from (6) after neglecting turbulence stresses. By iteration, the wave number magnitude is found so that the equality $\Omega^2(\bar{\zeta}) = \partial^2 \hat{p} / \partial z \partial \bar{\zeta}$ is satisfied. During the subsequent wave cycle the pressure-amplitude profile $\hat{p}(z; \omega_s)$ for a given angular frequency ω_s is converted into the instantaneous pressure $\tilde{p}(z, t; \omega_s)$ being in phase

with the surface elevation, see (3). The vertical pressure gradient of the spectral component with angular frequency ω_s then drives the momentum equation

$$\text{for } \omega_s: \quad \frac{\partial \tilde{w}_s}{\partial t} + \underline{U}(z) \cdot \nabla \tilde{w}_s + \frac{\partial \tilde{p}(z, t; \omega_s)}{\partial z} = \frac{\partial}{\partial z} \left\{ 2(\nu + f_{hp} \nu_T) \frac{\partial \tilde{w}_s}{\partial z} \right\} \quad (6)$$

for the vertical orbital velocity component while retaining just the most important Reynolds stress term. In (6), ν is the kinematic viscosity, ν_T the eddy viscosity and f_{hp} a wave- and turbulence-dependent high-pass filter function that is described later in this section.

For a spectrum of waves, the orbital velocity vector is rewritten as $\tilde{\underline{u}} \rightarrow \tilde{\underline{u}} + \tilde{\underline{v}}$ where $\tilde{\underline{v}}$ represents all other contributions at wave numbers that differ from wave number \underline{k} belonging to $\tilde{\underline{u}}$. Formally we thus define

$$\tilde{\underline{u}} = \tilde{\underline{u}}(\omega_s) \quad ; \quad \tilde{\underline{v}} = \sum_{n \neq s} \tilde{\underline{u}}(\omega_n) \quad (7)$$

where ω_s is the user-specified angular frequency component appearing in (4). The decomposition (7) as well as the previously introduced approximation $(\tilde{\underline{u}})_{hor} = \tilde{u} \hat{\underline{k}}$ with $\hat{\underline{k}}$ the unit vector parallel to the wave number vector $\underline{k}(\omega_s)$ yields the following equation for horizontal orbital momentum:

$$\begin{aligned} \text{for } \omega_s: \quad \frac{\partial \tilde{u}}{\partial t} + \{(\underline{U} + \tilde{\underline{v}}) \cdot \hat{\underline{k}} + \tilde{u}\} \frac{\partial \tilde{u}}{\partial x_k} + \tilde{w}_s \frac{\partial \tilde{u}}{\partial z} + \tilde{w}_s \frac{\partial \underline{U} \cdot \hat{\underline{k}}}{\partial z} + \frac{\partial \tilde{p}(z, t; \omega_s)}{\partial x_k} = \\ F_k(z) + \frac{\partial}{\partial x_k} \left\{ 2(\nu + f_{hp} \nu_T) \frac{\partial \tilde{u}}{\partial x_k} \right\} + \frac{\partial}{\partial z} \left\{ (\nu + f_{hp} \nu_T) \left(\frac{\partial \tilde{u}}{\partial z} + \frac{\partial \tilde{w}_s}{\partial x_k} \right) \right\} \end{aligned} \quad (8)$$

In (8), \tilde{w}_s is the vertical velocity component solved by (6) with the pressure induced at angular frequency ω_s and x_k is the horizontal co-ordinate along the $\underline{k}(\omega_s)$ -direction. In view of table 1, all wave-current terms are retained in (8) and most of the wave-wave interacting terms, the exception being the contribution of the vertical velocity component by other spectral components to the advection term.

In (8) appears the important horizontal WCI force F_k that is parallel to $\hat{\underline{k}}$. Rather than using some model for WCI, we define the WCI force in the 1DV code numerically such as to obtain a zero or negligibly small mean horizontal orbital velocity.

	\underline{U}	$\tilde{\underline{v}}$	$\tilde{\underline{u}}$
--	-----------------	-------------------------	-------------------------

\underline{U}	$\underline{U} \cdot \nabla \underline{U}$	$\underline{U} \cdot \nabla \tilde{v}$	$\underline{U} \cdot \nabla \tilde{u}$
\tilde{v}	$\tilde{v} \cdot \nabla \underline{U}$	$\tilde{v} \cdot \nabla \tilde{v}$	$\tilde{v} \cdot \nabla \tilde{u}$
\tilde{u}	$\tilde{u} \cdot \nabla \underline{U}$	$\tilde{u} \cdot \nabla \tilde{v}$	$\tilde{u} \cdot \nabla \tilde{u}$

Table 1 Overview of linear and non-linear (wave-wave) interaction terms in (8).

Our WCI force is determined per spectral component over its last completed wave period and it reads:

$$F_k(z, (l + \frac{1}{2})T; \omega_s) = \frac{1}{T^2} \int_{lT}^{(l+1)T} \tilde{u}(z, t; \omega_s) dt \quad ; \quad T = \frac{2\pi}{\omega_s} \quad ; \quad l = 0, 1, 2, 3, \dots \quad (9)$$

In (9) the integral expresses averaging over the last wave cycle and F_k is the mean orbital velocity divided by its wave period. The origin of (9) lies in the success of a similar procedure for adjusting the horizontal hydrostatic pressure gradient, see (14). Other formulations for $F_k(z; \omega_s)$ may be chosen provided they serve the essential purpose namely obtaining zero mean horizontal orbital velocity at every z-level.

The last hydrodynamic step in the inner-loop solution procedure involves the closure for turbulence stresses, particularly those in phase with the orbital strain rates. We use the concept of eddy viscosity/diffusivity for exchange of momentum and mass respectively. It can be argued that turbulent eddies with overturning time scales and length scales longer than those of the orbital velocity fluctuations are deformed without significant irreversible exchanges of orbital momentum. Conversely, the orbital momentum fluxes are altered irreversibly by turbulent eddies at scales faster and smaller than those of the orbital motions and these we define here as high-pass filtered turbulence. For surface waves affecting the bed it can be shown that high-pass filtering in terms of frequency spectra dominates so that we define the high-pass filter function

$$f_{hp} = \frac{\nu_T(\omega_s)}{\nu_T(0)} = \frac{\langle u'^2(\omega_s) \rangle \tau_L(\omega_s)}{\langle u'^2(0) \rangle \tau_L(0)} \quad , \quad (10)$$

reducing the total eddy viscosity of mean flow to the effective eddy viscosity $\nu_T(\omega_s)$ acting on orbital motions with angular frequency ω_s . In (10), $\tau_L(\omega_s)$ is the integral time scale of the high-pass filtered turbulence velocity component u' and we omitted the dependence on space and time. For an exponentially decaying velocity correlation coefficient it is straightforward to show that

$$f_{hp} = \left\{ 1 - \frac{2}{\pi} \arctan(\theta) \right\} \left\{ 1 - \exp[-\theta^{-1}] \right\} \quad ; \quad \theta = \omega_s \tau_L(0) \quad (11)$$

holds and obviously f_{hp} is unity for the mean flow. This expression is used in determining the total production Q of turbulent kinetic energy through

$$Q = 2\nu_T \left(D_{ij} D_{ij} + \sum_s f_{hp}(\omega_s) \tilde{d}_{ij}(\omega_s) \tilde{d}_{ij}(\omega_s) \right) \quad (12)$$

where, omitting space and time dependence, D_{ij} is the mean-flow strain rate and $\tilde{d}_{ij}(\omega_s)$ is the strain-rate tensor related to orbital motions with angular frequency ω_s . Using the well-known k-L, k- ω or k- ϵ turbulence models, $\tau_t(0)$ can be expressed in modelled turbulence properties. Consequently, (12) is a closed expression and (12) is used in some eddy-viscosity turbulence model at each *inner-loop* time step when all spectral components have been advanced a single *inner-loop* time step.

At the start of a new *outer-loop* time step all wave-averaged quantities are determined over their most recent wave period and these averages are used in solving the mean-flow horizontal momentum equation

$$\frac{\partial \underline{U}}{\partial t} + \nabla P + f \hat{e}_z * \underline{U} = \frac{\partial}{\partial z} \left\{ (\nu + \nu_T) \frac{\partial \underline{U}}{\partial z} \right\} - \underline{F} \quad ; \quad \underline{F} = \sum_s F_k(\omega_s) \hat{k}(\omega_s) \quad (13)$$

with Coriolis parameter f and \hat{e}_z the vertically upward unit vector. We omit describing the usual boundary conditions and just note that they include wave-averaged stresses. In (13), \underline{F} is the sum of all spectral WCI force vectors and the minus sign in (13) is due to its momentum transfer property so that F_k vanishes when adding (8) multiplied by \hat{k} to (13). The user specifies the depth-averaged velocity vector \underline{U}_0 , possibly time-dependent. We fulfil this condition by adjusting the horizontal hydrostatic pressure gradient, divided by fluid density, through

$$\nabla P = \frac{\tau_{surf} - \tau_{bed}}{\zeta} - \underline{F}^{(\zeta)} + \frac{(\underline{U} + \underline{U}^S)^{(\zeta)} - \underline{U}_0}{\Delta t_{out}} \quad (14)$$

The first term in the RHS of (14) is the difference in wind-shear and bed-shear stress vector divided by the mean water depth $\bar{\zeta}$, the second term represents the total WCI force where the superscript (ζ) denotes depth-averaging. The last term in the RHS of (14) represents the essential correction procedure with Δt_{out} the *outer-loop* time step by which (13) is solved. This correction procedure has shown to work excellently also for time dependent \underline{U}_0 . Finally, in (14) appears the depth-average of the Stokes drift $\underline{U}^S(z)$. Due to the rigid-lid formulation, the wave-induced mass flux vector \underline{M} of water between crest and trough is not simulated and instead we substitute the analytical formulation

$$\underline{M} = \overline{\zeta} \underline{U}^{s(\zeta)} = \sum_s \overline{\zeta} \overline{\tilde{u}(\zeta)} \hat{k} + \frac{1}{2} \sum_s \overline{\zeta}^2 \frac{\partial \underline{U}}{\partial z} \Big|_{\overline{\zeta}}, \quad (15)$$

derived in (Winterwerp & Uittenbogaard, 1997) and of second-order accuracy in surface elevation; in (15) the overbar denotes averaging over the most recent wave cycle.

The expression (15) is used for correcting just the mass flux of water because as long as sediment concentrations are zero near the free surface the Stokes drift of sediment is simulated directly, see also the accompanying paper (Bosboom and Klopman, 2000).

4. EXAMPLES

The lines in figure 1 present the simulation with this 1DV spectral solver and these show a good correspondence with observations; the inserted detail in Figure 1 has a logarithmic z-axis. The simulation is based on 150 layers that increase exponentially from a 0.1 mm thick bed layer for a 160 mm/s turbulent current parallel to the direction of propagation of a monochromatic wave of 1.44 s period and 60 mm amplitude on 500 mm deep water. The k-L turbulence model is used with the no-slip condition.

Figure 2 compares the simulated and observed horizontal velocity amplitude, which is slightly underestimated for the wave against the current. Figure 4 presents the simulated WCI force transferring momentum between (8) and (13).

Figure 3 compares similar simulations with experiments on bichromatic waves with wave amplitude and periods of 49 and 35 mm at 1.70 and 1.36 s, following the same current as for the monochromatic-wave experiment (figure 1).

Figure 5 presents time series of simulating a second-order Stokes wave (485 and 188 mm at 6.5 and 3.25 s) that propagates on 2.4 m deep water, without a depth-averaged current, using the k- ϵ turbulence model and 200 layers increasing exponentially from the 0.84 mm bed layer. Due to phase lags, the horizontal velocity signal at 100 mm above the bed is deformed inside the wave-induced boundary layer. The temporal pattern of the eddy viscosity coefficient ν_T shows the anticipated phase lags increasing with distance above the bed. Further, the time series of ν_T inside the wave-induced boundary layer show local maximums occurring just after the zero crossing of the velocity. These local maximums are induced by the high-pass filter function f_{hp} , see (11), that increases to unity with reducing turbulent time scales. This function first boosts the turbulence production (12) as soon as the wave-induced strain rates increase after zero velocity but subsequently the turbulence time scale increases and then f_{hp} reduces this production. This pattern in turbulence and mixing mimics phase-coupled turbulence bursting in oscillatory flows. This type of laminar-turbulence transition and/or secondary instability, however, is not introduced in the high-Reynolds k- ϵ model nor in the high-pass filter function so that

this part of the temporal pattern of v_T is a fortunate coincidence but it lacks a sound physical modelling concept.

5. CONCLUSIONS AND FUTURE DEVELOPMENTS

We conclude that the 1DV spectral solver, in Eulerian co-ordinates, is capable of simulating various wave-current-turbulence interactions. Therefore the 1DV solver is recommended for simulating laboratory experiments of sand transport under combined waves and currents as demonstrated in the accompanying paper (Bosboom and Klopman, 2000).

The high-pass filter function f_{hp} (11) appears to produce the correct wave-induced boundary layer thickness. This function, however, is applicable only if the strain rates and turbulence stresses of each spectral wave component are known explicitly but not in the case of composite temporal signals such as in wave-tunnel experiments. The modelling concepts of f_{hp} as well as the occurrence of laminar-turbulence transitions suggest the implementation of so called low-Reynolds Reynolds Stress Model that avoids f_{hp} and is suitable for composite time signals.

The reduction in spatial dimensions in the 1DV code excludes the simulation of the wave-driven secondary circulation in laboratory channels (Nepf & Monismith, 1991) by the Craik-Leibovich vortex force. In case of waves following the current this circulation transports low momentum fluid to the channel's centre (Dingemans et al., 1996) and enhances the backward bending of the mean profiles in figures 1 and 3.

Likewise, the 1DV code lacks the simulation of Langmuir cells in unbounded waters that augment the vertical exchange of horizontal momentum and of matter (Thorpe, 1984). Radder, see (Dingemans, 1999), proposes a cell-averaged model for vertical transport of horizontal momentum and matter and his model will be added to our 1DV code.

In the 1DV code, we decomposed hydrodynamic processes into those driven by hydrostatic pressure (*outer loop*) or driven by non-hydrostatic pressure (*inner loop*), for the latter assuming horizontal periodicity. This approach suggests the implementation of the *inner-loop* solver into a 3D free-surface hydrostatic solver, see (Groeneweg & Uittenbogaard, 2000). In this arrangement, the *inner-loop* solver then converts depth-averaged wave properties, estimated by wave-forecasting systems such as HISWA and SWAN, into z-dependent WCI force vector, z-dependent Stokes drift vector and z-dependent wave-induced turbulence production for use in 3D hydrostatic free-surface solvers and their 3D turbulence models.

6. ACKNOWLEDGEMENTS

Discussions with Judith Bosboom, Gert Klopman and Jan v.d. Graaff gave more insight in the model's limitations. This work is jointly funded by the MAST-3 SEDMOC project, in the framework of the EU-sponsored Marine Science and Technology Programme (MAST-III), under contractno. MAS3-CT97-0115, the Dutch Ministry of Transport and Public Works (Rijkswaterstaat) under contractno. RKZ-725 part I, the Delft Cluster organisation and WL | DELFT HYDRAULICS.

7. REFERENCES

- Bosboom, J. & G. Klopman 2000 Intra-wave sediment transport modelling. *Proc. 25th Int. conf. on coastal Engineering*, Sydney.
- Canuto, C., M.Y. Hussaini, A. Quarteroni, T.A. Zang 1988 *Spectral methods in fluid dynamics*. Springer-Verlag, Heidelberg.
- Davies, A.G., J.S. Ribberink, A. Temperville & J.A. Zyserman 1997 Comparisons between sediment transport models and observations made in wave and current flows above plane beds. *Coastal Engineering*, 31, pp. 163-198.
- Dingemans, M.W. 1999 *3D wave-current modelling*. WL|delft hydraulics, report Z2612.
- Dingemans, M.W., J.A.Th.M. van Kester, A.C. Radder & R.E. Uittenbogaard 1996 The effect of the CL vortex force in 3D wave-current interaction. *Proc. 25th Int. conf. on coastal Engineering*, Orlando, pp. 4821-4832..
- Groeneweg, J. & G. Klopman 1998 Changes of the mean velocity profiles in the combined wave-current motion described in a GLM formulation. *J. Fluid Mech.*, vol. 370, pp. 271-296.
- Groeneweg, J. & R.E. Uittenbogaard 2000 *1DV wave solver coupled to 3D hydrostatic flow solver*. Abstract submitted to *Waves 2001* (3-5 Sept.), San Fransisco.
- Klopman, G. 1994 *Vertical structure of the flow due to waves and currents*. WL|delft hydraulics, report H840.30, Part II.
- Kemp, P.H. & R.R. Simons 1982 The interaction between waves and a turbulent current: waves propagating with the current. *J. Fluid Mech.*, vol. 116, pp. 227-250.
- Kemp, P.H. & R.R. Simons 1983 The interaction between waves and a turbulent current: waves propagating against the current. *J. Fluid Mech.*, vol. 130, pp. 73-89.
- Kester, J.A.Th.M. Van, R.E. Uittenbogaard & E.D. de Goede 1997 *Onderzoek naar numerieke modellering van thermocliene effecten in de Noordzee*, WL|delft hydraulics, report Z2034.30
- Nepf, H.M. & S.G. Monismith 1991 Experimental study of wave-induced longitudinal vortices. *J. Hydraulic Engng*, 117(12), pp. 1639-1649.
- Thorpe, S.A. 1984 The effect of Langmuir circulation on the distribution of submerged bubbles caused by breaking wind waves. *J. Fluid Mech.*, vol. 142, pp. 151-170.
- Uittenbogaard, R.E., J. Bosboom & T. van Kessel 1999 *Numerical simulation of wave-current driven sand transport*. WL|delft hydraulics, report Z2733.41.
- Winterwerp, J.C. & R.E. Uittenbogaard 1997 *Sediment transport and fluid mud flow*. WL|delft hydraulics, report Z2005.

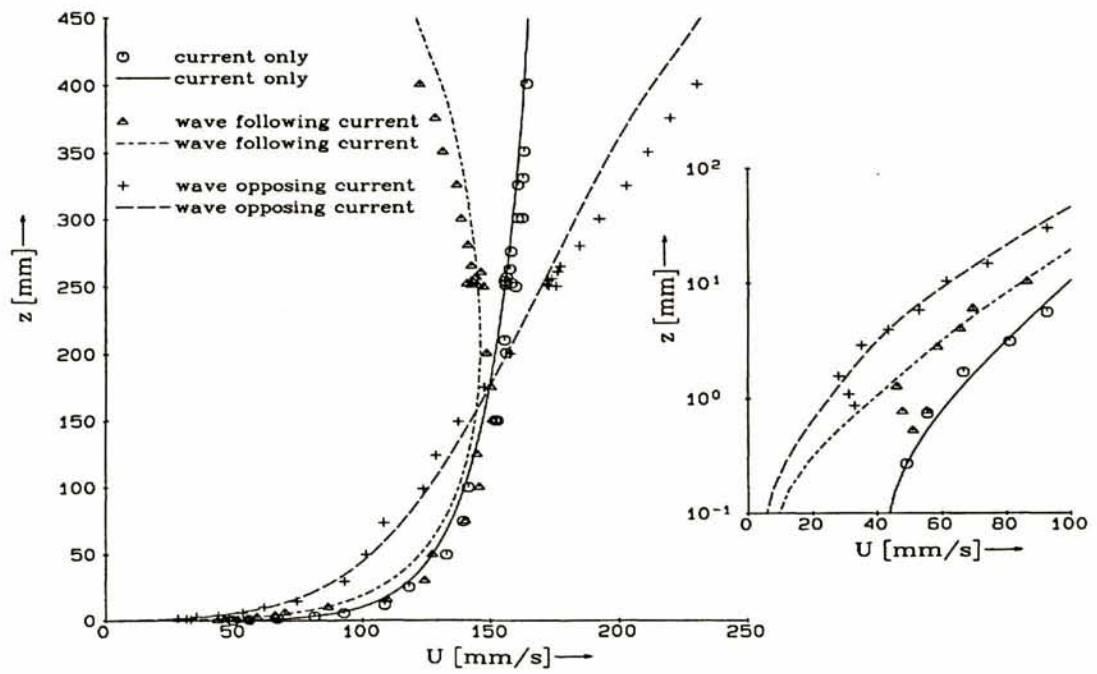


Figure 1. Mean current profile of 1DV code (lines) compared with Klopman's (1996) observations (symbols), monochromatic waves following or opposing the current.

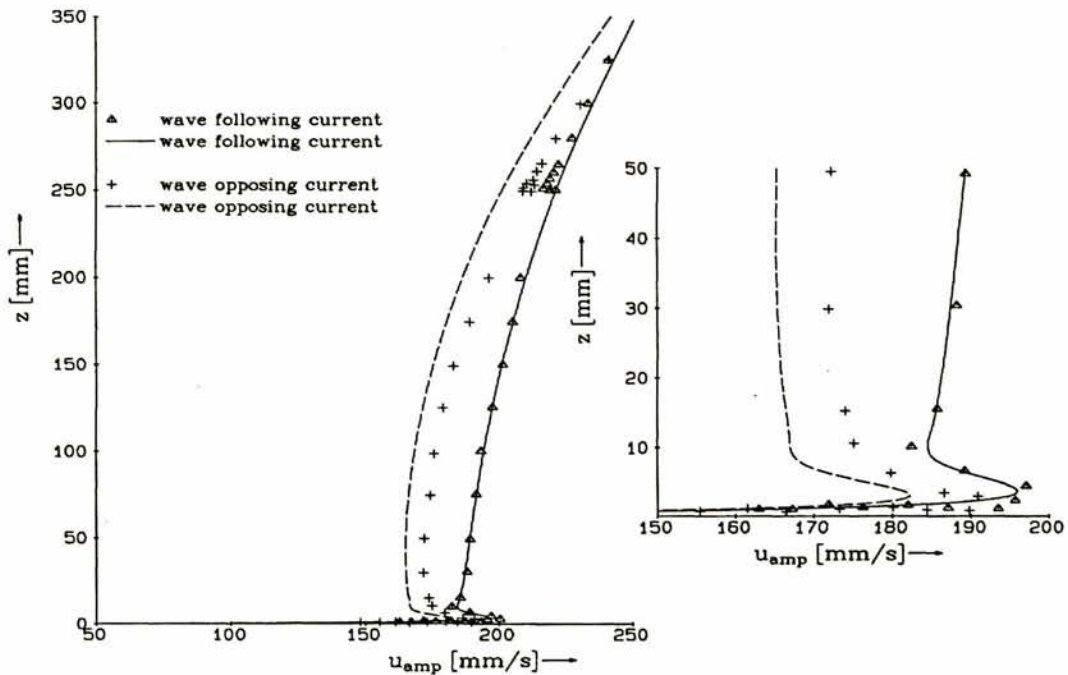


Figure 2. Carrier-wave amplitude of 1DV code (lines) compared with Klopman's (1996) observations (symbols) for monochromatic waves following or opposing the current.

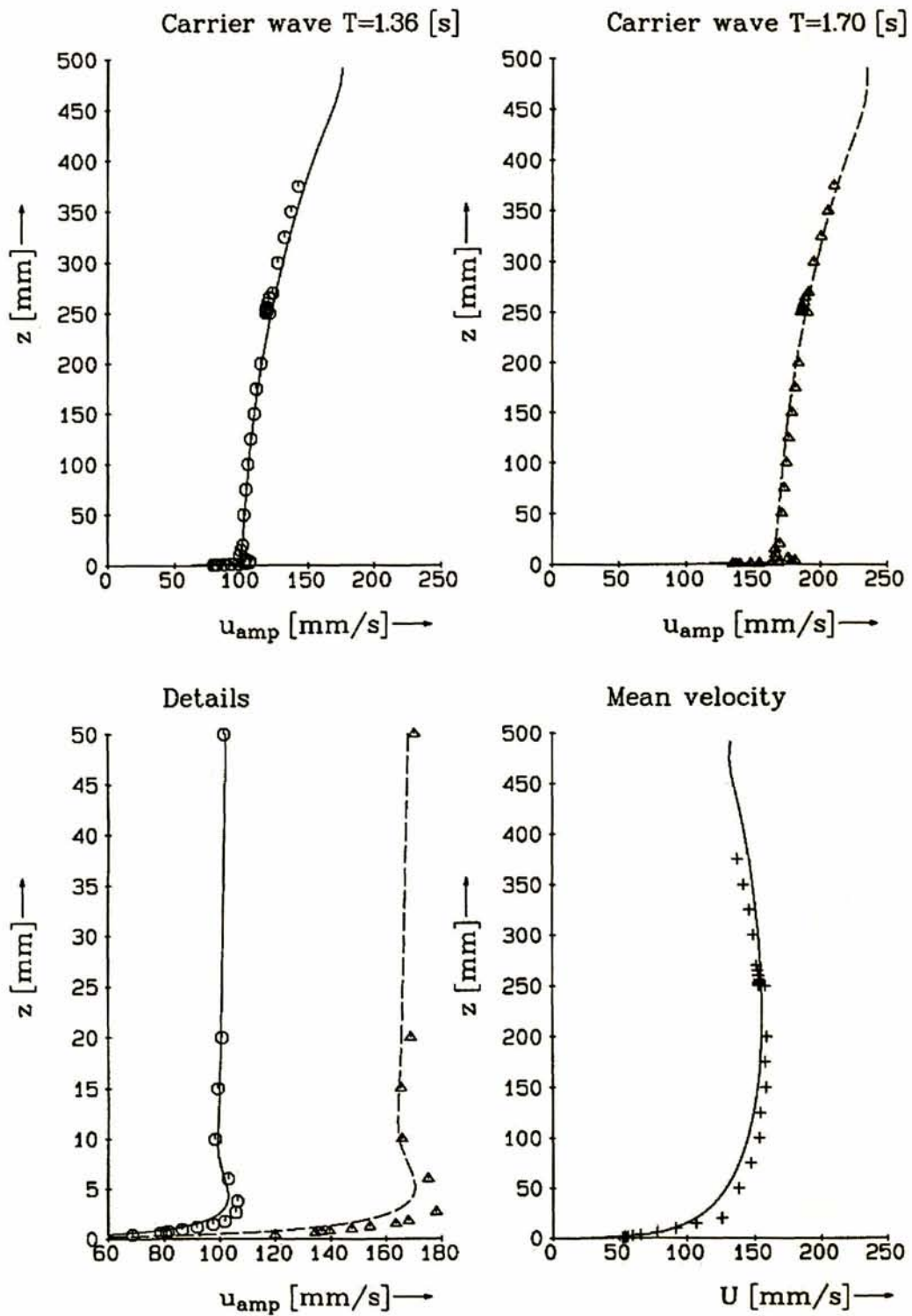


Figure 3. Mean current profile and carrier wave amplitudes of 1DV code (lines) compared with Klopman's (1996) observations (symbols) for bichromatic waves following the current.

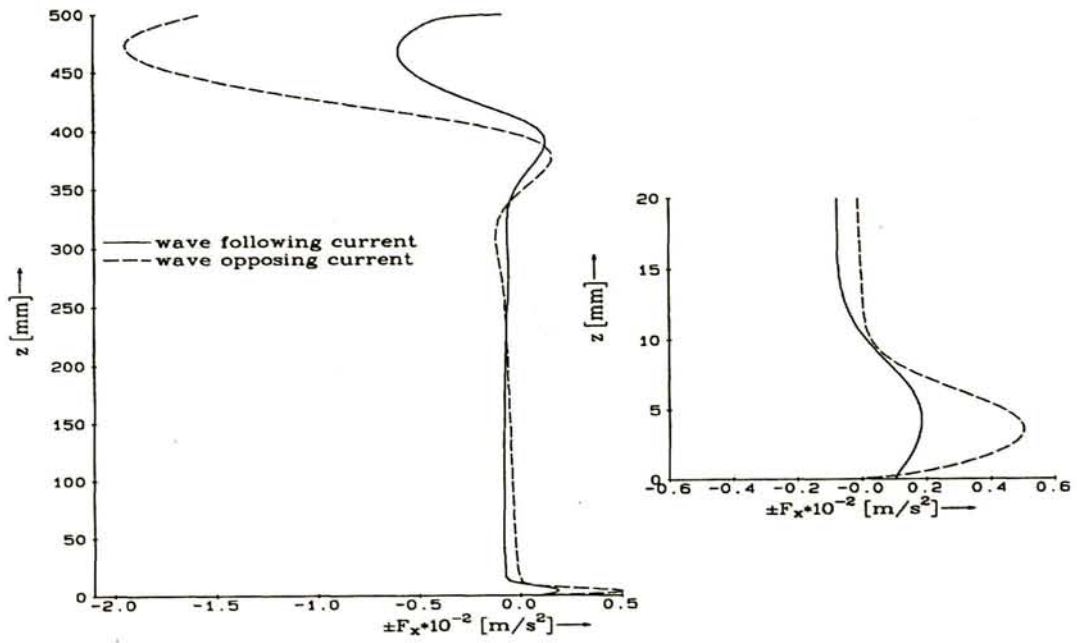


Figure 4. The WCI force for the simulations of figure 1.

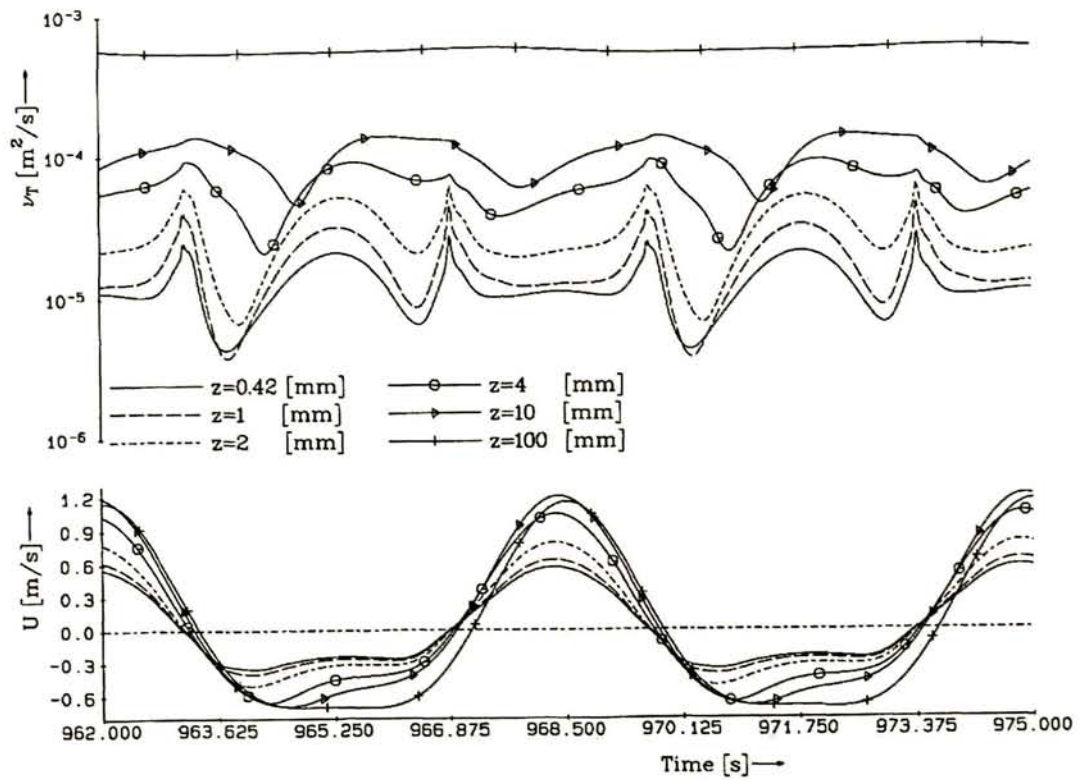


Figure 5. Total horizontal velocity U and eddy viscosity ν_T , estimated by $k-\epsilon$ turbulence model and high-pass filtered, derived from 1DV simulation of second-order Stokes wave, no current.

G ICCE Paper on intra-wave sediment transport

Intra-wave sediment transport modelling

Judith Bosboom^{1,2} and Gert Klopman^{3,2}

Abstract

This paper investigates the effect of wave-induced streaming on sediment transport by applying a newly developed numerical sediment transport model. The transport model solves the intra-wave oscillatory motion and sediment concentrations. The wave-induced streaming in the wave boundary layer, as occurs in propagating waves, is an integral part of the computed flow field. Comparison of the computed flow field with wave-current flume experiments gives good results. The model can also describe the horizontally uniform situation in an oscillating water tunnel, in which vertical orbital velocities and wave-induced streaming are absent. The model is successfully tested against measurements of sediment concentrations and net transport rates performed in a large-scale oscillating water tunnel. The importance of streaming is assessed by comparing model results for the case with wave-induced streaming and the case of the oscillating water tunnel. For a typical water tunnel condition, the effect of the absence of vertical velocities and streaming is found to be a 40% lower net transport rate than the corresponding situation under propagating waves. These differences result not only from the net transport by the streaming velocity, but are also due to an increased asymmetry in the model of near-bed velocity, bed shear-stress and resulting sediment concentrations. This result suggests that the differences in transport rates between water tunnel and propagating waves may not be insignificant.

Introduction

Since in the wave boundary layer under propagating waves the horizontal (\tilde{u}) and vertical velocities (\tilde{w}) are not exactly 90 degrees out of phase, an ensemble-averaged shear stress $-\rho\langle\tilde{u}\tilde{w}\rangle$ is introduced. As a result, a shoreward directed net velocity exists in the wave boundary layer (see Figure 1). Although this wave-induced streaming (Longuet Higgins, 1953) streaming is small, it is potentially important for the net-sediment transport, since the sediment is concentrated near the bed.

¹ WL|Delft Hydraulics, P.O. Box 177, 2600 MH Delft, The Netherlands. JudithBosboom@hotmail.com

² Netherlands Centre for Coastal Research (NCK), Department of Civil Engineering and Geosciences, Delft University of Technology, Delft, The Netherlands

³ Albatros Flow Research, P.O. Box 85, 8325 ZH Vollenhove, The Netherlands. Gert.Klopman@afr.nl (corresponding author)

In order to study sediment transport phenomena under controlled simulated wave conditions, often oscillating water tunnels are used. The generated oscillatory flow is purely horizontal. The water tunnel therefore provides a first-order representation of the sediment transport phenomena in the boundary layer under progressive waves. This paper assesses the effect of neglecting the vertical orbital velocities, horizontal gradients and wave-induced streaming on the net sediment transport rates.

We therefore first present a newly developed sediment transport model, which solves the intra-wave-period and depth variation of the velocity and concentration fields. A common assumption in such models is the neglect of the horizontal gradients in the fluid momentum equation and the sediment mass balance, apart from the horizontal pressure gradient. Neglecting these horizontal-gradient terms results in a model which does not take vertical orbital velocities, horizontal convection and streaming into account. This is a good representation of the oscillating water tunnel situation. Since the fields of velocity and sediment concentration are determined locally by a one-dimensional vertical (1DV) approach, the computational effort is limited.

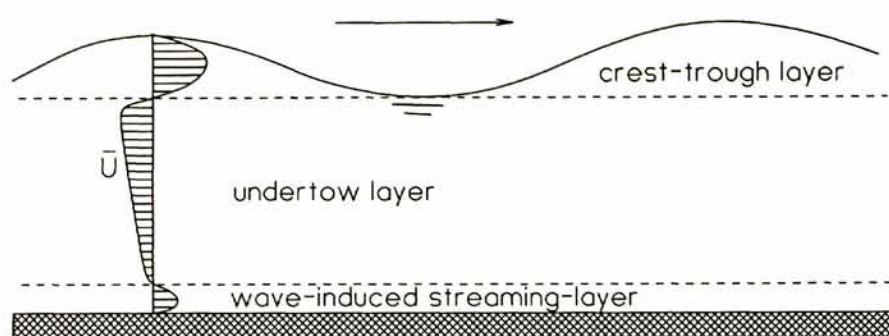


Figure 1 Net velocity profile under propagating waves. In the wave boundary layer, the net velocity is in the direction of wave propagation

In the model presented here, the horizontal gradient terms and the resulting vertical velocities are accounted for in an essentially 1DV framework by rewriting the horizontal derivatives in terms of time derivatives under the assumption of periodicity in time and space. To our knowledge this method was first used by Trowbridge et al. (1986) for the oscillatory boundary layer under waves. By retaining the horizontal and vertical convective acceleration terms in the fluid momentum equation, the Stokes drift and wave-induced streaming in the wave boundary layer are an integral part of the flow field. The concentration fields include the effects of advection by the wave orbital motion to second-order and therefore the wave drift of suspended sediment.

Further, an asset of the model is the consistent treatment of the complete water column (including the wave boundary layer). Other important aspects of the model are the applicability to random waves and the modelling of the water-sediment interaction.

In the verification of the model a number of aspects is considered. First, attention is directed towards the wave-induced streaming in the direction of wave propagation in the wave boundary layer. For this the model is compared with wave-current flume experiments. Secondly, the model is tested against measurements of sediment

concentrations and net transport rates performed in an oscillating water tunnel. Comparing computed sediment transport rates for the situation in the oscillating water tunnel and the corresponding situation in propagating waves assesses the importance of streaming.

Model formulation

A one-dimensional vertical (1DV) solver has been designed (Uittenbogaard, 2000) and extended with a sediment distribution model (Uittenbogaard et al., 1999, 2000), such that the suspended sand transport under sheet-flow conditions can be simulated. The model has a finite difference discretization in the vertical direction, and a mixed frequency-domain / time-stepping approach for the time stepping. Horizontal derivatives are rewritten as time derivatives assuming they are propagating with the wave celerity. The selection of a non-equidistant vertical grid allows for resolving details of the wave boundary layer while simulating the flow along the entire water depth.

The combined wave and current flow is determined from the following non-linear Reynolds' averaged horizontal momentum equations (see for more detail Uittenbogaard, 2000):

$$\frac{\partial u}{\partial t} + u \frac{\partial u}{\partial x} + v \frac{\partial u}{\partial y} + w \frac{\partial u}{\partial z} = -\frac{1}{\rho} \frac{\partial p}{\partial x} - \frac{\partial \langle u'w' \rangle}{\partial z} - \frac{\partial \langle u'v' \rangle}{\partial y} - \frac{\partial \langle u'u' \rangle}{\partial x}, \quad (1a)$$

$$\frac{\partial v}{\partial t} + u \frac{\partial v}{\partial x} + v \frac{\partial v}{\partial y} + w \frac{\partial v}{\partial z} = -\frac{1}{\rho} \frac{\partial p}{\partial y} - \frac{\partial \langle v'w' \rangle}{\partial z} - \frac{\partial \langle v'v' \rangle}{\partial y} - \frac{\partial \langle u'v' \rangle}{\partial x}. \quad (1b)$$

where the Reynolds' averaged velocity in the directions (x,y,z) is denoted by (u,v,w) , p is the pressure, ρ is the mass density of the water and $\langle \cdot \rangle$ denotes ensemble averaging. The turbulence fluxes are determined using a $k-\varepsilon$ turbulence closure model, via the Boussinesq hypothesis. The vertical velocities are solved through a (reduced) vertical momentum equation. The pressure $p(z)$ driving this equation is derived from the solution of Poisson-like equations for linear wave propagation on a slowly varying, vertically sheared current.

In order to transform these equations to a 1DV framework, which is attractive from a computational point of view, all horizontal derivatives in Eq. (1) to time derivatives by assuming a wave of permanent form propagating with a celerity $\underline{C}_w = (C_{w,x}, C_{w,y})$, and thus

$$\frac{\partial}{\partial x} = -\frac{1}{C_{w,x}} \frac{\partial}{\partial t}; \quad \frac{\partial}{\partial y} = -\frac{1}{C_{w,y}} \frac{\partial}{\partial t}. \quad (2)$$

The assumption of spatially periodic wave motions excludes sloping beds and strong decay or growth of wave properties. The spectral solution procedure to Eq. (1) is such that for each harmonic component in the velocity signal the propagation

velocity according to the dispersion relation is used for the transformation given by Equation (2).

The corresponding Reynolds' averaged conservation statement for the sediment assuming that the upward transport of sediment is due to turbulence diffusion reads:

$$\frac{\partial c}{\partial t} + u \frac{\partial c}{\partial x} + v \frac{\partial c}{\partial y} + w \frac{\partial c}{\partial z} - \frac{\partial w_s c}{\partial z} = - \frac{\partial \langle c'w' \rangle}{\partial z} - \frac{\partial \langle c'v' \rangle}{\partial y} - \frac{\partial \langle c'u' \rangle}{\partial x}, \quad (3)$$

where c is the sediment concentration and w_s the concentration dependent sediment fall velocity. In order to model the turbulence sediment flux, we make the assumption of upward transport due to turbulence diffusion as for the fluid. The loading of the flow with suspended sediment is considered to yield damping of turbulence. Analogous to the procedure for the fluid momentum equations, the horizontal derivatives in Equation (3) are converted to time derivatives via the assumption of periodicity.

We use a bottom boundary condition which is a function of the instantaneous bed shear stress and with an upper cut-off for the sediment concentration at large values of the bed shear stress. The sediment concentration is prescribed at a reference level $z_a = 2D_{50}$:

$$c(z_a, t) = c_b(t), \quad (5)$$

In this way we expect to account for the majority of the transport near the bed; the bed load transport is expected to be small as compared to the suspended load contribution. For more detailed description of the sediment transport model one is referred to Uittenbogaard et al. (2000).

Comparison with Scheldt flume experiments

The model is tested against wave-current flume experiments of Klopman (1994). The experiments were conducted to study the flow kinematics under combined wave-current motion. Tests were performed with mono-chromatic, bi-chromatic and random waves without current, following current, opposing current and current only. The cases with combined wave-current motion are investigated in Uittenbogaard (2000).

Here we only consider the case of mono-chromatic waves without a current. These test series without a current show the well known wave-induced streaming near the bed, in the direction of wave propagation. The experiments were performed in WL|Delft Hydraulics' Scheldt flume in a water depth of 0.5 m. The wave period is 1.44 s and the wave amplitude 0.06 m. Figure 2 and Figure 3 show the mean velocity (left plot) and amplitude of the first harmonic (right) plot for the entire water depth and for the lower 10 cm respectively. We find an overestimation of the streaming velocity and a slight underestimation of the velocity amplitude in the overshoot region. In general the measurements and computations compare reasonably well.

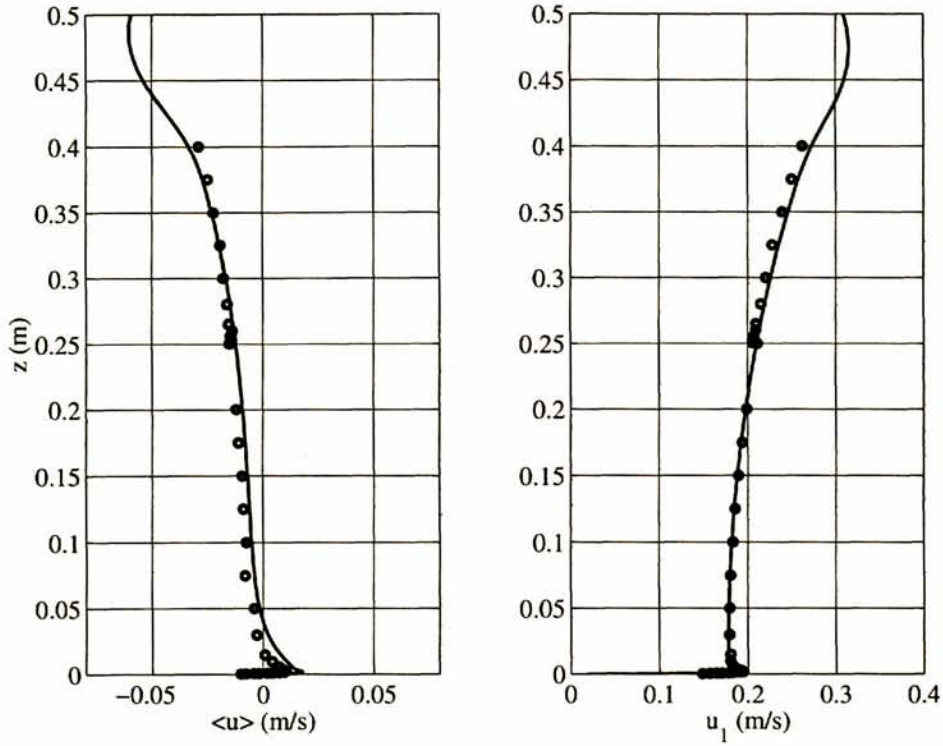


Figure 2 Mean velocity (left) and amplitude of the first harmonic (right) for the monochromatic wave test of Klopman (1994)

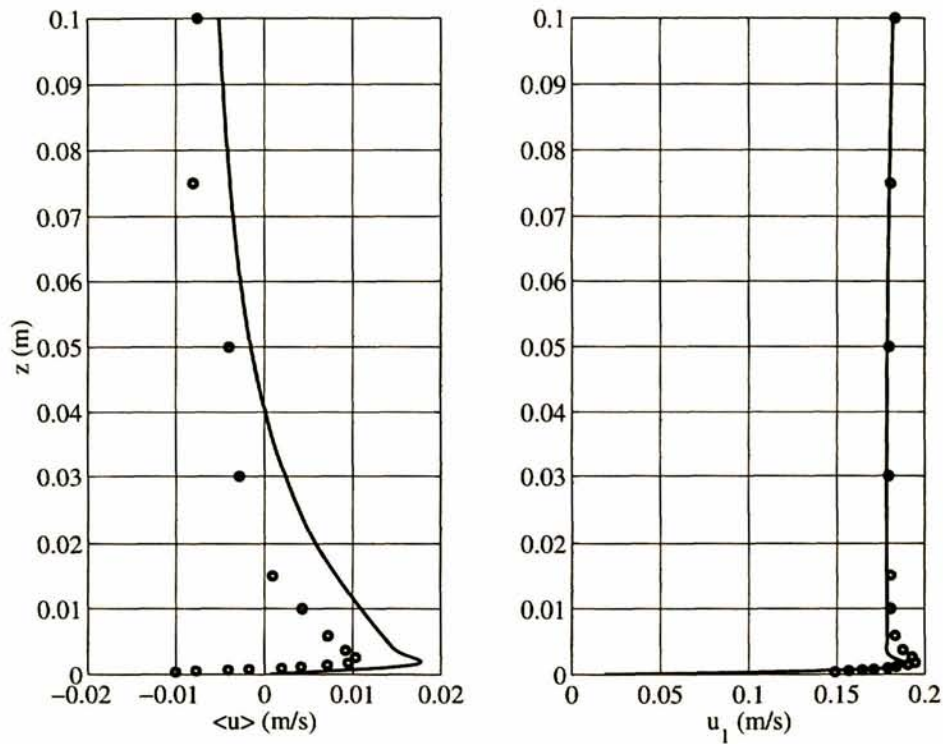


Figure 3 Mean velocity (left) and amplitude of the first harmonic (right) for the monochromatic wave test of Klopman (1994), lower 10 cm

Comparison with Large Oscillating Water Tunnel experiments

In order to study sediment transport phenomena under controlled simulated wave conditions at full scale, the Large Oscillating Water Tunnel (LOWT) has been constructed at WL|Delft Hydraulics, see Figure 4. The system basically consists of a vertical U-tube with one open leg. The other leg is provided with a piston. At the bottom of the test section a sediment bed may be installed. The tunnel is equipped with a flow circulation system, such that besides an oscillating flow a current can be generated. The generated oscillatory flow is purely horizontal. As opposed to the case of progressive waves, vertical orbital velocities and horizontal gradients, and thus wave-induced streaming, are absent.

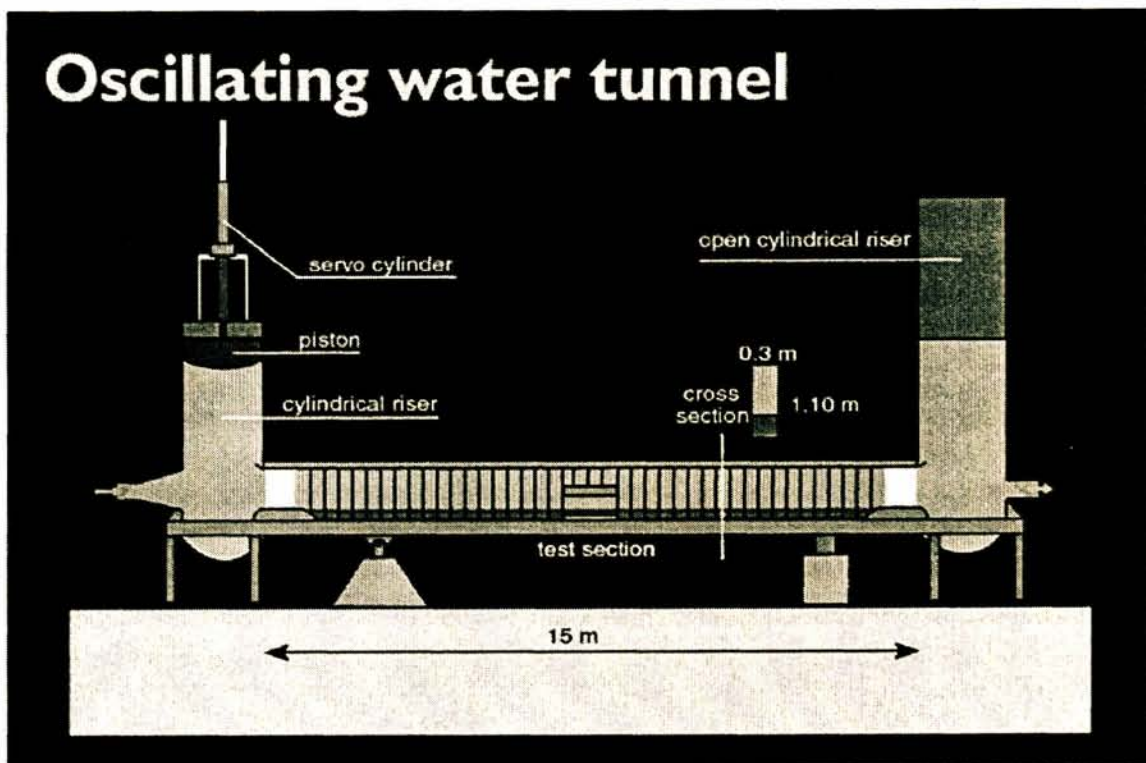


Figure 4 Schematic representation of the Large Oscillating water tunnel

Plane-bed experiments carried out in the LOWT for a sinusoidal oscillation plus current (Katopodi et al, 1994a,b) and for a regular asymmetric (second-order Stokes) oscillation in the absence of a mean current (Ribberink and Al-Salem, 1994, 1995) were used for model validation. The sand median diameter is $D_{50} = 210 \mu\text{m}$. The sets of experiments covered a range of wave periods, flow velocity and asymmetry. For a few tests detailed time-dependent measurements of flow kinematics and sediment transport were performed. For all tests net transport rates were derived using a mass-conservation technique. Time-averaged concentrations were measured using a suction system, whereas time-dependent concentrations were measured using a conductivity concentration meter (CCM) in the sheet flow layer and an optical concentration meter (OPCON) in the suspension layer. The conditions used here are the sinusoidal wave plus current condition E1 and the regular asymmetric wave condition C1.

Sinusoidal oscillation plus current, LOWT condition E1

The model input parameters for the E1 case are a mean velocity $\langle u \rangle = 0.17$ m/s at 10 cm and a fundamental harmonic $u_1 = 1.7$ m/s with a period of 7.2 s. Comparison between the model and the measurements for the cycle-averaged vertical profiles of horizontal velocity $\langle u \rangle$ and sediment concentration are shown in the upper two plots of Figure 5.

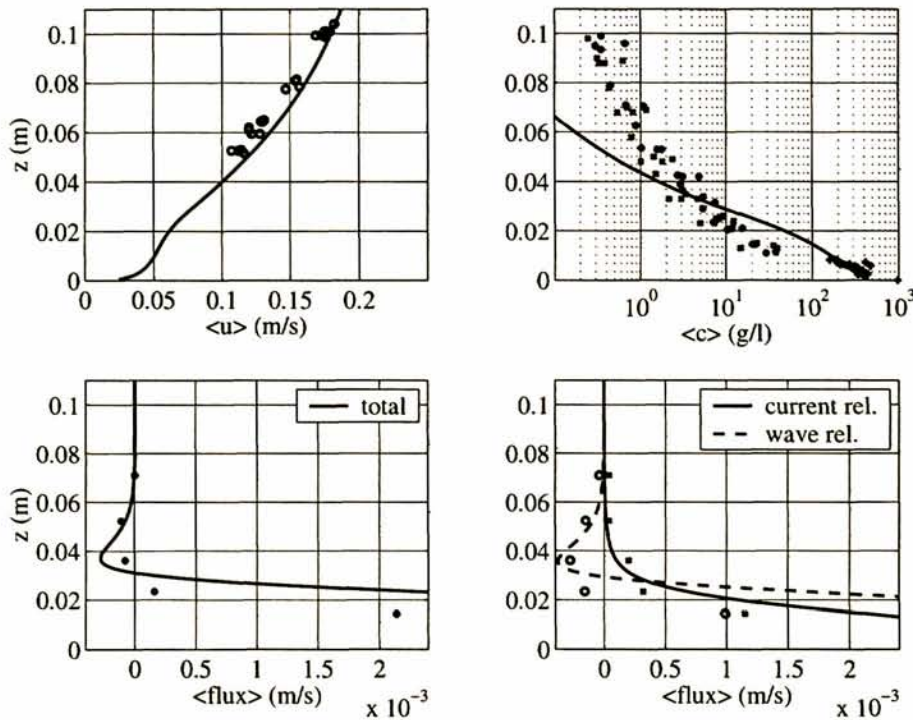


Figure 5 Comparison between model predictions and measurements by Katopodi et al. (1994a,b): the vertical profiles of cycle mean velocity (upper left panel) $\langle u \rangle$ and cycle mean concentration $\langle c \rangle$ (upper right panel) and the profiles of the cycle mean total sediment flux $\langle uc \rangle$ (lower left panel) and current related $\langle u \rangle \langle c \rangle$ and wave related $\langle \tilde{u} \tilde{c} \rangle$ contributions (lower right panel).

It is not surprising that the velocity magnitude around the matching level between data and model agrees well with the model. However, also the velocity shear is predicted quite accurately such that the velocity is in good agreement throughout entire region shown. The large sediment concentrations close to the bed are in good agreement with the measurements, but up to a few centimeters above the bed the sediment concentrations are clearly overestimated. An underestimation occurs for higher elevations.

In the lower left panel of Figure 5, the predicted time-averaged flux profiles are compared with the data. The model and the data show an 'onshore' transport in the near-bed layer and an 'offshore' transport in the outer suspension layer. Any mismatch between model and data further from the bed can be expected to be relatively unimportant for the net transport predictions. The overestimation of the net flux close to the bed is important for the net transport prediction; in this case the net transport is overestimated with a factor 1.5. Other tests showed that this is a general trend of the

model; the model tends to overestimate the net transport predictions, with factors up to 2.

Not surprisingly, these features qualitatively correspond with model predictions discussed in a MAST2 G8-M intercomparison study comparing four numerical 1DV wave boundary layer models with LOWT data (Davies et al., 1997): for the idealised water tunnel conditions, the equations underlying the here described model reduce to equations similar as used in other wave boundary layer models, in which vertical velocities and horizontal gradients are neglected a priori. Note that this is a valid assumption for models simulating LOWT experiments.

Second order Stokes condition without net current, LOWT condition C1

In the C1 experiment the free-stream velocity at $z = 20$ cm is:

$$u_{\infty}(t) = \langle u \rangle + u_1 \cos(\omega t) + u_2 \cos(2\omega t) \quad (5)$$

where $T = 2\pi/\omega = 6.5$ s and the velocity amplitudes are $\langle u \rangle = 0.025$ m/s, $u_1 = 0.85$ m/s and $u_2 = 0.27$ m/s.

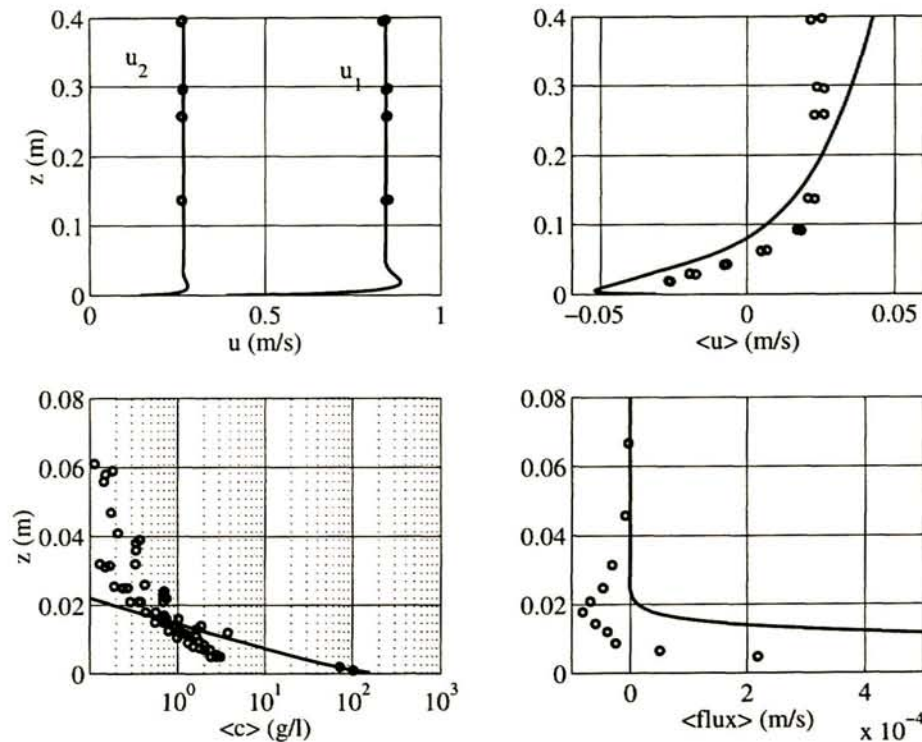


Figure 6 Comparison between model predictions and measurements by Ribberink and Al-Salem (1994,1995): the vertical profiles of first harmonic velocity amplitude u_1 and second harmonic u_2 (upper left panel) and cycle mean velocity $\langle u \rangle$ (upper right panel) and the profiles of the cycle concentration $\langle c \rangle$ (lower left panel) and mean total sediment flux $\langle uc \rangle$ (lower right panel).

The vertical profiles of the net current and first and second harmonic amplitudes is shown in the upper panels Figure 6. The existence of the small residual current in the tunnel, as shown in the upper left panel, has been discussed by Ribberink and Al-

Salem (1995). Near the bed ($z < 6$ cm) this current is 'against the wave propagation direction', i.e. in the direction of the flow during the trough half cycle. Further from the bed, a small compensating flow in opposite direction occurs. This boundary layer streaming results from the asymmetry in the turbulence characteristics under asymmetric waves. Although the mean shear stress $\bar{\tau} = -\rho \overline{u'w'}$ is effectively zero at each level, $\bar{v} \partial \bar{u} / \partial z = -\bar{v} \partial \bar{u} / \partial z$ is in general unequal to zero for asymmetric waves with asymmetric \bar{v} and \bar{u} . The present model predicts the tunnel streaming rather well (upper right panel).

In the lower left panel of Figure 6, the sediment concentration is compared with the measurements. As for E1, the concentration close to the bed are in good agreement with the measurements. Further from the bed, the concentrations are first significantly overestimated and then underestimated. The lower right panel shows the time-averaged sediment flux. The model significantly overestimates the height of zero flux, which is a direct result of the underestimation of the phase differences between velocity and concentration. This is generally the case in models based on a diffusion approach for the upward transport of sediment (see Davies et al 1997, Bosboom et al, 1998).

These features lead to a general overestimation of the net transport rates by the model. However, when testing the model against the complete set of experiments with a sand median diameter of $D_{50} = 210 \mu m$, covering a range of wave periods, flow velocity and asymmetry, all computed transport rates for the idealised water tunnel situation are within a reasonable factor 2 of the data.

Waves versus water tunnel: the effect of streaming

In the previous section, it was seen that in the water tunnel a turbulence asymmetry-induced streaming is present as a result of the wave asymmetry. Close to bed this streaming is against 'wave propagation direction' or in the direction of the wave trough velocity. In propagating waves however, the net wave-induced streaming close the bed is in opposite direction, i.e. in wave propagation direction. The water tunnel is therefore not a complete representation of the situation under propagating waves, although it is often assumed to be, since many transport models were calibrated using the tunnel data without making corrections to account for the difference in streaming.

In order to assess the importance of this streaming for the net transport rates, the model was run in 'water tunnel mode' for water tunnel condition C1 (see previous section) and in corresponding 'propagating wave mode'. The results of these two model runs were compared on velocity, concentration and flux profiles and the net sediment transport rate.

In first instance we choose a propagating wave condition corresponding to the wave tunnel by matching the oscillatory velocity above the wave boundary layer i.e., at $z \approx 0.2$ m. This means waves with a wave height $H = 1$ m and a wave period of 6.5 s propagating in a water depth of 2.4 m. In the right panel of Figure 7 the first and second harmonic amplitudes are given for both the water tunnel (drawn lines) and the

corresponding propagating wave condition (dashed lines). The profiles of the mean velocity are given in the left panel. The latter plot clearly shows the turbulence asymmetry induced streaming and the wave-induced streaming, which are of the same order of magnitude but of opposite sign. The magnitude of the net flow is small, both in absolute sense and relative to the root mean square velocity.

Figure 8 (left panel) shows the mean velocity in the lower 1.5 cm above the bed for the tunnel and propagating wave cases. The right panel shows the mean sediment concentration, which is remarkably similar in both cases. The total flux (lower left panel) however and the wave and current related fluxes (lower right panel) show some distinct differences. The major difference in the total flux occurs very close to the bed, where the propagating wave case shows a higher time mean flux. Upon integration it appears that the total sediment transport is $\approx 40\%$ higher in the propagating wave case. As expected from the signs of the mean velocity, the current related flux is 'onshore' and 'offshore' directed for the propagating wave and water tunnel case respectively. This effect however only results in part of the differences in the observed total fluxes. The wave related flux also shows some important differences, being larger for the propagating wave case near the bed, but smaller at higher elevations above the bed.

The difference between tunnel and wave case seems to be largely due to the wave induced effects on the flow field. Switching off the vertical velocity related terms in the advection-diffusion equation for the sediment concentration did result in very small changes in the results.

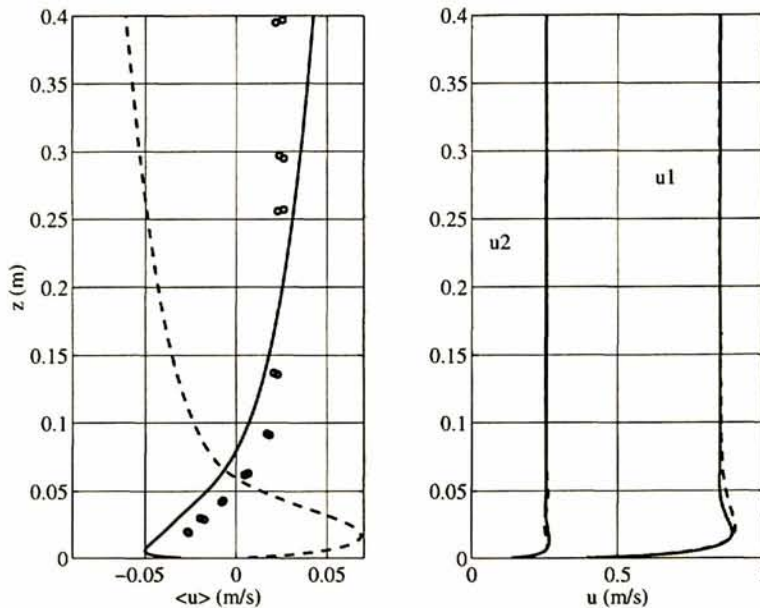


Figure 7 Comparison between model results for the water tunnel (drawn lines) and the corresponding propagating wave condition (dashed lines). Profiles of mean velocity (left panel, including data for the tunnel situation) and amplitudes of first and second harmonics (right panel).

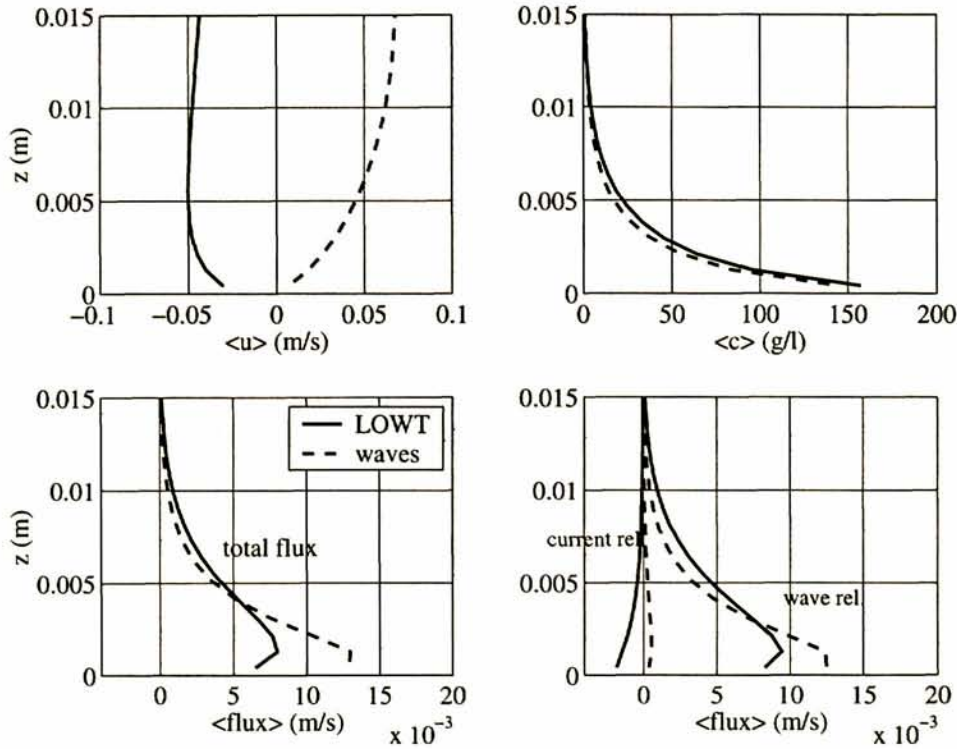


Figure 8 Comparison between model results for the water tunnel (drawn lines) and the corresponding propagating wave condition (dashed lines): the vertical profiles of cycle mean velocity (upper left panel) $\langle u \rangle$ and cycle mean concentration $\langle c \rangle$ (upper right panel) and the profiles of the cycle mean total sediment flux $\langle uc \rangle$ (lower left panel) and current related $\langle u \rangle \langle c \rangle$ and wave related $\langle \tilde{u} \tilde{c} \rangle$ contributions (lower right panel).

Summarising, the observed net effect on the total flux going from the water tunnel to the corresponding propagating wave situation is an approximately 40 % higher net transport rate. Both the current related (due to opposite signs of the streaming velocity in waves and LOWT) and wave related flux are significantly different. This result suggest that the differences in transport rates between water tunnel and propagating waves may not be insignificant. The differences in the wave related flux become clear when inspecting the instantaneous bed shear stress and sediment concentrations in either case (Figure 9).

The upper right panel of Figure 9 shows that the oscillatory velocities in the wave boundary layer are practically identical. The total velocities however, as shown in the upper left panel are significantly different, as a result of the opposite sign of the streaming velocity. This significantly influences the asymmetry of the velocity signals (upper left panel) and bed shear stress (see shear velocity in lower left panel). In the propagating wave case the asymmetry is enhanced by the streaming in the wave propagation direction, or, in the direction of the crest velocity. In the water tunnel case however, the turbulence asymmetry induced streaming, in the direction of the trough velocity, reduces the asymmetry of the velocity, bed shear stress and sediment concentrations. The increased asymmetry in the concentrations close to the bed results in an increased wave related flux near the bed where the oscillatory velocity and sediment concentrations are only slightly out of phase. Thus, differences in the sediment fluxes between the water tunnel and waves not only result from the net

transport by the streaming which is opposite in sign, but from a decreased asymmetry in the water tunnel velocity signal, bed shear stress and therefore sediment concentrations as well.

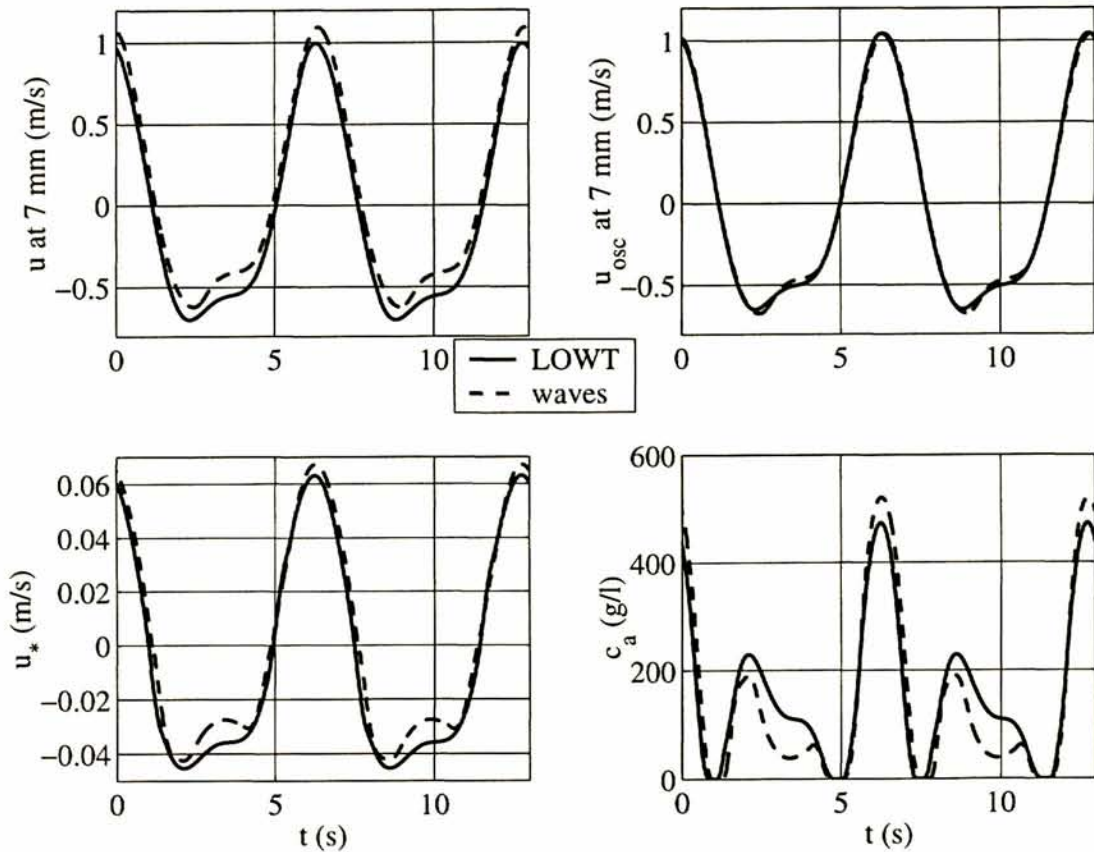


Figure 9 Comparison between model results for the water tunnel (drawn lines) and the corresponding propagating wave condition (dashed lines): the instantaneous total velocity (upper left panel) oscillatory velocity (upper right panel), the instantaneous shear velocity (lower left panel) and sediment concentration (lower right panel).

In the above, we talked about the corresponding propagating wave case as the case which would yield the same identical oscillatory velocity signal in both wave and water tunnel case. The mean velocity in the water tunnel is matched at a certain level with the known, measured, mean velocity. For the propagating wave case, the mean velocity profile is determined using the condition that the mean depth-averaged velocity is zero. One could just as well argue that the reasoning to determine the conditions that should be compared should be the other way around and start at the real wave case. This is illustrated in Figure 10 where the result for the previous comparison are repeated and a new case LOWT2 is added. Here it is assumed that in the field we measure a velocity signal, oscillatory and mean, above the wave boundary layer, at $z = 0.2$ à 0.3 m. We carry out a test in the LOWT, which simulates this field condition. So instead of experiment C1 with a mean velocity at $z = 0.2$ m of $\langle u \rangle = 0.025$ m/s, we have an experiment with a mean velocity at $z = 0.25$ m of -0.05 m/s (experiment LOWT2). In that case the difference in transport rates between propagating wave case and water tunnel case becomes only larger.

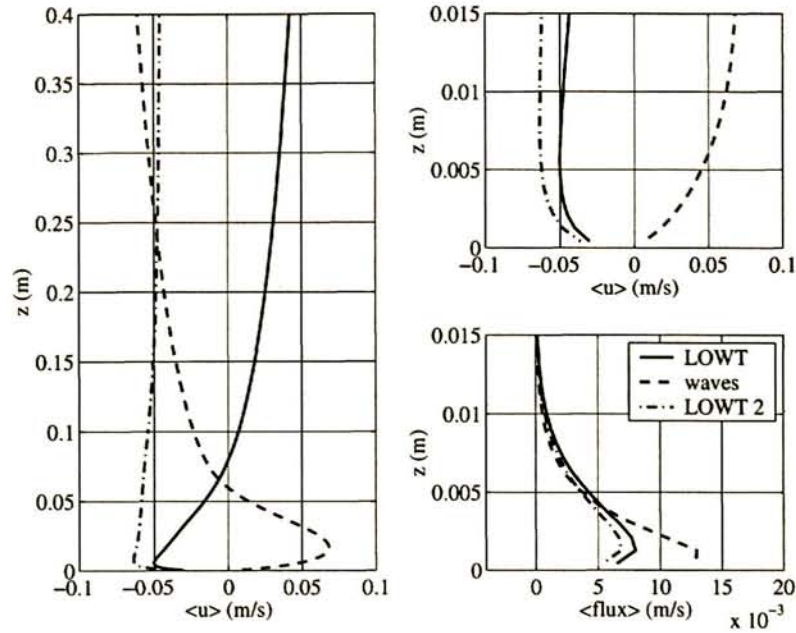


Figure 10 Comparison between model results for the water tunnel case LOWT (drawn lines) and LOWT2 (dash-dot) and the corresponding propagating wave condition (dashed lines): cycle mean velocity (left panel, upper right panel) $\langle u \rangle$ and cycle mean total sediment flux $\langle uc \rangle$ (lower right panel).

Conclusions

The following conclusions can be drawn:

1. The 1DV model provides a means to assess the flow field and sediment transport under waves and current over the full water depth including the bed boundary layer. By switching off the vertical velocities the model can also compute the flow and sediment fields as found in an oscillating water tunnel.
2. The flow kinematics computed by the model agree well with measurements both in a wave-current flume and an oscillating water tunnel.
The sediment transport rates computed with the model agree in general to within a factor of two with those obtained in the oscillating water tunnel. However, the model in general overpredicts the sediment concentration near the bed and overestimates the level of zero sediment flux.
3. The turbulence asymmetry induced streaming in the oscillating water tunnel is of opposite sign as the wave induced streaming under propagating waves. The sediment transport rate was found to be 40 percent higher under waves than for the oscillating water tunnel. This suggests that relationships between near-bed velocities and sediment transport derived from oscillating water tunnel experiments should be corrected for the absence of wave induced streaming in the bed boundary layer.
4. This increase in transport rates is partly due to the 'onshore' directed transport by wave-induced streaming. Further, differences in wave-related transport occur between water tunnel and propagating waves which are due to differences in asymmetry of near-bed velocities (owing to the streaming more asymmetric under propagating waves), bed shear stress and therefore sediment concentrations.

Acknowledgements

This work is undertaken in the SEDMOC project, in the framework of the EU-sponsored Marine Science and Technology Programme (MAST-III), under contract no. MAS3-CT97-0115. It is cosponsored by the Dutch Ministry of Transport and Public Works (Rijkswaterstaat), WL|Delft Hydraulics in the framework of the Netherlands Centre for Coastal Research (NCK) and Delft Cluster Sediment Transport under contract no. 03.01.01

References

- Bowen, A.J., 1980. Simple models of nearshore sedimentation; beach profiles and longshore bars. *The Coastline of Canada*, Ed. S.B. Cann, Geological Survey of Canada, Ottawa, pp.1-11.
- Bosboom, J., Klopman, G., Reniers, A.J.H.M., Stive, M.J.F., 1998. Analytical model for wave-related sediment transport. *Proc. ICCE 1998*, pp. 2573-2586.
- Davies, A.G., J.S. Ribberink, A. Temperville and J.A. Zyserman, 1997. Comparisons between sediment transport models and observations in wave and current flows above plane beds. *Coastal Engineering* **31**, pp. 163-198.
- Katopodi, I., Ribberink, J.S., Ruol P., Koelewijn, R., Lodahl, C., Longo, S., Crosato, A., and Wallace, H., 1994. *Intra-wave sediment transport in an oscillatory flow superimposed on a mean current*. WL|Delft Hydraulics, Report H1684, Part III.
- Katopodi, I., Ribberink, J.S., Ruol, P. and Lodahl, C., 1994. Sediment transport measurements in combined wave current flows. *Proc. of Coastal Dynamics*, 1994, Barcelona, ASCE.
- Klopman, G., 1994. *Vertical structure of the flow due to waves and currents: Laser-Doppler flow measurements for waves following or opposing a current*. WL|Delft Hydraulics report H840.30 Part II.
- Longuet-Higgins, M.S., 1953. Mass transport in water waves. *Phil. Trans. Roy. Soc. London A* **245**, pp. 535-581
- Ribberink, J.S. and Al-Salem, A.A., 1994. Sediment transport in oscillatory boundary layers in cases of rippled beds and sheet flow. *J. of Geophys. Res.*, **99**(C6), pp. 12707-12727.
- Ribberink, J.S. and Al-Salem, A.A., 1995. Sheet flow and suspension of sand in oscillatory boundary layers. *Coastal Eng.* **25**, pp. 205-225.
- Rijn, L.C. van, 1993. *Principles of sediment transport in rivers, estuaries and coastal seas*. Aqua Publ. (The Netherlands).
- Trowbridge, J.H. and Kanetkar, C.N., 1986. Numerical simulations of turbulent wave boundary layers. *Proc. ICCE 1986*, ASCE, pp. 1623-1637.
- Uittenbogaard, R.E., Bosboom, J. and T. van Kessel, 1999. *Numerical simulation of wave-current driven sand transport*. WL| Delft Hydraulics, Report Z2733.41.
- Uittenbogaard, R.E., Bosboom, J. and G. Klopman, 2000. *Numerical simulation of wave-current driven sand transport*. WL| Delft Hydraulics, Report Z2899.
- Uittenbogaard, R.E., 2000. 1DV simulation of wave-current interaction. *Proc. ICCE 2000*.
- Zyserman, J.A. and J. Fredsøe, 1994. Data analysis of bed concentration of suspended sediment. *J. Hydraulic Eng.* **120**(9), ASCE, pp. 1021-1042.



WL | Delft Hydraulics

**Rotterdamseweg 185
postbus 177
2600 MH Delft
telefoon 015 285 85 85
telefax 015 285 85 82
e-mail info@wldelft.nl
internet www.wldelft.nl**

**Rotterdamseweg 185
p.o. box 177
2600 MH Delft
The Netherlands
telephone +31 15 285 85 85
telefax +31 15 285 85 82
e-mail info@wldelft.nl
internet www.wldelft.nl**

